



UNIVERSITÀ DEGLI STUDI DI NAPOLI
FEDERICO II

Scuola Politecnica e
delle Scienze di Base



Università degli Studi di Napoli Federico II
Dottorato di Ricerca in
Ingegneria Strutturale, Geotecnica e Rischio Sismico
THESIS FOR THE DEGREE OF DOCTOR OF PHILOSOPHY

Safety of existing bridges

Traffic load models for accurate safety checks and methods for damage detection

by
Giusiana Testa

Advisor: Prof. Iervolino Iunio, Prof. Bilotta Antonio



Scuola Politecnica e delle Scienze di Base
Dipartimento di Strutture per l'Ingegneria e l'Architettura

*Si conobbero.
Lui conobbe lei e sé stesso,
perché in verità non s'era mai saputo.
E lei conobbe lui e sé stessa,
perché pur essendosi saputa sempre,
mai s'era potuta riconoscere così.
(da Il barone rampante - Italo Calvino)*

A Leonardo

Safety of existing bridges
Traffic load models for accurate safety checks and
methods for damage detection

Ph.D. Thesis presented
for the fulfillment of the Degree of Doctor of Philosophy
in Ingegneria Strutturale, Geotecnica e Rischio Sismico
by
Giusiana Testa

October 2023



Approved as to style and content by

Prof. Iervolino Iunio, Advisor
Prof. Bilotta Antonio, Advisor

Università degli Studi di Napoli Federico II
Ph.D. Program in Ingegneria Strutturale, Geotecnica e Rischio Sismico
XXXV cycle - Chairman: Prof. Iunio Iervolino



www.dist.unina.it/dottorati-di-ricerca/dottorati

Candidate's declaration

I hereby declare that this thesis submitted to obtain the academic degree of Philosophiæ Doctor (Ph.D.) in Ingegneria Strutturale, Geotecnica e Rischio Sismico is my own unaided work, that I have not used other than the sources indicated, and that all direct and indirect sources are acknowledged as references.

Parts of this dissertation have been published in international journals and/or conference articles (see list of the author's publications at the end of the thesis).

Napoli, September 18, 2023

Giusiana Testa



Abstract

The calibration of traffic loads based on real traffic data of the road network and health monitoring system are two useful tools for the assessment of their safety.

Therefore, in this thesis (i) the innovative data processing techniques aimed at structural monitoring and structural damage detection are showed and compared and (ii) a methodology for calibrating traffic loads based on traffic micro-simulations is discussed. Regarding structural monitoring, a dynamic identification technique namely Frequency Domain Decomposition (FDD) is described. The use of this technique allows to detect the dynamic properties of structures in terms of vibration frequencies and modal shapes. The characterization of the dynamic behavior of structures is aimed at: (i) detecting any anomalies that may be indicative of a damage condition and (ii) updating the FE model. In order to fully characterize the dynamic behavior of structures with the smallest number of sensors, it is necessary to adequately design the sensor network. In fact, the accuracy of dynamic identification results depends on the number and location of sensors placed on the structure. Therefore, optimal sensor placement (OSP) techniques for the accurate design of the accelerometer network are described.

Since the accuracy of the dynamic identification depends on the number and position of the sensors placed on the structure. The main OSP methods provide an efficiency ranking for the possible positions of an accelerometer. However, a selection criterion for the optimal sensors number is not provided.

In this thesis, a criterion is firstly proposed to minimize the number of sensors and optimize their position using the efficiency ranking of the Effective Independent Method. The methodology is applied to the prestressed railway bridge of Circumflegrea of Naples.

Moreover, the results obtainable through FDD are compared with the adoption of artificial intelligence algorithms, i.e., an unsupervised data driven methodology. The latter is developed by combining a Variational Autoencoder and a One Class - Support Vector Machine. This method is applied to two case studies, i.e., a steel structure and prestressed concrete joists.

Finally, the methodology for probabilistically characterizing the traffic loads on bridges based on network-level traffic micro-simulation is described through application to the A56, that is the urban highway that connects the districts of Naples (Italy).

Keywords: traffic load, micro-traffic simulations, dynamic identification, optimal sensor placement, artificial neural networks, anomaly detection

Abstract

La calibrazione dei carichi da traffico basata su dati di traffico reali della rete stradale e un efficace sistema di monitoraggio delle sue condizioni di salute sono due strumenti utili per la corretta valutazione della loro sicurezza. Quindi, in questo elaborato, (i) le principali tecniche di elaborazione dati finalizzate al monitoraggio strutturale e al rilevamento di danni strutturali sono mostrate e confrontate e (ii) una metodologia di calibrazione dei carichi da traffico basata su micro-simulazioni di traffico è discussa.

In merito al monitoraggio strutturale, in primo luogo, una tecnica di identificazione dinamica detta Frequency Domain Decomposition (FDD) è descritta. L'impiego di questa tecnica permette di rilevare le proprietà dinamiche delle strutture in termini di frequenze di vibrare e forme modali. La caratterizzazione del comportamento dinamico delle strutture è finalizzata a: (i) rilevare eventuali anomalie che possono essere sintomo di una condizione di danno e (ii) all'aggiornamento del modello FE. Affinché le tecniche di identificazione dinamica siano efficaci - ossia con il minor numero di sensori sia possibile caratterizzare completamente il comportamento dinamico delle strutture - è opportuno progettare in maniera adeguata la rete di sensori da adoperare. Infatti, l'accuratezza dei risultati dell'identificazione dinamica dipende dal numero e dalla posizione dei sensori disposti sulla struttura. Pertanto, le tecniche di optimal sensor placement (OSP) per la progettazione accurata della rete accelerometrica sono descritte. I metodi OSP presenti in letteratura forniscono una graduatoria di efficienza per le possibili posizioni di un accelerometro. Tuttavia, non è fornito un criterio di selezione del numero di sensori ottimale. In questa tesi viene proposto un criterio per minimizzare il numero di sensori e ottimizzarne la posizione, a partire dalla classifica del metodo Effective Independence. La metodologia è applicata al ponte ferroviario in c.a.p. della Circumflegrea di Napoli. Infine, i risultati ottenibili tramite FDD sono confrontati con l'adozione di un algoritmo di intelligenza artificiale, ossia una metodologia non supervisionata basata su dati. Quest'ultima è sviluppata combinando un Variational Autoencoder e un One Class - Support Vector Machine. Questo metodo viene applicato a una struttura in acciaio e a travetti in calcestruzzo armato precompresso.

Infine, la metodologia per caratterizzare probabilisticamente i carichi di traffico su ponti basata sulla micro-simulazione del traffico a livello di rete è descritta tramite l'applicazione all'A56, cioè l'autostrada urbana che collega i distretti di Napoli (Italia).

Parole chiave: carico da traffico, micro-simulazioni di traffico, identificazione dinamica, ottimizzazione della posizione dei sensori, reti neurali artificiali, rilevamento di anomalie.

Acknowledgements

Part of this study was performed thanks to funding from the DiSt – Tangenziale di Napoli spa agreement of 2021.

Another part was developed during the ReLUIs-Ponti project - funded by the Higher Council of Public Works and supported by the GRISIS project, implemented by STRESS scarl under ERDF Campania 2014-2020 – and during Digital Smart Structures DS2 – supported by INAIL.

I thank Ente Autonomo Volturno Srl for their cooperation in the realization of the demonstrator.

I would like to thank my tutors Prof. Antonio Bilotta and Prof. Iunio Iervolino for leading and supporting me during the PhD.

To the scientific committee, Prof. Flora and Prof. Cosenza thank you for your advice and attention to me.

I thank all those who helped me during my research activities, Eng. Chioccarelli, Eng. De Angelis, Eng. Baltopoulos, Eng. Montanino, Prof. Prevede, Prof. Punzo and Prof. Pecce.

Special thanks to Dr. Gaetano Zaccaria for his cooperation about traffic microsimulations and Dr. Andrea Pollastro for his continuous support on artificial intelligence.

Finally, I want to thank Dr. Antonio Grella for the support and the sincere relationship of esteem and affection.

Finally, I thank all the colleagues and friends with whom I have spent my PhD.

Any opinions or conclusions from the study do not necessarily reflect those of the funding entity.

Contents

Abstract	i
Acknowledgements	iii
Introduction	3
1.1. The safety of existing bridges	3
1.2. The Goal of thesis.....	5
1.3. Framework.....	7
1.4. Related Works	8
1.4.1. Traffic Load	8
1.4.2. Structural Health Monitoring.....	13
Damage Detection	22
2.1. Operational Modal Analysis	24
2.2. Dynamic Identification.....	26
2.2.1. Frequency Domain Decomposition	27
2.2.2. Modal Analysis	28
2.2.3. Power Spectral Density and Singular Value Decomposition	30
2.2.4. Modal Assurance Criteria	31
2.3. Model Updating.....	32
2.4. Artificial Intelligence	34
2.4.1. Artificial Neural Networks	34
2.5. Methodology	37
2.6. The case studies.....	39
2.6.1. Steel frame.....	39
2.6.2. Prestressed concrete joists	48
2.7. Conclusions	57
Updating of FE models	59
3.1. Optimal Sensor Placement	60
3.2. Selection Criteria	62
3.2.1. Railway bridge of Circumflegrea (EAV).....	69
3.3. Model Updating.....	78
3.3.1. Tammarecchia Bridge	78
3.4. Conclusions	88

Traffic load models for accurate safety checks	89
4.1. A56 – Tangenziale di Napoli	90
4.1.1. A56 Bridges: Miano Agnano, Calata San Domenico and Arena Sant’Antonio	90
4.2. Regulatory standards	96
4.3. Traffic Model	100
4.3.1. Cluster Analysis.....	100
4.3.2. Daily O/D Matrix	103
4.3.3. Traffic characterization	104
4.3.4. Calibration of vehicle behavior	106
4.3.5. Traffic microsimulation.....	107
4.4. Annual distributions of maximum stresses	109
4.4.1. Vehicle weight and axial forces	109
4.4.2. Traffic load schemes	112
4.4.3. Results	113
4.5. Conclusions	120
Conclusions.....	121
Annex A	vi
Annex B	x
References	xiv
List of Figures	xxii
List of Tables.....	xxiv

Introduction

1.1. The safety of existing bridges

In recent years, the safety of existing structures - such as bridges and viaducts - has been a much-discussed topic because, on the one hand, structures are subject to significant variations in traffic loading from design standards and, on the other hand, their health may be altered due to the natural degradation of materials accentuated by environmental effects.

Thus, the main issues related to the safety of existing bridges can be grouped into two macro categories namely the monitoring of the structural health condition and the structural safety checks. In the former case, the monitoring system allows the detection of the structural health status under operating conditions, while in the latter, the degree of structures 'safety referred to collapse conditions is ensured through safety checks.

About the structural monitoring in order to detect the structural damage, monitoring strategies are mainly characterized by (i) types of monitoring (static or dynamic), (ii) analysis methodologies (i.e., input-output, with known forces, or output-only, with unknown forces), and (iii) analysis approach (i.e., data-driven or model-based).

Static monitoring techniques consist of discrete detection of gradual and slow variations of some static quantities in a long time. Conversely, dynamic monitoring methodologies allow the detection of anomalies based on the variation of features extracted from the acquired signals (e.g., natural frequencies of vibration, modal curvature, etc.).

However, the accuracy of dynamic identification results depends on the number and location of sensors on the structure. While the adoption of many sensors tends to increase the goodness of results, a limited number of sensors reduces trial costs and the volume of data to be processed. So, optimizing the sensor network consists of the optimal choice of the number and position of instruments on the structure.

The model-based approach requires the use of a finite element model consistent with the actual behavior of the structure for the prediction of structural degradation and the analysis of its evolution over time; conversely, the data-driven approach allows the identification of the structural healthy status through the analysis of signals acquired by the sensors. In general, the use of a calibrated numerical allows to investigate the causes of a possible variation in structural response, to assess the structural capacity and behavior in both operational and exceptional conditions. On the other hand, data-driven approaches are preferred because for such structures it is not easy to obtain an adequate model of the physical behavior in operating conditions although the high variability of the boundary conditions could alter the anomaly estimate.

In both cases, when structural damage is localized to a small portion of the structure, it may not result in significant changes in structural behavior. These results may involve insignificant variations in the damage-sensitive features and, therefore, damages could not be detected clearly. The process of statistical modeling for feature discrimination (i.e., defining damage thresholds) is a tool that allows the identification of structural

damage when it has not yet compromised the operability of the structure. On the other hand, the issue can be overcome using artificial intelligence algorithms.

Indeed, innovative techniques based on the machine learning and deep learning are applied to structural monitoring in order to detect damage conditions. In this field, two strategies can be followed: (i) a supervised one that involves knowledge during training of all possible damage conditions that may occur on the structure and (ii) an unsupervised one that involves training the algorithm only with data recorded on the structure in healthy condition. For the former, the use of numerical models is necessary to simulate all possible damage scenarios, while the latter allows to use only experimental data. For the definition of damage thresholds, the use of classifiers subject to optimization processes allows the statistical problem to be bypassed.

Finally, the ability to detect the real condition of the structures enables: (i) to realize an early warning system for the management and scheduling of maintenance activities and (ii) to calibrate the numerical model of the structure to use in safety checks.

Indeed, the safety of existing bridges is checked through the use of FE models to calculate stresses and displacements caused by the traffic loading schemes imposed by current standards. To make the finite element model representative of the structural behavior, a dynamic identification process for possible model updating may be necessary.

Regarding traffic loads to assess the level of existing bridges' safety, in current standards, they are typically based on a semi-probabilistic approach in which the probability of exceeding the effects of actions (or, equivalently, the return period), is controlled for any time interval of interest. However, on a specific bridge, this probability is strongly conditioned by the characterization of traffic on the transportation network to which the bridge belongs. Several studies related to the calibration of traffic loads based on real data have been conducted in recent decades; however, when these are not available, traffic simulations can be a valuable tool to determine a surrogate for the traffic data specific to the structure. Structure-specific traffic load analysis is desirable to determine the margin of safety under which the bridge operates and to introduce traffic control measures or structural retrofitting actions, if necessary.

Next, bridges should be equipped with a monitoring system - temporary or permanent - for characterizing its health status over time.

Therefore, the combined use of a calibration of traffic loads based on real traffic data for the proper calibration of the supply and demand model of the road network and an effective monitoring system allows a complete safety assessment of existing bridges.

1.2. The Goal of thesis

This thesis discusses the main safety issues of existing bridges, namely, (i) on the one hand, the main structural monitoring techniques for identifying structural damage are analyzed, and (ii) on the other hand, traffic loading schemes to carry out safety checks are analyzed. The main topics are described in Figure 1.

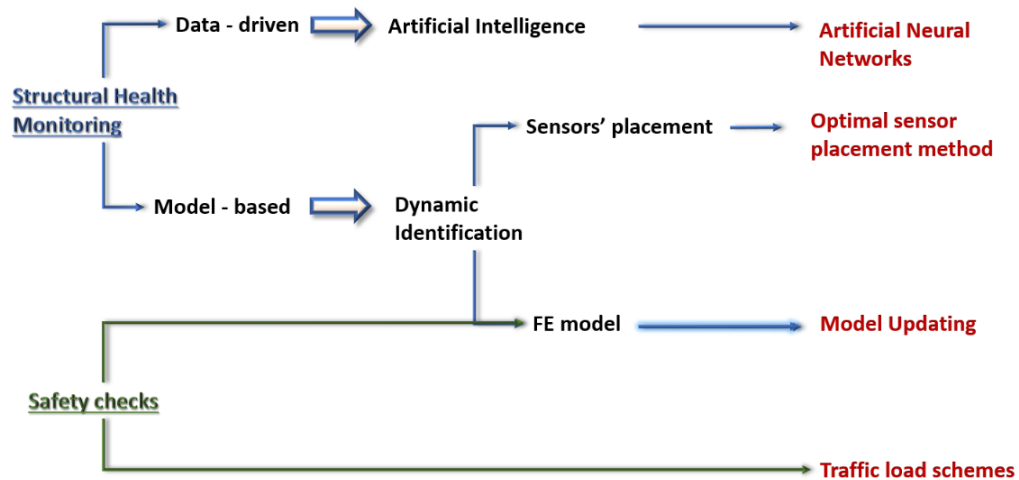


Figure 1 – Flow chart

About structural monitoring, the main techniques are based either on dynamic characterization of structures or on artificial intelligence. Artificial intelligence-based techniques use artificial neural networks. These techniques can be divided according to the type of approach by which the training phase of the network is performed namely: (i) supervised approach and (ii) unsupervised approach. In the first case, neural network training is performed with labeled data. In the second case, however, training is performed with unlabeled data. Since the purpose of the network is to define whether damage is present or absent, a supervised approach requires the use of data recorded on the structure in both healthy and damaged conditions. Thus, in the absence of heterogeneous data, the FE model of the structure is necessary to simulate the damage conditions and create a surrogate for the real data. However, especially for complex structures, the simplified numerical model may not correspond with the real behavior of the structure. Therefore, in the field of structural engineering, an unsupervised approach is more effective because it can be used without numerical data. Both aforementioned techniques can be employed with either a model-based approach in which numerical models are required to identify possible anomalies caused by structural damage or a data driven approach based on data. In this thesis, a methodology based on the joint use of variational autoencoder and one class - support vector machine for structural damage identification is described. The proposed methodology is based on a data-driven approach that allows damage identification in the absence of an FE model of the structure. The method is therefore employed on two case studies: (i) a 3-D steel frame and (ii) prestressed reinforced concrete joists. The two case studies are subject to both the described methodology and a dynamic identification process using the Frequency Domain Decomposition (FDD). This allowed the comparison of techniques. The aim is

to show that the proposed method performs better especially in the presence of localized and little extensive damage.

The dynamic characterization of structures is performed using the Frequency Domain Decomposition (FDD) technique, which allows the eigenfrequencies and modal shapes of the structure to be derived. Generally, these techniques are used with a model-based approach since they are aimed at updating the numerical model of the structure. Since the goodness of results that can be obtained from dynamic identification is a function of the spatial distribution of sensors on the structure, the main optimal sensor placement techniques for optimizing the sensor network design are discussed in this thesis. Specifically, since these techniques make it possible to derive a ranking of efficiency among all possible positions of a sensor on the structure, but no criterion is established for selecting the optimal number to be used, in this thesis a criterion is defined for selecting the optimal configuration of sensors to be used for performing a dynamic identification test.

The results of the identification process can then be used to: (i) detecting anomalies i.e., identifying structural damage, and (ii) updating the FE model of the structure with which to subsequently conduct safety verifications. Indeed, safety verifications of existing bridges are conducted at the section level by exploiting the FE model of the structure in order to derive the maximum stresses caused by code-prescribed loading schemes. For existing bridges, the issue of traffic loading schemes is a much-discussed topic in the literature because code-mandated loading schemes may be too conservative than the usual traffic flows insisting on the structure and dependent on the road network in which the structure is embedded. Technological developments have made it possible to know the actual loading schemes on the structure through the acquisition of real time traffic data. However, in the absence of these data, traffic microsimulations could allow a surrogate for them. Therefore, in this thesis, a methodology for identifying traffic load schemes based on microsimulation of traffic on the entire road network - in which the facility is located - is defined. In this way, the structural safety assessment of bridges can be performed with a network-specific characterization of the uncertainty of traffic loads, compared to the conventional code. The method is applied to three prestressed concrete bridges on the A56 – Tangenziale di Napoli.

1.3. Framework

This thesis analyses the two main issues about the safety of existing bridges, i.e., traffic loads and the structural health monitoring. On the one hand a methodology for the calibration of traffic loads based on micro-simulations is proposed. On the other hand, the main data analysis techniques necessary for structural monitoring based on traditional (such as Frequency Domain Decomposition) and innovative (with artificial neural networks) techniques are analyzed. Finally, optimal sensor placement algorithms are defined in order to maximize the goodness of results of a dynamic identification process, and a criterion for selecting the number and location of sensors is described.

In **Chapter 2**, the techniques to anomaly detection are described. These techniques can be based on the use of artificial intelligence algorithms or on the results of dynamic identification process. In the first case, a methodology to identify a structural damage is proposed. This methodology is applied to two experimental case studies namely (i) a steel frame tested for Phase II of the SHM benchmark problem (IASC, 2003) and (ii) a prestressed concrete joist tested at the DiSt laboratory (DS2, 2022). The two applications involved each case study both in a "healthy" and "damaged" conditions. In addition, the use of a dynamic identification technique applied to the same data enabled a direct comparison in terms of damage identification capability between the artificial intelligence algorithm and the traditional dynamic identification algorithm.

In **Chapter 3**, dynamic identification for updating the FE model of the structure is discussed. In addition, some optimal sensor placement (OSP) techniques are described. These techniques allow a ranking of the efficiency of each sensor placement for analyzing the dynamic behavior of the structure, but do not establish a selection criterion for the optimal number of sensors. Therefore, a selection criterion is described in order to minimize the number of sensors to be used and optimize their distribution on the structure to maximize the results of the identification process. Finally, two applications are described: (i) a steel-concrete composite bridge, the Tammarecchia Bridge, for which an update of the FE model was carried out through the adoption of dynamic and static measurements; and (ii) a reinforced concrete railroad bridge of the Circumflegrea connecting the Quarto Centro and Quarto Stazione stations on the Montesanto - Quarto - Naples line, is used to apply an optimal sensor placement technique with the proposed selection criterion.

In **Chapter 4**, a methodology for calibrating traffic loads based on the use of micro-simulations is described. The methodology is then applied to three prestressed concrete viaducts of the A56 - Tangenziale di Napoli namely Miano Agnano viaduct, Calata San Domenico and, finally, Arena Sant'Antonio viaduct.

1.4. Related Works

This section describes the literature about the structural monitoring and the structural safety checks. In the first case, the existing literature focuses on methodologies for structural damage detection based on both traditional and innovative - i.e., based on the adoption of artificial intelligence algorithms - data analysis techniques. In the second case, special consideration is given to studies about the calibration of traffic load schemes performed with micro traffic simulations.

1.4.1. Traffic Load

In the last decade, the need to verify the safety level of existing bridges has increased because, on the one hand, their functionality can be challenged by a progressive increase in traffic actions and, on the other hand, the natural degradation of materials, together with inefficient planning of maintenance activities, could compromise their load-bearing capacity. For safety checks of existing bridges, a semi-probabilistic limit state approach is provided in the current standards (Wiśniewski et al., 2012; O' Brien et al., 2015) in which traffic loading schemes are calibrated so that the probability of their exceedance effect is controlled for any time interval of interest. The two main strands focus of safety checks of existing bridges are (i) the analysis of traffic loading schemes and (ii) the variation of partial safety factors respect to those used for the newly designed structures. Both topics are interesting, especially in Italy where strict regulations on the operation of road bridges are in place, based on conventional structural safety verifications (CS.LL.PP., 2020)

Regarding partial safety factors, many authors, consistent with the *fib80* (fib Bulletin No. 80, 2016), propose the adoption of some risk models for calibrating the reliability index and obtaining the partial safety coefficients to use during structural checks.

Koteš et al 2013 (Koteš and Vičan, 2013) define a strategy to assess the reliability levels of safety checks for existing bridges. These levels – that depends on the age of bridge - are used to determine the partial safety factors associated to the strength and the load effects. So, authors show the calculation of partial factors for concrete elements, reinforcement, permanent load, and variable traffic load.

Sýkora et al 2013 (Sýkora et al., 2013) describe the application of the semi-probabilistic approach in accordance with EN 1990 and ISO 2394 for safety checks of existing reinforced concrete bridges.

Numerical examples illustrate how design values and partial factors can be derived for different reliability objectives.

Gino et al 2019 review the partial-factor methods for the existing reinforced concrete structures proposed in Fib Bulletin 80. Specifically, the definition of partial factors for existing structures takes into account residual service life, in-situ and laboratory test results, variable action measurements, and reduced reliability levels based on both economic and human safety criteria.

The methodologies proposed in Bulletin fib 80 are applied by the authors to evaluate the safety of an existing prestressed concrete bridge built in the 1990s in Italy. The results were compared with the EN1990. About the traffic load, the code-prescribed probability of exceeding traffic effect on a specific bridge in a specific time depends on the characterization of traffic on the transportation network to which the bridge belongs (Enright et al., 2013). So, the assessment of the safety margin of existing bridges should be performed through a traffic load analysis specific to the structure.

O'Connor et al 2005 (O'Connor and O'Brien, 2005) describe a methodology for traffic load simulations using WIM statistics.

The objective is to present traffic flow simulation models, to verify their appropriateness for bridge safety assessment, and to determine the factors that influence their accuracy. The influence of the accuracy of recorded WIM data is a function of light and load effect. The authors show that the effects of increasing inaccuracy are attenuated with span width. Time-dependent and seasonality analyses provide no clear evidence of a seasonal trend.

O'Brien et al 2014 (O'Brien et al., 2014) analyze the phenomenon of truck volume growth during the life of a bridge and the influence of this growth on the effects of the maximum characteristic load. The study uses Weigh-in-Motion data (WIM) from the Netherlands to calibrate Monte Carlo simulation of load effects on a series of bridge spans. For short spans, the distribution of the maximum data is Weibull type. As the span increases, a better fit is obtained with Generalized Extreme Value type distributions.

Xin Ruan et al 2017 (Ruan et al., 2017) propose a specific traffic loading model for a long-span multi-pylon cable-stayed bridge.

Three traffic states on the bridge are simulated and via influence lines the stresses are derived. The traffic states are simulated by Monte Carlo simulation using the available WIM data. Finally, Weibull extrapolations are used to predict the extreme responses. These responses are analyzed and compared with different design codes. The results indicate that the maximum response is only 75% of the value calculated based on the Chinese design code (D60) and lower than other codes such as BS5400, AASHTO, ASCE, HSBA and Eurocode.

In Proverbio et al 2018 (Proverbio et al., 2018), the topic of reserve capacity analysis of existing bridges is discussed. In this paper, it illustrates the updating of the FE model by the error domain model falsification (EDMF) method used to compare real and numerical behavior. This paper introduces a methodology to assess the reserve capacity of bridges consistently with EDMF. The application concerns a reinforced concrete bridge in Singapore. The traffic load specifications of design codes (British Code-1978) and current codes (Eurocodes) are compared. For the specific case, the results show that past design practices resulted in an as-built reserve capacity of 60%. However, about 40% of the reserve capacity was absorbed by the increased demand caused by the new traffic loading schemes of the current Singapore codes.

Skokandic et al 2022 (Skokandić and Mandić Ivanković, 2022) aim to demonstrate the benefits of using traffic monitoring data in structural safety assessment. The research illustrates the adoption of Weigh-in-Motion (WIM) data and subsequent extrapolation of maximum load effects on a bridge over a period of time. Finally, taking into account all related costs, possible strategies for bridge life management are presented.

Shi-Zhi Chen et al 2021 (Chen et al., 2021) propose a method to determine the weight limit of vehicles that can travel on urban bridges. A stochastic traffic model through site-specific weighing data and a vehicle-bridge simulation model are described. Then, a reliability analysis using the probabilistic density evolution method is performed taking into account uncertainties related to load and structural strength. The study is presented with reference to 75 urban bridges in Nanjing, China. For this reason, the use of traffic real data (Meli and Pugi, 2013; Lydon et al., 2016) to calibrate the traffic load is the main topic of the existing literature. However, when direct traffic observations are not available (Zhang et al., 2019), simulation can provide a surrogate for such facility-specific data (Olstam and Tapani, 2011) Micro-simulation of traffic leads to recording

the movement of each vehicle along the roadway bordering the bridge and so, it allows to assess the effects of that traffic.

In the last two decades, several studies on traffic micro-simulation have been conducted, either to provide a model for extracting congestion characteristics to simulate highway traffic flow (Adeli and Ghosh-Dastidar, 2004; Ghosh-dastidar and Adeli, 2006; Caprani, 2010), to show general methodologies for building a traffic flow prediction model (Jiang and Adeli, 2004; Treiber et al., 2011), or to localize the effects of disruptive accidents (Karim and Adeli, 2002). In addition, software has been developed to authorize the transit of exceptional vehicles (Waheed and Adeli, 2000) or to support the assess of existing bridges (Sirca and Adeli, 2005).

Dong Guo et al 2019 (Guo and Caprani, 2019) analyze the design standards approach to traffic load configuration on bridges and propose an approach to reflect the real traffic load distribution. The authors find that the worst-case load effect obtained by modeling the live load only on the adverse portion of the influence line is characterized by a low probability of occurrence. Therefore, a traffic microsimulation is used to simulate traffic flows on 1200-meter bridge. Load effect results are extrapolated for return periods of 5, 75 and 1000 years, and from these, a distribution method is proposed based on different traffic topologies obtained from an adverse combination of congested and free traffic.

Bin Sun et al 2019 (Sun et al., 2019) developed a fatigue damage prognosis algorithm for newly constructed long-span steel bridges under vehicle loading. The multiscale fatigue damage prognosis algorithm was developed based on the multiscale FE model. The vehicle load on the bridge is defined using recorded weight-in-motion (WIM) data and agent-based traffic flow micro-simulation method. The method is tested on a newly constructed long-span cable-stayed bridge for the period from 2010 to 2020.

Micu et al 2019 (Micu et al., 2019) propose a technique to estimate the effects of maximum load characteristic of traffic on the Forth Road Suspension Bridge (FRB). The authors believe that when the bridge is subject to the critical state of congestion, most WIM systems are not reliable. Therefore, they use CCTV cameras and image processing techniques to collect five months of bridge traffic data on the FRB. The axial force in the main cable of the bridge is calculated using the corresponding line of influence, and the maximum characteristic values of axial force are assessed for return periods of 75 and 1000 years.

Ning Hou et al 2021 (Hou et al., 2021) study traffic load modeling from weigh-in-motion (WIM) data on a long-span Shanghai cable-stayed bridge. On the one hand, the authors analyze vehicle selection from the available WIM data. On the other, the process of transforming the data statistics into a deterministic load model is described.

Junyong Zhou et al 2020 (Zhou et al., 2020) examine a Chinese highway widening project to assess structural safety of widened bridges in a way using code-based deterministic approaches and reliability-based probabilistic approaches. Previous and current Chinese bridge designs and other national codes were used in the deterministic evaluation. On the other hand, in the probabilistic evaluation, irregular multi-lane truck load modeling was implemented based on site-specific traffic data. The safety of the bridge under normal traffic conditions with all lanes open and under occasional traffic conditions with lane closures was then analyzed. The results indicate that most of the slabs are unsafe according to current Chinese design specifications. However, a site-specific evaluation under normal traffic conditions indicates that these slabs have adequate safety reserves. The closure of the express lanes does not significantly affect the safety of the slabs. In contrast, the closure of slow lanes significantly affects safety.

Junyong Zhou et al 2022 (Zhou et al., 2022) propose a numerical approach to study the structural safety of widened bridges when maintenance work requires partial lane closure on the new bridge. For these, the existing bridge may not meet the new design standards although the distribution of traffic loads is non-uniform between new and existing structure. When lane closures are required to perform maintenance work on the new bridge, traffic is diverted from the new to the existing bridge, and the safety of the old bridge may be a critical issue. The results show the most effective restrictions about weight and of transit speed so that the level of safety is guaranteed during maintenance activities.

Jihwan Kim et al 2022 (Kim and Song, 2022) proposed a live load model for long-span bridges based on site-specific traffic conditions. The analysis of traffic conditions allows classification based on the percentage of heavy vehicles and the frequency of traffic congestion. Traffic microsimulation allows the production of live load samples from which to obtain a design lane load model and multiple presence factors for long-span bridges. The application was tested on a real bridge, and the results are compared with those of the current South Korean bridge design code.

Baorui Dai et al 2022 (Dai et al., 2022) present a method for predicting the effects of extreme loads on road-rail bridges in order to identify multiple presence factors (MPFs). The method consists of an unsupervised clustering algorithm based on a generalized extreme value mixture model (GEVMM). Road vehicle flow is generated based on traffic and vehicle parameters, while train flow is generated based on passenger volume distribution and train schedule. The 1000-day load effects on road-rail bridges with various spans were simulated and then used to predict the maximum load effects in 100 years. Then, MPF values of road-rail bridges are calculated from the predicted maximum load effects during a 2000-year return period.

Xinfeng Yin et al 2023 (Yin et al., 2023) analyze the dynamic interactions of suspension bridges with the different traffic conditions they may be affected by. They propose a traffic-bridge interaction (TBI) model for the dynamic analysis of suspension bridges considering realistic traffic behavior and real vehicle characteristics.

The stochastic simulation model based on the joint use of the Monte Carlo approach and the intelligent traffic guidance model makes it possible to reproduce realistic traffic flow. The TBI is applied to a long-span suspension bridge model. The effect of traffic loads on the vertical displacement of the bridge is evaluated by varying key parameters of the TBI framework, such as traffic density and road roughness.

Rossigali et al 2023 (Rossigali et al., 2023) present two traffic load configurations developed on the basis of a real traffic database, traffic simulations, modeling of dynamic interaction between vehicles and structures, and statistical extrapolations. The proposed load models include dynamic effects, and they were calibrated for two-lane, single-track bridges with span lengths up to 40 m under free traffic conditions. The target values of the effects were compared with those generated by the proposed new load models and the model provided by Brazilian code NBR 7188. We note transportation engineering models have not yet been combined with structural models to develop a traffic-specific bridge safety assessment procedure for transportation networks. For this, a methodology is described to estimate a probabilistic model of hourly origin/destination (OD) demand matrices based on the observed spatial and temporal correlations of available traffic counts. The individual spatiotemporal trajectory of each simulated vehicle allowed the mapping of vehicle axes, and thus loads, on each bridge at each instant of a sampled traffic year. Applying these load schemes to the structural model of each bridge allows

the annual frequency distribution of maximum structural actions to be determined. Modelling the supply-demand matrix of the entire network in which the bridge insists is the main step in performing the traffic micro-simulation. In particular, such modelling can be nontrivial considering that traffic flows can be highly uncertain (Ciuffo et al., 2008; Buisson et al., 2014). At the same time, consistent structural modelling is needed to translate vehicular traffic into structural actions and safety controls. The study is referred to a specific case study namely three bridges of the A56 – Tangenziale di Napoli (Testa et al., 2022 a).

1.4.2. Structural Health Monitoring

Related to the Level 1 of the structural monitoring i.e., the detection of structural damage conditions on structures and infrastructure, scientific research has mainly focused on data analysis techniques of both traditional types based on dynamic identification and innovative types based on deep learning algorithms.

Dynamic identification techniques (Brincker, R., Zhang, L., & Andersen, 2000) - both those in the frequency domain and those in the time domain applied mainly to bridges and viaducts - allow the extraction of damage-sensitive features whose variation may be an index of the health condition of the structure. Several authors have analyzed the type of feature best suited for the purpose. Regarding the techniques in the frequency domain (Rainieri, C., Fabbrocino, G., & Cosenza, 2007; Fan W, 2011), the main features employed can be divided into two macro-categories depending on the purpose to be achieved namely:

- frequency (Pereira et al., 2020) and modal shapes (Prendergast et al., 2018) with which only structural damage identification can be performed.
- modal curvature (Pooya and Massumi, 2021), modal strain energy (Gomes et al., 2018) and modal strain (Pandey and Biswas, 1994) to perform damage identification and localization.

For time-domain techniques (Fassois and Sakellariou, 2007) on the other hand, autoregressive models (AR), moving average models (MA), and, finally, autoregressive moving average models (ARMA) (Kang et al., 2005) are the main techniques used. For these, the basic assumption is that the system is stationary in time during data acquisition. For all three techniques, the goal is to predict the i -th response of the structural system based on the previous and possibly the known input. The prediction is accomplished by linear combination, and the coefficients of the combination-derived when the structure is in a healthy condition-represent the damage-sensitive feature.

In Bodeux et al 2001 (Bodeux and Golival, 2001), the ARMA model is used for damage detection based on estimating the uncertainties of modal parameters. Damage detection is performed on a statistical basis by analyzing changes in modal parameters. The benchmark "Steel-Quake" is used as a case study to validate the identification of frequencies, modal shapes and damping ratios.

In Zembaty et al 2006 (Zembaty et al., 2006), two full-size reinforced concrete frames were subjected to seismic excitations of increasing intensity through a vibrating table. The objective is to study the changes in modal parameters due to the development of cracks in the concrete. It was observed that damage resulted in a faster decrease in natural frequency for the 1st mode and slower for later modes. It was noted that the loss of natural frequencies was about 10% and that the first cracks could not be detected visually (15% loss of stiffness).

In Alvandi et al 2006 (Alvandi and Cremona, 2006), some damage identification techniques such as mode shape curvature method, flexibility method, flexibility curvature method and strain energy are analyzed. The application of these methods to a supported beam with different damage levels allows a comparison of the techniques. With this application, the authors showed that the strain energy method presents more stable results against noisy signals. The mode shape curvature method, flexibility method, and flexibility curvature method are able to detect and localize damage, but in the case of complex and simultaneous damage, these techniques are less effective.

In Huth et al 2005 (Huth et al., 2005), large-scale progressive damage tests were performed on a prestressed concrete highway bridge to study the sensitivity of different

damage detection, localization and quantification methods based on modal parameters. It was observed that although the bridge was severely damaged, the natural frequencies show only minimal changes instead, the relative changes of modal shapes are greater. Finally, detecting or locating damage through changes in the flexibility matrix gave better results than natural frequencies or modal shapes. In conclusion, the authors state that damage detection in prestressed concrete bridges is hardly possible due to the almost complete recovery of stiffness after crack closure in prestressed concrete.

In Jin et al 2017 (Jin et al., 2017), a method based on extended Kalman filtering (EKF) is described in order to perform a real-time structural damage detection. The numerical validation of the method is performed through linear and nonlinear structures with different damage scenarios. The Authors argue that the proposed method avoids false alarms - related to damage identification - often caused by environmental and operational effects.

Curadelli et al 2008 (Curadelli et al., 2008) propose a method to identify structural damage through the instantaneous damping coefficient and a wavelet transform. Laboratory tests and numerical simulations show that the presence of damage results in significant changes in the damping coefficient rather than in frequency or modal form. Zhao et al 2012 (Zhao and Zhang, 2012) propose a method to identify structural damage based on the modal characteristics. The method assumes that the reduction of the structural stiffness due to damage is the sum of each elementary stiffness matrix multiplied by a damage coefficient where the damage coefficient can be solved by the equation of motion. In addition, the MAC criterion is introduced to check the correlation of mode shapes between the damaged and undamaged structure. The method is applied to a numerical case study of a six-span truss beam. The results indicate that the proposed method is effective in locating and quantifying the extent of damage.

Ghannadi et al 2019 (Ghannadi and Kourehli, 2019) defined a structural damage detection method using the Moth-Flame Optimization Algorithm (MFO). The objective function underlying the MFO consists of MAC and natural frequency. The method was applied to two numerical cases, namely a truss and a shear frame. The results showed that the presented method is efficient in damage identification.

Huseynov et al 2020 (Huseynov et al., 2020) present a methodology for assessing the condition of bridges using direct rotation measurements. The methodology - in which rotation is assumed as a damage-sensitive parameter - was first calibrated on numerical case studies. Then several laboratory tests were conducted in order to validate the methodology. The tests were conducted on a simply supported bridge structure, and several single and multiple damage scenarios were considered.

A damage detection index for arch structures is presented in Giordano et al 2020 (Giordano et al., 2020). The results of eight laboratory tests performed on arches are used to define the index. The arches were damaged to failure using pseudo-static test cycles. The damage indicator is a function of frequency reduction compared to the undamaged scenario. Finally, the index was also validated for different arch collapse mechanisms through finite element modeling.

In Zhang et al 2021 (Zhang and Zhu, 2021), damage indices based on Pearson's correlation coefficient, Spearman's correlation coefficient and Kendall's correlation coefficient, respectively, are obtained using the measured vibration responses of the bridge under vehicle loading for structural damage identification. The proposed method is verified by numerical simulation and compared with the method based on the correlation function amplitude vector (CorV). Numerical results show that the proposed

method can effectively identify and localize the damage, and the effectiveness of the index based on Pearson's correlation coefficient is the best. Finally, the method is validated through experimental cases.

In Meixedo et al 2021 (Meixedo et al., 2021), a methodology for structural damage detection is proposed. It consists in a combination of time series analysis methods and multivariate statistical techniques. The effectiveness of the proposed methodology was validated in a steel-concrete composite arch railroad bridge with a permanent structural monitoring system. With this methodology, early damages are detected, even when it consists of small reductions in stiffness that do not compromise the safety or use of the structure.

The goodness of fit of the results obtained is highly dependent on: (i) environmental conditions during experimental testing (Gentile et al., 2016), (ii) duration and resolution of acquired signals, and (iii) number and location of sensors. In particular, different environmental conditions for different test setups can result the variation in features not attributable to the presence of structural damage (Luo et al., 2022). Depending on the frequency range to be investigated, the acquisition duration and resolution of the instrumentation should be accurately determined in order to limit external disturbances. In fact, appropriately designing the accelerometer network through optimal sensor placement (OSP) techniques (Kammer, 1991; Papadopoulos and Garcia, 1998; Michele Meo, 2004; Rao et al., 2014; Liu et al., 2018; Moussas, V. C., & Pnevmatikos, 2019) allows to optimize the identification process and, therefore, on the one hand not to lose information on modal deformations and on the other hand to reduce the costs associated with the experimental phases.

Papadimitriou 2004 (Papadimitriou, 2004) proposes a method of sensor optimization based on information entropy, i.e., measuring the uncertainty of system parameters. Author shows that the lower and upper bounds of information entropy are decreasing functions of the number of sensors and, therefore, he proposes two algorithms that are considered more efficient than genetic algorithms. The methods are presented with reference to two structural systems: (i) a 10-degree-of-freedom model with elastic mass and (ii) a three-dimensional truss structure.

In Ting-Hua Yi et al 2011 (Yi et al., 2011), a sensor optimization method (OSPS) that combines multiple existing methodologies is proposed. The initial sensor placement is obtained by QR factorization i.e., using the minimization of the off-diagonal elements of the MAC. The optimal configuration is returned by the generalized genetic algorithm (GGA). The method is described through the case study of the Guangzhou New TV Tower.

In this paper (Stephan, 2012), a sensor optimization method that exploits the finite element model of the structure is defined. The method uses two sensor selection criteria based on the observability of modal shapes and the information shared by the sensors. The set of optimal sensors is obtained by maximizing the Fisher information matrix and avoiding information redundancy among sensors.

Vincenzi et al 2017 (Vincenzi and Simonini, 2017) analyze the influence of modeling errors and parametric uncertainties in the sensors' placement for the structural health monitoring (SHM). The case study is a steel pedestrian bridge.

The employed OSP method is based on Information Entropy, and a correlation function-based method is described to take into account the model uncertainties. The application shows that the method can better estimate the upper modes when the number of sensors is greater than the number of modes of interest.

Chisari et al 2017 (Chisari et al., 2017), propose a novel method for optimal sensor placement based on defining the representativeness of the data with respect to global displacement. The method uses an optimization procedure based on Genetic Algorithms and is applied to two numerical case studies.

In Tan et al 2020, the main methodologies to optimize the sensors' position on the structure are analyzed with a focus on evolutionary algorithms and their variants.

Pachón et al 2020 (Pachón et al., 2020) study the main techniques of optimal sensor placement such as The Effective Independence (EFI) method and the Energy Matrix Rank Optimization (EMRO). The techniques are applied to a real case study such as the Monastery of San Jerónimo de Buenavista in Seville, Spain. A preliminary OMA campaign is performed to build a reliable finite element (FE) model. Then, the optimal sensor distribution is obtained by applying the different OSP techniques through the numerical model.

Nieminen et al 2023 (Nieminen and Sapanen, 2023) propose a two-step sensor placement optimization method. The method uses the criterion of minimum variance in the estimation error of structural responses. A measure of information redundancy is introduced as an additional criterion for the placement of triaxial sensors. A criterion based on modal displacement is also introduced to avoid the selection of locations with low vibration energy. The method is tested with numerical models of different types of structures and laboratory experiments.

In both cases (time or frequency domain), the decision-making process downstream of feature extraction - that is the statistical process of feature discrimination by which, having established a threshold of variation, it is possible to say that the structure is in a healthy or damaged condition (Pozzi, 2022), is the problem of greatest interest.

In addition, the results of dynamic identification techniques can also be used for updating the numerical model used for safety checks. Model updating is a necessary tool when adopting a model-based approach. It consists in the calibration of a numerical model following dynamic tests to characterize the modal characteristics of the structure. Based on the results of site tests it is possible to calibrate some parameters of the model in order to make the numerical model consistent with the real behavior of the structure. In this field, it is strongly discussed the possibility of automating the updating process by intervening directly on the mass and stiffness matrices extracted from the FE model without analyzing the possible physical phenomenon that led to the variation (Liu et al., 2016). Finally, the possibility to introduce the results of static tests (Wang et al., 2010; Xiao et al., 2015; Schommer et al., 2017) as well as dynamics in the update process allows to increase the accuracy of the FE model.

In Jaishi et al 2005 (Jaishi and Ren, 2005), a finite element model updating technique using ambient vibration test results is described.

The numerical application of a supported beam allows the analysis of possible objective functions for the updating method. Four objective functions were considered i.e., (i) in the first one only frequency is introduced as a variable, (ii) the second one considers only modal forms, (iii) modal flexibility in the third one, and (iv) finally all the previous variables together. Numerical analyses showed that the fourth function is the most complete, and this was implemented in a second case study of a steel arch bridge. The bridge was tested with ambient vibration measurements. In this case, the model updating produced an improvement over the experimental results in the modal parameters of the modes involved.

Wu et al 2006 developed a procedure for damage detection by model updating. The procedure was tested on a steel structure (IASC-ASCE). The procedure consists of two steps: (i) in the first, both weighted least squares methods and Bayesian estimation are adopted for the identification of the beam-column connection stiffness and Young's modulus of the structure; (ii) in the second, FE model updating enables damage detection. In

A probabilistic finite element (FE) model updating technique based on Bayesian modeling is described in Behmanesh et al 2015 (Behmanesh et al., 2015). Since the mass and stiffness of structures may have inherent variability due to various sources of uncertainty, such as variation in ambient temperature, wind speed, and traffic loads, the model updating via a hierarchical Bayesian model approach is considered more valid than classical approaches. In particular, the method is tested numerically on a 3-story shear building model.

Xiong et al 2009 (Xiong et al., 2009), the goal is to infer typical calibration parameters for a numerical model that provide a better match between physical and numerical data. For this purpose, the maximum likelihood estimation (MLE) approach for estimating the distributional properties of variable parameters is used. In addition, the u-pooling method (Ferson et al., 2008) is used as a validation metric to assess the accuracy of an updated model.

Schlune et al 2009 (Schlune et al., 2009) point out that generally initial models are simplified, and too few measurements on complex structures can lead to an erroneous update based on inaccurate modeling assumptions. Therefore, they propose a methodology that aims to: (i) eliminating modeling simplifications by manual model refinements and (ii) nonlinear optimization of modeling parameters through multiple-response objective functions that allow combining different types of measurements (static and dynamic). The proposed methodology was applied to a single arch bridge namely the Svinesund Bridge.

A process of updating the finite element model of the Vernon Avenue bridge over the Ware River in Barre, Massachusetts through data recorded by nondestructive testing is described in Sanayeu et al 2015 (Sanayei et al., 2015). Since the bridge was instrumented during all phases of construction, the update was possible with the static data set obtained during testing.

In Liu et al 2016 (Liu et al., 2016), the finite element model (FEM) of an arch bridge is updated through an automated procedure developed within two software programs. The first is used for sensitivity and optimization analysis, while the second for structural modeling.

Specifically, based on the original drawing and topographic survey, the initial FEM of the bridge is created.

Downstream of the update--for which dynamic tests on the structure are required--the updated FEM is verified by comparison with the results obtained from the static tests.

In this survey (Abdeljaber et al., 2017), several methods for structural damage identification by updating finite element (FE) models are analyzed. Several direct, probabilistic, statistical, and iterative methods for updating FE models for structural damage identification are described. evolutionary algorithms (EA) are the main topic of this paper. In particular, the study aims to present a review of critical aspects of structural damage identification by updating FE model based on evolutionary algorithms. A case study allows the applications of two single objective EAs and one multi-objective EA for FE model updating.

In Schommer et al 2017 (Schommer et al., 2017), a method for a model updating is described. The method is based on the minimization of an objective function that considers both static and dynamic data. The updated model is then used over time for structural damage detection. The method is tested on a single beam of a prestressed concrete bridge where damage is realized by cutting one or more strands.

Standoli et al 2021 (Standoli et al., 2021) present the results of the study conducted on four different isolated masonry bell towers located in the province of Ferrara, Italy. The survey campaigns allowed to update the finite element models (FEM). Dynamic data were developed through the application of two Operational Modal Analysis (OMA) identification techniques: the Enhanced Frequency Domain Decomposition (EFDD) and the Stochastic Subspace Identification (SSI) methodology.

As previously mentioned, recently the research is strongly interested in the use of artificial intelligence algorithms - deep learning DL - for the identification of structural damage. One of the main advantages of the introduction of DL methods in SHM systems is the creation of systems based on deep neural network (DNN) in order to bypass the problem of statistical processes of feature discrimination. In this perspective, many authors aim to define a methodology based on neural networks by investigating among the countless techniques that the field of computer science offers today. For example, Li et al (Li et al., 2006) proposed a comparison of the performance of using a convolutional neural network (CNN) for damage detection on an experimental cable bridge model and those of different methods such as the Support Vector Machine, the Random Forest, k-Nearest Neighbor and the Decision Trees.

Artificial neural networks can be used through two approaches: (i) supervised and (ii) unsupervised. Although not very functional for real applications, many authors use a supervised approach in which there is a need to know the target of data (Bao et al., 2019). The supervised approach can be considered unsuitable for real applications because it requires a great effort of modeling all possible damages that may occur on the structure in order to perform the learning phase of the network through a data set heterogeneous - derived on a numerical basis. In recent years, the interest for the unsupervised approach is growing, in particular through the use of Autoencoder (AE). Pathirage et al. (Pathirage et al., 2018, 2019) proposed several AE-based frameworks to learn the relationship between the dynamic behavior of the structure required in output to the network with its physical properties given in input. Mao et al. (Mao et al., 2021) combine Generative Adversarial Networks (GAN) with the AE to perform unsupervised damage classification based on accelerometric stories transformed into images. Rastin et al. (Rastin et al., 2021) proposed convolutional AE to perform unsupervised damage detection using the AE reconstruction error. Zilong Wang et al (2018) (Cha and Wang, 2018) proposed an unsupervised method based on acceleration signals in which, after a data preprocessing phase based on the application of Continuous Wavelet Transformation (CWT) and Fast Fourier Transformation (FFT) at the raw signals, data is first inserted into an AE to extract significant characteristics for each sensor and then the structural condition is classified by the One Class Support Vector Machine (OC-SVM). The same authors (Wang and Cha, 2021) then proposed an evolution of the method by directly exploiting the raw data.

However, a standard AE performs a deterministic mapping from the input data to their reconstruction, that is, the modeling of the variability of the data in latent representations (An, J., & Cho, 2015) is missing. Unlike the AE, the Variation Autoencoder (VAE) models the distribution parameters of the latent variables thus capturing a greater

variability of the data. In this regard, Ma et al. (Ma et al., 2020) proposed a VAE method based on time domain data to detect structural damage in the SHM field. The proposed method uses the latent representation produced by the VAE encoder to generate a time series of damage indices during the test phase, in order to clearly display a sudden change in the location of the damage. In (Yuan et al., 2021), instead, a method based on a convolutional VAE is proposed as a feature extractor to perform anomaly detection using OC-SVM and Elliptic Envelope (Rousseeuw and Driessen, 1999) on latent representations.

Abdeljaber et al 2017 (Abdeljaber et al., 2017) present a structural damage detection system using 1D convolutional neural networks (CNs) in which there are both the part intended for feature extraction and feature classification. The method allows the detection and localization of damage in real time. A large grandstand simulator is employed for the application of the method. Tests have verified the efficiency of the method in damage detection.

Yi-Zhou Lin et al 2017 (Lin et al., 2017) present a method of automatically extracting damage-sensitive features from low-level sensor data through deep convolutional networks. The deep convolutional neural network is designed to learn features and identify the location of damage on both noise-free and noisy datasets. The method is then compared with another detector that uses wavelet packet energy as the input feature. The application is tested on a numerical case study.

Young-Jin Cha et al 2017 (Cha et al., 2017) discuss image processing techniques (IPTs) for detecting defects in civil infrastructure. These IPTs are mainly used to manipulate images and extract defect features, such as cracks in reinforced concrete surfaces. However, various factors such as variations in light and shadow can affect the result. In order to overcome this problem, the authors propose a method based on convolutional neural networks (CNNs).

Chang et al 2018 (Chang et al., 2018) propose a structural health monitoring strategy using artificial neural networks. In this case, the input parameters are the structure's modal characteristics, i.e., frequency and modal shapes. The dynamic identification required for the extraction of the healthy structure's modal parameters is performed using the technique of stochastic subspace system identification. The results of the identification process are necessary for updating the simplified numerical model of the healthy structure. The neural network must be able to detect the stiffness matrix of the model and then to estimate its changes in the presence of damage. The methodology is analyzed numerically on a seven-story building with two damage scenarios. Finally, it is validated through an experimental test performed on a scaled two-tower building.

Gao 2018 (Gao and Mosalam, 2018) deals with structural damage recognition using images (Structural ImageNet). The network is trained with 2000 labeled images (supervised approach) of concrete columns, beams and nodes. Damages are classified for their extent and severity. Transfer learning (TL) based on VGGNet (Visual Geometry Group) is introduced and applied using a feature extractor and fine-tuning. The methodology is applied to two experimental cases in order to obtain the optimal SIM model.

Pathirage et al 2018 (Pathirage et al., 2018) define a framework based on an autoencoder type deep neural network. The training phase consists of three objectives: (i) preprocessing the data, (ii) reducing dimensionality while preserving the necessary information, and (iii) learning the relationships among the data. Since structural damage-

which results in reduced stiffness-occurs only in a small number of elements in the entire structure, the method also involves sparse regularization of the data.

The accuracy of the method is tested numerically on a steel frame structure and then by laboratory tests on a prestressed concrete bridge.

Cao Vu Dung et al 2019 (Dung and Anh, 2019) propose a method of crack detection in reinforced concrete elements based on deep convolutional networks (FCNs). Three different network architectures - which serve as the backbone of the FCN encoder - were trained for the classification of images on a public dataset. Finally, images extracted from a video of a cyclic load test on a concrete specimen are used to validate the proposed method.

In Luleci et al 2022 (Luleci et al., 2022), the problem of the data amount for the training phase of the deep neural networks for structural damage detection is discussed. The paper describes a generative neural network to generate the data about the structure's damaged condition for the training phase. Specifically, the one-dimensional (1-D) Wasserstein model for convolutional and generative adversarial deep networks (1-D WDCGAN-GP) is adopted to generate damage-associated vibration datasets. Authors show that in cases of insufficient data in DL or ML based damage diagnostics, the 1-D WDCGAN-GP can generate data.

In Yang Yu et al 2019 (Yu et al., 2019), a method based on deep convolutional neural networks is described to identify and localize damage on structures equipped with intelligent control devices. The network is able to automatically extract features from raw signals and to combine them according to the pursued objective i.e., damage identification and/or localization. The network was tested on five-story building equipped with adaptive intelligent isolators and subjected to seismic loading.

Do-Eun Choe et al 2021 (Choe et al., 2021) propose a deep learning (DL) method for structural damage detection tested on floating offshore wind turbines (FOWT). The used networks are recurrent type i.e., with short-term memory (LSTM) and Gated Recurrent Unit (GRU) type i.e., with long-term memory. These network types detect correlations and dependencies among time series data. The simulations consider different damage scenarios with various intensities, locations and forms. Therefore, the real data are related to healthy structure and the simulated ones to damage conditions. The accuracy of K-fold cross-validation of the network and damage detection are above 90%.

Akintunde et al 2021 (Akintunde et al., 2021) proposed indices of damage detected by unsupervised Machine Learning techniques. The study was conducted with data obtained from tests on a full-scale mock-up bridge. The structural response of the bridge subjected to different levels of damage was analyzed namely (i) impact-induced concrete barrier damage; (ii) "saw-cutting" of the entire barrier height; and (iii) extension of saw-cutting through the deck. The damage-sensitive characteristics are Singular Value Decomposition (SVD) and Independent Component Analysis (ICA). The indices were developed using the left singular vectors (LSVs) of the measured response i.e., own orthogonal modes (POM) and independent component modes (ICM). The authors show that an index based on POMs is relatively insensitive to vehicle load and speed variability compared to ICMs.

In Thanh Cuong-Le et al 2022 (Cuong-Le et al., 2022), a damage detection and localization method based on the combination of two techniques namely Particle Swarm Optimization and Support Vector Machine (PSO-SVM) is described. The PSO technique is used to eliminate redundant input parameters and the SVM technique to classify damage. The input data of the network are natural frequencies and mode shapes extracted

from numerical examples of truss and frame structures. The PSO-SVM shows good prediction accuracy for both location and damage level classification.

Lingkun Chen et al 2023 (Chen et al., 2023) develop a deep convolutional neural network (CNN) for the recognition of damage caused by fatigue and ultimate load phenomena for railway bridges. The network's input are images of various bridges in both healthy and damaged condition. The examined damage conditions can be divided into three main categories: concrete cracking, concrete spalling, and reinforcement exposure. The use of transfer learning techniques enabled the training of the AlexNet CNNs with a large amount of data.

Nguyen et al 2023 (Nguyen and Abdel Wahab, 2023) propose the use of Convolutional Neural Networks (CNN and R-CNN) to determine the modal curvature in order to identify damage in steel slab.

The damage indicator is defined as the differences between the 2D curvature of damaged and healthy slabs. Different damage scenarios are created using a finite element (FE) model of the slab. Four damage types were considered i.e., a single small hole, a single large hole, two small holes, and two large holes. The images created from these damage scenarios are then used to train the CNN and R-CNN. Finally, the CNN is able to predict the damage types and the R-CNN is able to delineate the damaged areas. Validation of the method is performed by laboratory testing.

Yongpeng Luo et al 2023 (Luo et al., 2023) define an unsupervised damage detection method based on an improved generative adversarial network (IGAN) and a cloud model (CM). The network is trained only with data in healthy condition. IGAN is an encoder-decoder-encoder generative network for encoding, reconstructing, and recoding the structural response. During the testing phase, the differences between the latent features of the two different encodings (i.e., healthy and damaged condition) can be used to determine the health status of the structure. The CM theory is used to quantify structural damage and to solve the problem of incorrect damage assessment caused by measurement noise. The effectiveness of the damage detection method was verified with the IASC-ASCE Phase I structure.

In this framework, the thesis aims on the one hand to investigate the main techniques of optimal sensor placement by providing a selection criterion of the sensor configuration more appropriate to the identification of the dynamic properties of the structure. On the other hand, a methodology of structural damage detection is proposed exploiting the advantages of using a VAE for anomaly detection.

Unlike other methods, the proposal leverages the ability of the VAE to model the distribution of undamaged data through its probabilistic encoder during the training phase in order to emphasize corrupted data with different distributions. In this way, the distribution is captured by the VAE probabilistic decoder, which reconstructs the data less accurately as the damage increases, because it has been trained to reconstruct only data from the distribution of undamaged data.

Finally, an OC-SVM is adapted to the damage sensitive features extracted from the input data and their reconstruction to classify them as damaged or not.

Damage Detection

Structural Health Monitoring (SHM) is an application of structure monitoring whose objective is to identify the actual health condition of structures in order to detect the presence of structural damage. Damage can be defined as a change in mechanical and/or geometric properties that affects structural behavior and therefore, adversely affects the performance of the structure. Structural damage detection is an application of anomaly detection, and it is based on comparing two different states of the system, one of which is assumed as initial undamaged state.

The focus on procedures for detecting anomalies due to structural damage in civil construction and infrastructure has been growing in recent decades. On the one hand, technological innovation has led to the emergence of "smart structures," i.e., equipped with various embedded sensors that provide real-time information. On the other hand, the need for timely responses to aid the management of the building stock has led to a strong interest in procedures that enable the implementation of a monitoring system. Indeed, the use of monitoring systems allows for continuous and rapid detection of abnormal conditions due to damage.

Specifically, the process of structural monitoring consists of several phases, such as: (i) the executive design of the monitoring system in which all operational aspects of the experimental phase are established such as the sensors' type and number to be used and their location on the structure; (ii) the experimental phase for signal acquisition; (iii) the data processing phase for the extraction of damage-sensitive features; and (iv) the decision-making process by which the ongoing health status of the structure can be detected through the comparison of the extracted features with the healthy condition, established the damage threshold.

The accuracy of the monitoring process can be distinguished by 4 levels listed below (Anders Rytter, 1993):

- Level 1 - The system allows detection of the presence of damage in the structure.
- Level 2 - The system provides information regarding the location of the damage.
- Level 3 - The system provides an estimate of the extent of damage.
- Level 4 - The system provides information regarding the safety of the structure, such as by estimating the remaining life.

The first two levels can be achieved with a data-driven strategy, that is, in the absence of detailed models. Conversely, the achievement of the third and fourth levels is contingent on the use of mechanical models, and it is called a model-based strategy. However, the adoption of models is marred by modeling simplifications and uncertainties that increase with the degree of complexity of the structure.

Referred to dynamic monitoring - based on the analysis of signals from natural or artificial vibrations to detect the dynamic properties of the monitored structure both under operating conditions and during extraordinary events - traditional data analysis techniques can process acceleration, velocity, and displacement signals recorded on the structure in both the frequency and time domains in order to extract damage-sensitive

features. The analysis of structural vibrations induced by natural or man-made actions enables the assessment of dynamic structural characteristics in terms of modal frequencies, modal shapes and damping of a structure.

The assessment of dynamic behavior can be conducted by (i) an analytical approach based on knowledge of the geometry of the structure, boundary conditions and material characteristics and (ii) an experimental approach which allows the calculation of frequency response functions based on measured data from which the dynamic parameters of the structure can be estimated. Modal analysis using an experimental approach can be of two types: experimental modal analysis (EMA) and operational modal analysis (OMA). The former is an investigation technique that assumes the use of artificial excitation. The second, on the other hand, is an investigation technique that uses the excitation produced by the surrounding environment. It allows to determine the dynamic properties of the structure in the case of unknown excitation, which is likened to a zero-averaged Gaussian-type white noise, i.e., a random signal characterized by a constant power spectral density function over all frequencies.

Typical features can be (i) the natural frequency of vibration of the structural system, modal shapes, or modal curvature in the frequency domain; while (ii) in the time domain, they are generally error parameters obtained by comparing the expected condition with the one returned by the regression model.

In this case, structural damage can be identified analyzing the change of extracted features - such as the vibration frequency of the structure - i.e., through the comparison over time with the initial healthy condition.

In both cases, when the damage is not very extensive and/or localized on the structure, it may not cause a change in the features and therefore its identification would not be possible.

In fact, the feature variation must draw on and/or exceed the established damage threshold to identify the presence of damage. The statistical process of the threshold definition must be conducted with special care because it must be calibrated so that it is possible to detect the damage when the structure is in operating condition i.e., in the elastic field.

For this reason, there is an increasing use of artificial intelligence algorithms to bypass the problem of defining damage thresholds through statistical modeling processes that allow the detection of anomalies before they compromise the operation of the structure. In fact, the use of deep learning techniques in the field of civil engineering for structural damage detection has been of increasing interest in recent years. The use of artificial intelligence algorithms is an important resource for big data analysis, reducing uncertainties related to the definition of anomalous thresholds and analysis time.

2.1. Operational Modal Analysis

Modal analysis of a structure can be conducted by two approaches, namely analytical and experimental. The analytical approach is based on knowledge of the structure's geometry, boundary conditions and material characteristics. Basically, the dynamic properties of the structure are derived through solving the equation of motion and the eigenvalues and eigenvectors problem described below. On the other hand, the experimental approach involves estimating the dynamic parameters of the structure through the frequency response functions derived from the data measured on the structure.

Modal analysis using an experimental approach can be of 2 types: (i) Experimental Modal Analysis (EMA) and (ii) Operational Modal Analysis (OMA).

Experimental Modal Analysis (EMA) is an investigation technique that assumes the use of artificial excitation. Specifically, the set of dynamic quantities measured at different points of the structure constitutes "the output," while the amount of energy that stresses the structure (artificial forcing) constitutes "the input." Therefore, in Experimental Modal Analysis (EMA) the dynamic properties of the structure are identified on the basis of the measured output and the known input.

Operational Modal Analysis (OMA) is an investigation technique that exploits the excitation produced by the surrounding environment. It makes it possible to determine the dynamic properties of the structure in the case of unknown excitation, which is likened to a Gaussian-type white noise.

Compared with Experimental Modal Analysis, Operational Modal Analysis has several advantages, such as:

- the test is usually cheaper, since no equipment is needed to excite the structure;
- the test is operationally easier to perform, since fewer devices are placed in place and no external control is required;
- measurements are made under conditions more similar to the operational conditions of the structure, so the modal parameters obtained are representative of the dynamic behavior of the structure under its conditions of use;
- environmental excitation is continuous and permanent; this allows the realization of continuous monitoring of the structure.

However, the disadvantages are:

- the input signal is assumed to be white noise. A violation of this assumption will return additional peaks in the responses that are not an indication of structural modes;
- in some cases, the overall level of ambient excitation may be quite low. If this problem is compounded by a limited amount of available data (so the data are not averaged for sufficiently long times), the results will be affected by noise and the modal parameters returned by the analysis uncertain. In contrast, in the artificial forcing test there is the advantage of controlling the level of forcing and thus the energy input into the structure. This allows, in the case where the forcing is properly designed, the described problem to be avoided;
- given the limited excitation level, uncertainties in the measurement instrumentation can affect the quality of the data, going to disturb the identification of modes.

The main factors influencing the choice between the EMA and OMA techniques are (i) amplitude of the range of survey frequencies; (ii) damping associated with the structure's own modes; (iii) intensity of excitation required for proper detection of structural response; (iv) duration of the test; and (v) economic considerations.

Finally, these techniques are based on the following fundamental assumptions:

- **Linearity:** the principle of superposition of effects applies.
- **Stationarity:** the dynamic characteristics of the structure do not change over time.
- **Observability:** possibility of measuring the data needed to calculate the dynamic characteristics.

For both EMA and OMA techniques, the dynamic behavior of the structure can be characterized by solving differential equations in the time domain or by algebraic equations in the frequency domain. Frequency domain methods provide good results when the analysis is aimed at a wide range of frequencies and many mode shapes must be identified. However, results can be affected by frequency resolution and at losses. In contrast, time domain methods return good results when the frequency range is limited, and few mode shapes need to be extracted.

2.2. Dynamic Identification

Dynamic identification can be used for the detection of the structural health status because the variation of the structure's modal properties can be an indication of the presence of structural damage over time. In particular, the use of the dynamic identification's results can be used for the calibration of the finite element model of the structure. In this case, it is possible to identify, locate and even quantify structural damage through the model updating. In this case, the model-based approach is used. Vice versa, the results can also be used with data driven approach established the damage threshold.

The main methods of dynamic identification in the frequency domain are the Circle Fitting, the Peak Picking, the Frequency Domain Decomposition and the Enhanced Frequency Domain Decomposition.

The basic assumption of the Circle-fit method is that around a structure's eigenfrequency, the inertia function – i.e., the frequency response function defined as the ratio of the Fourier transform of the generic acceleration response to the Fourier transform of the modulus of the applied force - describes a circumference in the Nyquist complex plane. This assumption is correct in the case of the mobility function – i.e., the frequency response function in velocity - with viscous-type damping. For the inertia, the assumption is correct locally i.e., around the eigenfrequency. The procedure then consists of interpolation by circumference of the circle produced by the i -th mode of vibration near the resonant frequency (Ewins, 2000)

Peak Picking uses the self-spectra and cross-spectra of recorded accelerations under the assumption that only one mode is dominant around the resonant frequency. Therefore, the PSD matrix trace contains the peaks corresponding to the structural resonances. The modal shapes associated with the identified frequencies are obtained from the first column of the PSD matrix. The results are accurate if the vibration modes are distinct, and the damping is low (Brincker, R., Zhang, L., & Andersen, 2000).

The Frequency domain decomposition assumption is that each displacement of the structure can be reproduced as a linear combination of the eigenvectors, i.e., the modal forms, since they form a basis, being linearly independent. Therefore, the displacements of the vibration modes of the system can be decomposed. The decomposition is accomplished by the technique of singular value decomposition (SVD) of the power spectral density (PSD) matrix, obtained from the measured data. SVD then allows three matrices to be obtained for each frequency: two matrices of singular vectors that provide information on the modal shapes, and the diagonal matrix of singular values, in which the first value is the intensity of the predominant vibration mode, while the others are representative of the intensity of the noise or vibration modes close to the predominant mode.

An evolution of the FDD method is Enhanced Frequency Domain Decomposition (EFDD). This method returns the modal shapes, frequencies and also the modal damping of the structure. In fact, the signals are first processed by the FDD technique to derive the frequencies and modal shapes. Then they are processed in the time domain to estimate the damping ratio in the selected frequency intervals around a peak.

In this section, the Frequency Domain Decomposition (FDD) is described.

2.2.1. Frequency Domain Decomposition

Frequency Domain Decomposition is an output-only method useful for identifying the vibration frequencies and corresponding modal shapes of a structural system from the accelerations recorded on the structure (output).

The technique is based on the assertion that the eigenvectors, which represent the vibration modes, form a basis because they are linearly independent. So, any displacement of the system can be represented by a linear combination of them, and it is possible to decouple the components of the various modes. This property can be applied to the response of the system, measured at each point where the accelerometer is placed, or to the spectral density (Power Spectral Density, PSD) of the accelerometer history through the Singular Value Decomposition (SVD) of the matrix defined for each frequency ω (Wall et al., n.d.).

The frequencies and modal shapes provided by this procedure are considered valid if the following conditions are met: (i) the excitation is Gaussian white noise with zero mean and unit standard deviation; (ii) the identified modal shapes are orthogonal; and (iii) the structure has a low damping coefficient (Brincker, R., Zhang, L., & Andersen, 2000).

This method exploits frequency response functions (FRFs) from which the eigen periods, damping and modal deformations of the structure can be identified. In particular, the Fourier transform makes it possible to transform the system of differential equations-which governs the dynamic behavior of the structure-to a system of algebraic equations of simpler resolution.

In the flowchart in Figure 2, the data processing procedure through the FDD technique is described step-by-step. Specifically, the first step consists of estimating the PSDs through the Fourier transforms of the signals. Then the PSD matrices - one for each frequency - are decomposed to singular values. The singular values are representative of the degrees of the structural system, while the singular vectors carry the information of the modal forms. Finally, the vibration modes can be selected on the graphical representation of the singular values spectrum at the resonance peaks. In fact, natural frequencies are identified graphically by peak-picking technique. To each identified peak, a singular value is associated to which the singular vectors correspond. The goodness of attribution of a frequency to a mode of vibration is performed through the MAC - Modal Assurance Criteria (Mirsolav et al., 2012; Brigante et al., 2017).

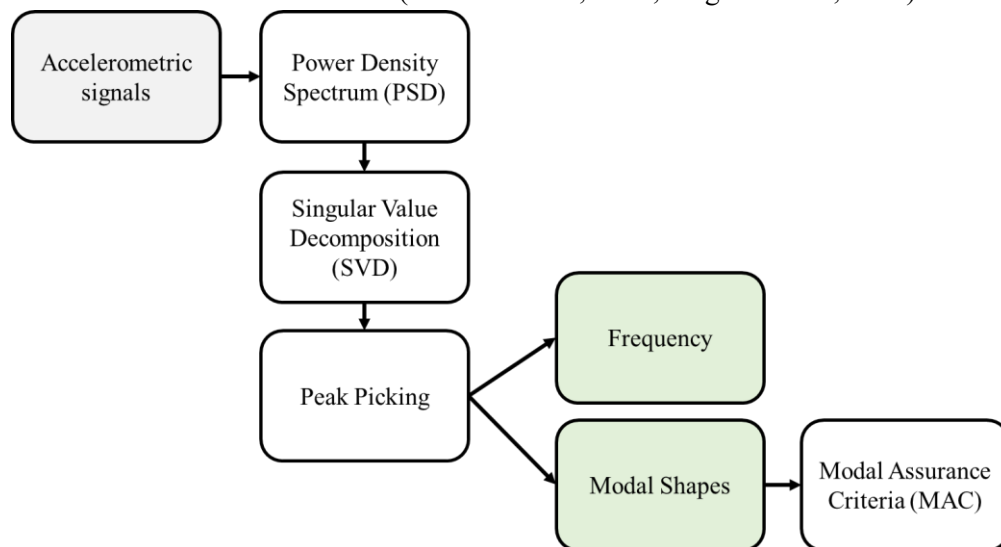


Figure 2 – Flowchart about FDD technique

2.2.2. Modal Analysis

The dynamic behavior of a linear elastic damped and forced spring - carriage system with N degrees of freedom (MDOF) - as in Figure 3 - can be studied by the equation 1. It is the system of differential equations in matrix form that describes the motion of the spring-carriage system in the time domain (Iervolino Iuno, 2021).

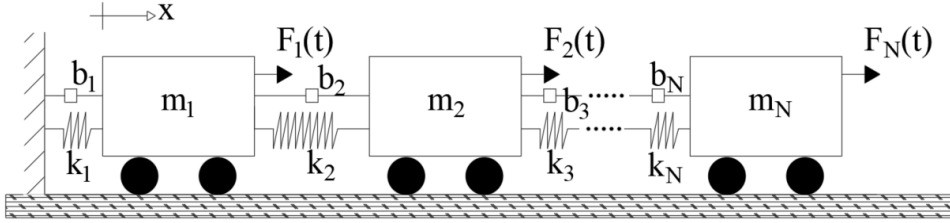


Figure 3 – Elastic spring - carriage system

$$[M]\{\ddot{x}(t)\} + [B]\{\dot{x}(t)\} + [K]\{x(t)\} = \{F(t)\} \quad 1$$

Where $[M]$, $[B]$ and $[K]$ represent the mass, damping and stiffness matrices of the elastic system, respectively. $\{F(t)\}$ is the time-varying external force, and $\{\ddot{x}(t)\}$, $\{\dot{x}(t)\}$ and $\{x(t)\}$ are the unknown acceleration, velocity and displacement vectors that characterize the motion of the system, respectively.

The viscous damper is introduced in the model to take account of non-hysteretic mechanisms associated to energy losses which occur in the response of the elastic systems. Damping is produced by energy dissipation of the vibrating system through various mechanisms, which are associated with the thermal effect of repeated elastic deformation of the material, internal friction and other factors. Specifically, there are four types of damping such as, viscous damping, hysteretic damping, frictional damping and aerodynamic damping. Because of the complexity of the phenomena that produce damping, in models of the dynamic response of a system it is usually idealized by introducing equivalent viscous damping.

The dynamic characteristics of the MDOF system can be identified by a traditional approach i.e., analytical modal analysis and an experimental approach.

Traditional modal analysis is generally performed by considering an unforced system in the absence of damping whose equation of motion is:

$$[M]\{\ddot{x}(t)\} + [K]\{x(t)\} = \{0\} \quad 2$$

Assuming that $\{x(t)\} = \{\varphi_n\} [C \cos(\omega t - \Phi)]$ where $\{\varphi_n\}$ is the vector of modal shapes, the vibration modes and the natural frequencies are obtained by solving the eigenvalue problem associated to Eq. 2, namely:

$$([K] - \omega_n^2 [M])\{\varphi_n\} = \{0\} \quad 3$$

The set of equations expressed through Eq. 3 has two solutions: a trivial solution $\{\varphi_n\} = \{0\}$ and a nontrivial one such as:

$$\det([K] - \omega_n^2 [M]) = 0 \quad 4$$

The characteristic equation or frequency equation expressed through Eq. 4 has N real and positive roots for ω_n^2 , since [M] and [K] are symmetric and positively defined matrices. These roots are related to the natural frequencies of the system, and they are the eigenvalues of the problem. The N independent vectors corresponding to the N natural frequencies are known as eigenvectors and represent the natural modes of vibration.

Instead, the experimental approach uses the Fourier transform to solve the equation of motion (Eq. 1). In this case, the approach considers the structural system in its complexity i.e., with external forcing and viscous damping.

Using the Fourier transform (FFT) of the function $\{x(t)\}$ and its property for derivatives (see eq. 5), with reference to the j-th pulsation ω_j , the system of differential equations can be written as in equation 6.

$$\{X(\omega)\} = \mathbf{FFT}(\{x(t)\}) = \int_{-\infty}^{+\infty} x(t)e^{-i\omega t} dt \rightarrow \mathbf{FFT}\left(\frac{d^n x(t)}{dt^n}\right) = (i\omega)^n X(\omega) \quad 5$$

$$(-\omega_j^2[M] + i\omega_j[B] + [K]) \cdot \{X(\omega_j)\} = \{F(\omega_j)\} \quad 6$$

$\{X(\omega_j)\}$ and $\{F(\omega_j)\}$ are the Fourier transform of the structural response $\{x(t)\}$ and the system input forcing $\{F(t)\}$, respectively.

The FRF transfer function for the generic pulsation ω_j - $[H(\omega_j)]$ - is represented by equation 7 (or 8). It is obtained as the inverse matrix of the sum between three factors that are a function of the mass, the damping, and the stiffness matrix, respectively.

$$[H(\omega_j)] = \{X(\omega)\}/\{F(\omega)\} = (-\omega_j^2[M] + i\omega_j[B] + [K])^{-1} \quad 7$$

By applying mathematical manipulations explained in more details in Rainieri and Fabbrocino (Rainieri and Fabbrocino, 2014), Heylen et al. (Heylen et al., 1998), or in Ewins (Ewins, 2000), the FRF can be expressed as a function of modal parameters as follows:

$$[H(\omega)] = \sum_{r=1}^N \frac{[R_r]}{i\omega - \lambda_r} + \frac{[R_r]^*}{i\omega - \lambda_r^*} = \sum_{r=1}^N \frac{Q_r \{\theta_r\} \{\theta_r\}^T}{i\omega - \lambda_r} + \frac{Q_r^* \{\theta_r\}^* \{\theta_r\}^{*T}}{i\omega - \lambda_r^*} \quad 8$$

where N is the number of modes, $\{\theta_r\}$ is r-th mode shape, Q_r holds information about the modal scaling factor, λ_r is the pole of the r-th mode and provides information about damped frequency and damping ratio of the r-th mode of vibration.

Ultimately, the modal characteristics of the structural can be identified through the experimental approach from the FRF function i.e., known structural responses $\{X(\omega)\}$ and forcings $\{F(\omega)\}$

2.2.3. Power Spectral Density and Singular Value Decomposition

As mentioned above, the FDD method is based on estimating PSDs through the Fourier transforms of the recorded signals. These PSD matrices-one for each frequency-are then decomposed into singular values. The singular values are representative of the degrees of the structural system, while the singular vectors carry the information of the modal shapes.

The spectral density matrices can be derived from the equation of motion of the MDOF system in the frequency domain (Eq. 9) reproduced below.

$$(-\omega_j^2[\mathbf{M}] + i\omega_j[\mathbf{B}] + [\mathbf{K}]) \cdot \{X(\omega_j)\} = \{F(\omega_j)\} \quad 9$$

Pre-multiplying both members of equation 6 by the inverse of the H-matrix, the result is showed in compact form by the eq. 10:

$$[I] \cdot \{X(\omega_j)\} = [H(\omega_j)] \cdot \{F(\omega_j)\} \quad 10$$

Where $[I]$ denotes the unitary matrix.

Defined the convolution product between two generic signals $\{a(t)\}$ and $\{c(t)\}$ by eq. 11:

$$G(t) = \{a(t)\} \cdot \{c(t)\} = \int_{-\infty}^{+\infty} a(t + \tau)c(t)d\tau = E[a(t + \tau)c(t)^T] \quad 11$$

The convolution theorem can be exploited to derive the response of a linear system in the frequency domain. In fact, the convolution theorem states the Fourier transform of the convolution of two functions $FFT(\{a(t)\} \cdot \{c(t)\})$ is the product between the transform of the first function $\{A(\omega)\}$ and the conjugate of the transform of the second $\{C^*(\omega)\}$. Therefore, the response of any linear system $\{x(t)\}$ can be studied as the convolution product between the forcer $\{F(t)\}$ and the transfer function in the time domain $\{H(t)\}$, confirming the eq. 10.

Assuming that S sensors are available on the structure with which acceleration signals $x(t)$ are acquired with a given sampling rate, the power density spectrum (PSD) consists of N matrices S x S - one for each frequency in the examined range - having on the main diagonal the Fourier transform of the autocorrelation function and outside the diagonal the transform of the cross-correlation function.

The autocorrelation function $R_{x_i x_i}$ is defined as the convolution product of signal $x_i(t)$ with itself, While the cross-correlation function $R_{x_i x_k}$ is the convolution product between the two signals $x_i(t)$ and $x_k(t)$.

Then, the generic element of the PSD matrix for a given pulsation ω_j is represented by the equation 12 for terms on the main diagonal and the equation 13 for the terms off the diagonal.

$$W_{x_i x_i}(\omega_j) = FFT(R_{x_i x_i}) = FFT(x_i(t) \cdot x_i(t)) = X_i(\omega_j)X_i^*(\omega_j) \quad 12$$

$$W_{x_i x_k}(\omega_j) = FFT(R_{x_i x_k}) = FFT(x_i(t) \cdot x_k(t)) = X_i(\omega_j)X_k^*(\omega_j) \quad 13$$

The spectral density matrix (PSD) can be related to the forcer - or rather to the PSD of the force - and the FRF function. Referred to a generic signal $x_i(t)$, the generic element of the main diagonal of the PSD matrix can be written as in equation 14. Conversely,

outside the main diagonal, the power spectrum associated with two distinct signals $x_i(t)$ and $x_k(t)$ is described by equation 15.

$$W_{X_i X_i}(\omega_j) = X_i(\omega_j)X_i^*(\omega_j) = |H_{X_i}(\omega_j)|^2 W_F(\omega_j) \quad 14$$

$$W_{X_i X_k}(\omega_j) = X_i(\omega_j)X_k^*(\omega_j) = X_i^*(\omega_j)X_k(\omega_j) = H_{X_i}(\omega_j)H_{X_k}^*(\omega_j)W_F(\omega_j) \quad 15$$

Singular Value Decomposition is a matrix factorization technique by which any matrix can be represented as the product of two orthogonal matrices and one diagonal.

Singular Value Decomposition (SVD) applied to spectral density matrices - one for each frequency - allows to derive three matrices: (i) a diagonal one $[\Sigma]$ containing the singular values (s_1, s_2, \dots, s_S) , the first of which represents the intensity of the predominant mode, and (ii) two matrix $[U]$ that represent the intensity of the noise or modes close to the dominant one.

The singular values are the spectral densities of the one-degree-of-freedom systems and in fact are equal to the number of accelerometers. The other two matrices $[U]$ contain the singular vectors $(\{u_1\}, \{u_2\}, \dots, \{u_S\})$ that carry with them the information of the relevant modal forms (see eq. 16).

$$[W(\omega)] = [U] \cdot [\Sigma] \cdot [U]^*$$

$$\text{with } [U] = [\{u_1\} \quad \{u_2\} \quad \dots \quad \{u_S\}] \quad \text{and} \quad [\Sigma] = \begin{bmatrix} s_1 & 0 & 0 & 0 \\ 0 & s_2 & 0 & 0 \\ 0 & 0 & \dots & 0 \\ 0 & 0 & 0 & s_S \end{bmatrix} \quad 16$$

2.2.4. Modal Assurance Criteria

MAC (Mirsolav et al., 2012) is one of the main strategies for quantitative comparison of modal shapes. It is a criterion to assess the consistency of the experimental results with numerical values derived from a FE model. This criterion allows to verify that the frequencies - identified by the PSD peaks - correspond to real vibration modes of the structure by comparing the experimental results with the reference ones obtained by the FE model.

The MAC matrix has dimensions $M \times M$ - if M indicates the number of identified modes - and it is constituted by scalar numbers between 0 and 1. This matrix is obtained by the eq. 17.

$$MAC_{ij} = \frac{|\{\varphi_{num}^j\}^T \{\varphi_{sp}^i\}|^2}{\{\{\varphi_{num}^j\}^T \{\varphi_{num}^j\}\} \{\{\varphi_{sp}^i\}^T \{\varphi_{sp}^i\}\}} \quad 17$$

Where $\{\varphi_{num}^j\}$ indicates the modal shape of the j -th mode obtained from an analytical modal analysis (performed with FE model) and the experimental one $\{\varphi_{sp}^j\}$.

As mentioned, MAC can take values between 0 - when modal shapes are independent or unrelated - and 1 - when there is total correlation.

2.3. Model Updating

The design and safety checks of structures generally require a mathematical based on the finite element method (FE) that represents the physical behavior of the structure. However, in the case of complex structures such as bridges and viaducts, the initial FE model may not match the actual behavior of the structure. In fact, despite the importance and complexity of these structural types, often in practice, existing bridges are analyzed using simplified structural models. So, inaccuracies arise from a series of simplifying assumptions underlying FE modeling.

Therefore, the update of the numerical model on the basis of the results of site tests (static and dynamic load tests) allows to calibrate the theoretical behavior and, thus, matched it to the actual behavior (Schommer et al., 2017).

In addition, the updated FE model can be used as a facility management tool providing useful information on the health status of the structure and allowing to record information on the evolution of the structuring degradation. Therefore, it can be used to improve the planning of management and maintenance plans.

Unlike data driven techniques, this process makes it possible to detect and localize the damage, but above all to quantify it in terms of extent and severity. Finally, the updated model can be an aid for the analysis of the prediction of the evolution of degradation based on recorded historical data or previous comparisons with experimental data.

Figure 4 summarizes the process of damage detection by exploiting the updated FE model.

When a model-based approach is used in the structural monitoring process, two phases must be distinguished:

- the first at time $T = 0$ in which on-site tests are needed to verify the correspondence between the actual behavior of the structure and the simulated one by FE model.
- in the second phase ($T \neq 0$), however, tests are used to verify the healthy condition of the structure.

Thus, the basic assumption is that at $T = 0$, the structure is considered in a "healthy" condition after appropriate testing.

The first update phase should be performed when there is no match between model and real structure in order to make the numerical behavior equal to the real one.

In the second stage, when the real behavior is different from the modeling behavior, the detected anomaly could be a symptom of damage. Therefore, it is necessary to investigate about the type of damage and its location during the updating process. Eventually, through the updated numerical model, it is possible - through statistical prediction models - to predict the evolution of the damage.

In general, model updating techniques can be divided into two macro categories:

- with physical interpretation in which the variation of the parameters of mass and stiffness of the model is subject to the physical interpretation of the problem
- automatic technique based on genetic algorithms in which the matrices of mass and stiffness of the model are varied until the perfect correspondence between experimental and numerical results is obtained.

Following, the model updating will be implemented through a procedure to physical interpretation considered more appropriate here.

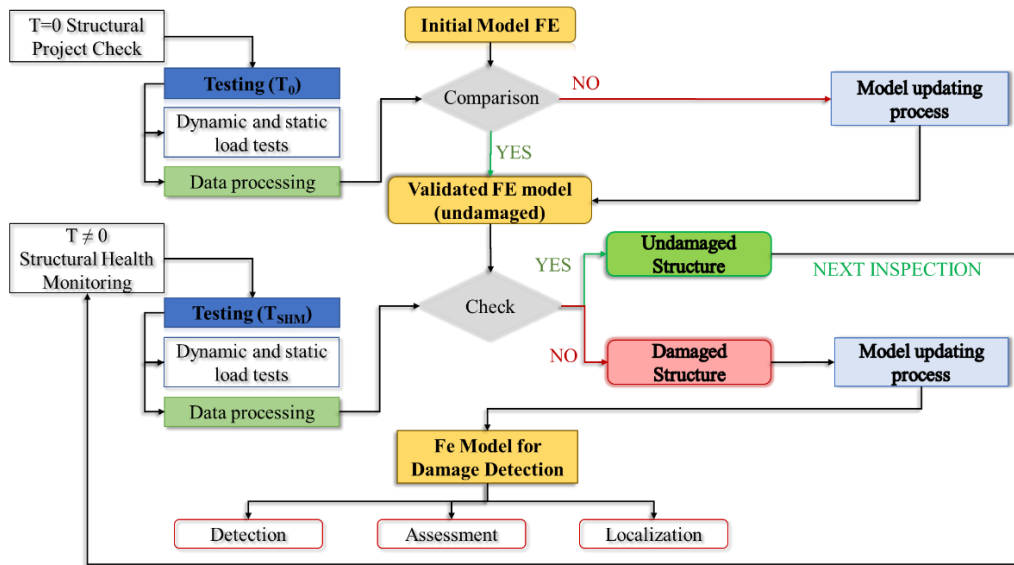


Figure 4 – Flowchart Model Updating

2.4. Artificial Intelligence

Artificial Intelligence (AI) studies some techniques and methodologies aimed to the design of systems that can task activities without the human interaction. These systems are able to learn from experience in order to improve their performance to optimally achieve the purpose for which they were designed. Most applications in the field of Artificial Intelligence, are related to different technologies, including "Machine Learning" and "Deep Learning" (Sujith et al., 2022). AI-based systems allow: (i) to automate repetitive processes of learning and searching within data, reducing the chance of error; (ii) to learn and improve their performance by processing data continuously over time; and (iii) to provide very high accuracy by processing a large amount of data in relatively little time.

Deep Learning is a branch of Artificial Intelligence whose aim is to automate the construction of analytical models. The basic idea is that systems are able to learn from data in order to autonomously classify the features without categorization from outside. The training phase affects the system's ability to solve the problem. Training must be performed so that the system learns the mathematical relationships between input and output. In this way, the system will perform in achieving its goal in terms of analysis time and goodness of results.

Deep Learning is based on the use of Artificial Neural Networks. Such networks can be characterized by two types of learning namely supervised or unsupervised learning. In the first case, in the training phase of the algorithm it is necessary to have labeled data i.e., input - target pairs. Later, in the testing phase, the algorithm will be able to process unknown i.e., unclassified datasets. In unsupervised learning, on the other hand, the training dataset is unlabeled. Therefore, the algorithm is able to detect a "hidden" structure in the provided dataset, enabling its classification.

In the field of civil engineering, possible applications of artificial intelligence are (i) Construction Design and Optimization; (ii) Structural Monitoring; and (iii) Decision-Making Support.

Referred to the last two possible applications, the use of deep learning techniques is gaining more and more prominence. In the field of anomaly detection, the adoption of artificial neural networks allows - through the adoption of a data-driven strategy with an unsupervised approach - to identify structural damage without the use of a numerical model. In added, it would allow bypassing the problem of defining anomalous thresholds and related uncertainties (Pollastro et al., 2023).

2.4.1. Artificial Neural Networks

Artificial Neural Network (ANN) is a computational model characterized by artificial neurons that is inspired by the human neural network (Yegnanarayana, 2009). The typical structure of ANN is characterized by a series of interconnected neurons (or nodes) that trigger a response based on the information to be processed. The neurons are organized into interconnected layers: (i) input layers, (ii) hidden layers, and (iii) output layers. For each layer, there are a certain number of neurons that can be optimized in order to maximize the learning quality of the network according to the intended purpose. Each neuron interacts with those in the next layer by summing stimuli from neurons belonging to the previous layers. Each neuron can receive input signals from many other nodes; however, it only processes one local information. In fact, a node is activated only according to the information it receives through its connections, but it does not know the

overall purpose of the network, or the operations performed by other nodes. Connections between neurons are weighted because a weight is associated to the each one. The weight represents the strength of the connection, i.e., its influence in the network.

If the generic neuron i belongs to the generic layer k and it is characterized by j connections with other neurons having weight w , the output a_{ik} of the neuron is given by equation 18.

$$a_{ik} = f(\sum_j w_{ij}^{k-1} a_j^{k-1} + b) \quad 18$$

Where f indicates the activation function of neuron i .

The main activation functions include (i) sigmoid limited in the interval $[0; 1]$; (ii) the step function, (iii) the hyperbolic tangent; and finally, (iv) the linear function.

Each neuron is characterized by the activation function f and an activation threshold. The latter is usually introduced by a constant input called bias (b). The purpose of the bias is to control the translation of the threshold.

About structure, artificial neural networks can be classified: (i) by memory capacity and (ii) by number of hidden layers (multilayer or monolayer). In the presence of internal loops in the network, we speak of recurrent networks and the output of the generic neuron depends not only on the current input but also on its historical memory (current input); Conversely, we speak of feedforward networks and the output of the neuron depends only on the current input.

The successful resolution of a problem through the Artificial Neural Network depends on the training phase for defining the set of Hyper-Parameters-especially weights and biases.

The use of the Neural Network requires three phases:

- Training: in which the weights and bias are varied in order to achieve higher network performance.
- Validation: in order to test the performance of the network on different data from the training data. This phase allows to avoid the overfitting issues.
- Testing: i.e., the application of the network on a dataset in order to obtain the desired output.

The aim of the training phase is to determine the set of parameters (weights and biases) so that the network is able to build the best analytical model. Validation, on the other hand, is a phase of validating the training performance.

The training process (training and validation) ends when: (i) the desired performance is achieved; or (ii) the imposed time limit is exceeded; (iii) or in case of overfitting. Overfitting is a condition in which the network fails to extrapolate the mathematical function between data, but it learns the data itself and thus fails to generalize the problem. The most popular training process is the "Gradient Descent Method." This method is based on the definition of a cost function (see eq. 19), which represents the error associated with each output neuron.

$$Cost = \sum_{i=1}^n (Output_i - Target_i)^2 \quad 19$$

The method consists of minimizing the cost function according to the gradient of descent to find the global minimum of the function. The problem is n -dimensional since the set of n -weights that minimizes the cost function must be found (where " n " means the

number of connections associated with the network). The process is iterative, and it is generally called backpropagation of error. At each step the cost function gives the error between the output obtained and the expected output. Then, the weights are varied in order to minimize the cost function i.e., the error.

2.5. Methodology

In this work, a framework to perform an unsupervised damage detection using a VAE followed by a OC-SVM is described (Pollastro et al., 2023). The main aim is to identify the presence of damages and to assess the results in terms of a binary classification response (healthy or damaged structure). The unsupervised approach is realized by training the network on the basis on only normal data, thus avoiding studies the use of FE models.

The Variational Autoencoders (VAE) (Ma et al., 2020) is a probabilistic generative model that aims to simulate the data generation process. Conversely, discriminative ones (the classical VA) learn to make predictions but fail to understand the causal relationships between data. correspond to neural networks logically divided into two components, an *encoder* and a *decoder*. An encoder receives training or test input, and it generates not a simple vector in latent space, but a multivariate normal distribution described in terms of mean and variance. The decoder receives as input a vector sampled on the distribution generated by the encoder, and it generates an output as close as possible to the input processed by the encoder.

In this case, the variational auto-encoder is trained only on healthy data, so that the network learns the natural structure behavior (healthy condition). Thus, in the testing phase, when data may also be anomalous due to damage on the structure, there will be an incorrect reconstruction of the data by the probabilistic decoder. In fact, the basic assumption is that the latent distributions learned by VAE during training on undamaged data are different from what the damaged data would have. Therefore, the raw data - recorded on the healthy structure - are inputs of the VAE and they are divided between training datasets for network learning and testing datasets. Next, the extraction of damage-sensitive features is performed by comparing the original and reconstructed signals. The damage-sensitive features employed are:

Mean Squared Error (MSE), that measures the reconstruction error between the input acceleration signals and their reconstruction (eq. 20):

$$MSE = \sum_{i=1}^n (x_i - \bar{x}_i)^2 \quad 20$$

where n is the number of the signal features, x_i is the i -th feature in the original signal and \bar{x}_i is the i -th feature in the reconstructed signal.

Original-to-Reconstructed-Signal Ratio (ORSR), computed as (eq. 21):

$$ORSR = 10 \cdot \log_{10} \frac{\sum_{i=1}^n x_i^2}{\sum_{i=1}^n \bar{x}_i^2} \quad 21$$

that represents the ratio in decibels between the magnitudes of the original signal and its reconstruction.

Considering input data (i.e., the damage-sensitive features) as points defined in a vector space, a Support Vector Machine (SVM) is a two-class method which classifies data according to a decision hyper-plane that maximizes the separation between the two classes. In order to detect damages in a monitored structure, the use of a SVM implies that data of both undamaged and damaged structure must be available during the training stage. A One-Class Support Vector Machine (OC-SVM), instead, is a method that requires only data related to one class to train the model. For OC-SVM, the main aim of

the training stage consists in finding the smallest hyper-sphere including most of the training samples. Figure 1 shows a graphical representation of the proposed architecture. Data are firstly fed into a VAE. Then, using original and reconstructed signals, after a feature extraction stage, data are fed into an OC-SVM for being classified as damaged or not. Finally, features are classified by the OC-SVM (see Figure 5) as damaged or not. The OC-SVM is a binary classifier, and it is trained equally labelled data. In this case, using only undamaged data during the training phase, the OC-SVM creates a decision hypersphere that allows new data to be classified as healthy or damaged.

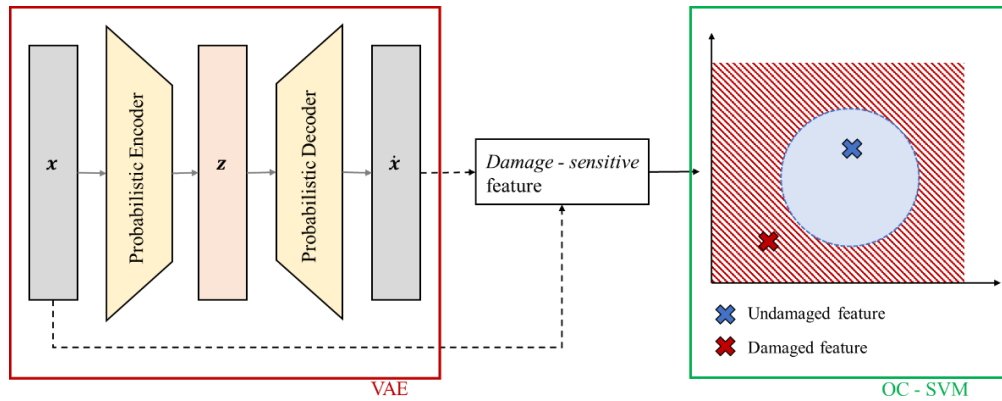


Figure 5 – Flowchart of the methodology

2.6. The case studies

2.6.1. Steel frame

The case study consists in a steel frame tested in Phase II of the SHM benchmark problem, whose results were published in 2003 by the International Association for Structural Control (IASC) American Society of Civil Engineers (ASCE) Structural Health Monitoring Task Group. The frame is a four-story steel structure built at the University of British Columbia (Figure 6). The dimensions are 2.5 m 2.5 m in plan, and the total height is 3.6 m. The structural elements are hot-rolled, grade 300W steel. The columns are B100x9 sections and beams are S75x11. In each span, the bracing system is composed of two threaded steel bars with a diameter of 12.7 mm and inserted along the diagonal. To make the mass distribution reasonably realistic, four slabs of 1000 kg are in the first, in the second and in the third floors, while slabs of 750 kg were used on the fourth (see Figure 7). Further information can be read in (D. Bernal, S. J. Dyke, H.F. Lam, 2002).



Figure 6 – Case study

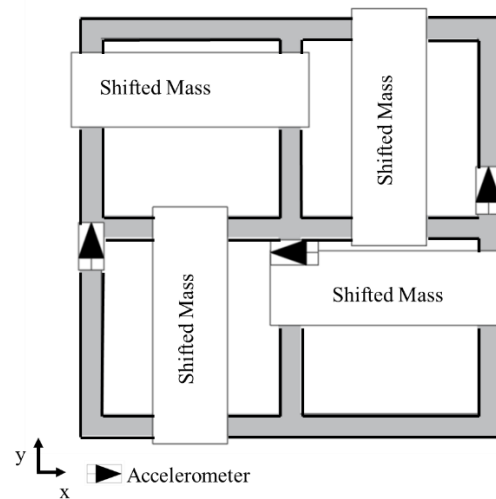


Figure 7 – Masses distribution

12 accelerometers were placed on the structure as shown in Figure 8. On each floor, 4 accelerometers were installed on the West, the East and on the central column. All sensors are monoaxial: the accelerometers located on the west and on the east columns are oriented along the +X direction, while those on the central column are oriented along the +Y direction. In this thesis, the signals are caused by shaker excitation, i.e., a band-limited white noise with components between 5–50 Hz.

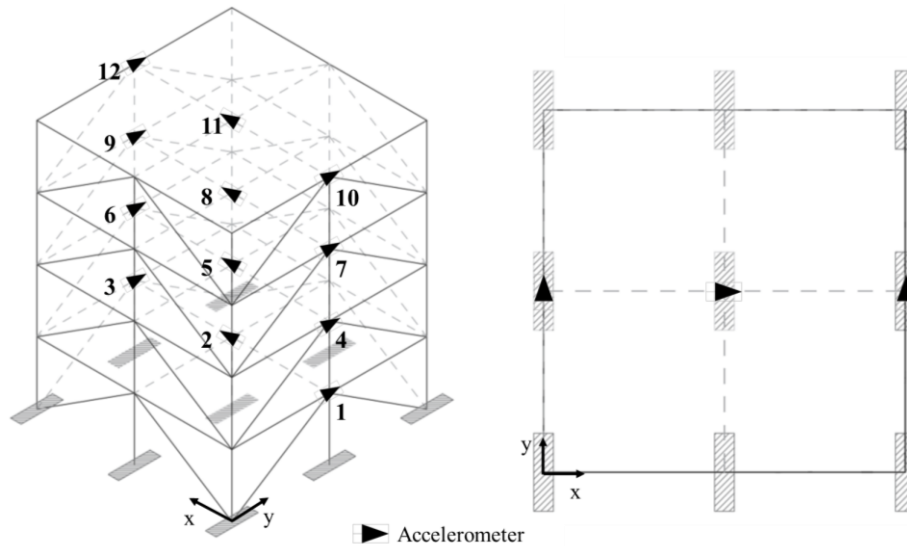


Figure 8 – Sensors' position and orientation

Accelerations were recorded in the absence (Case 1) and in the presence of structural damage. Eight cases of damage were simulated. Table 1 and Figure 9 summarize the various damage scenarios in which the intensity gradually increases from Case 2 to Case 9. The simulated structural damage consists in the removal of diagonal stiffening elements in Cases 2 to 7, while the loosening of the connecting bolts is added in Cases 8 and 9.

Table 1 – Damaged cases

N.	Description
1	Not damaged
2	On the second floor, the diagonal element is removed in a span
3	On the first and fourth floors, diagonal elements are removed in a single span
4	Diagonal elements are removed in a single span
5	The diagonal elements in the east frame are removed
6	The diagonal elements in the east frame and on the second floor in the north frame are removed
7	All diagonal elements are removed
8	Case 7 + loosening of connection bolts for two beams
9	Case 7 + loosening of connection bolts for all beams in the east frame

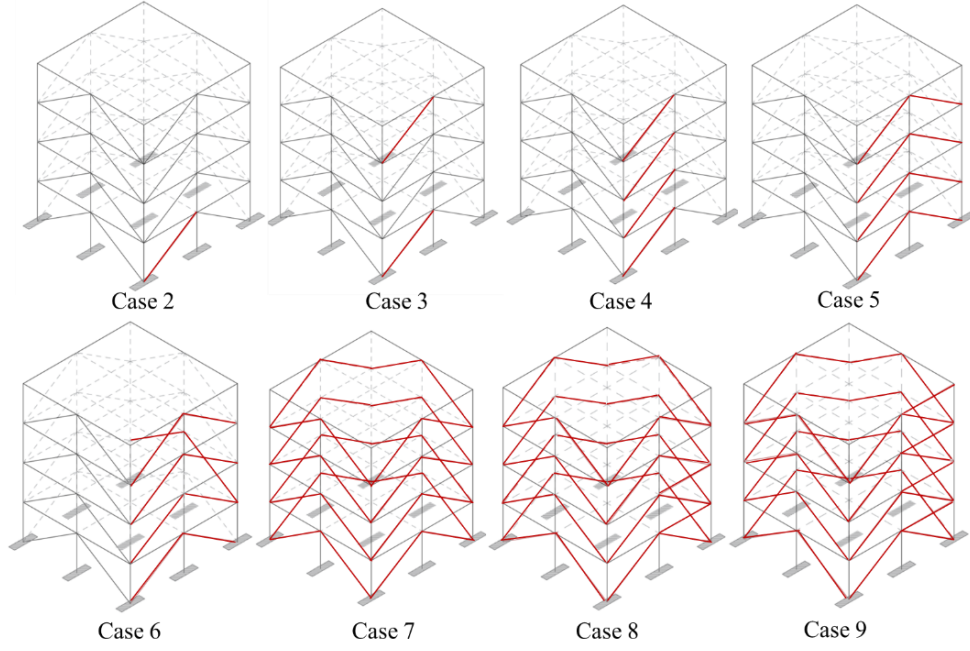


Figure 9 – Damaged cases

Each damage case S_i , with $1 \leq i \leq 9$, was considered as a set of signals collected by n sensors $S_i = \{S_{i1}, S_{i2}, \dots, S_{in}\}$. Each signal S_{ij} of length j_d , with $1 \leq j \leq n$, was divided in several frames having the same length s (eq. 22).

$$S_i = \{S_{ij_1}, S_{ij_2}, \dots, S_{ij_{n_{ij}}}\} \text{ where } n_{ij} = j_d/s. \quad 22$$

Acceleration measurements obtained from random shaker excitation under 5–50 Hz were used. Acceleration measurements were sampled at 200 Hz. Data were measured for 120 s for Cases 1 - 5, 300 s in Case 6 and for 360 s in the remaining cases. As it was explained above, an architecture for each accelerometer was trained, using only undamaged data (Case 1). A length of $s = 128$ was considered to divide each signal in frames, thus obtaining 187 frames for Cases 1 - 5, 468 frames for Case 6 and 562 frames for Cases 7 - 9.

Figure 10 and Figure 11 show a graphical representation of an undamaged (i.e., Case 1) and a damaged (i.e., Case 7) signal reconstructed by a VAE. Note that in the presence of damage, the reconstructed signal is very different from the original one. Instead, in the absence of damage, the error is reduced. Therefore, error metrics are good features to detect the health status of the structure.

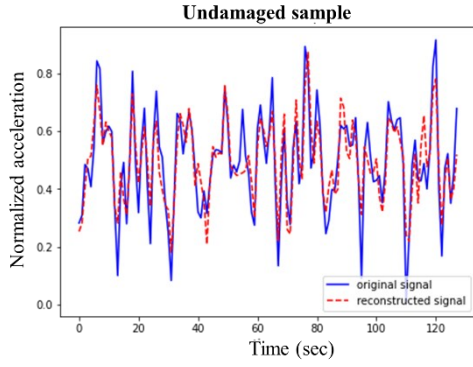


Figure 10 – Comparison between output of VAE and target, healthy case

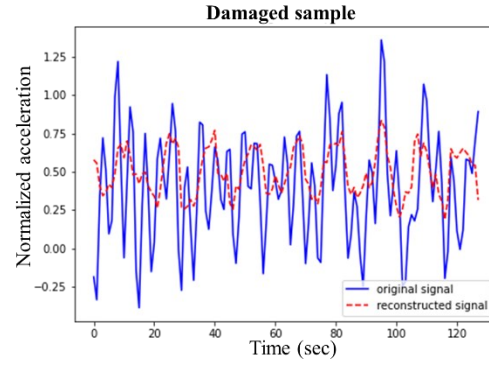


Figure 11 – Comparison between output of VAE and target, damaged case

Figure 12 and Figure 13 show a graphical representation of a OC-SVM fitted on undamaged (Case 1) training data and tested on undamaged test data. OC-SVM allows to distinguish the two health conditions of the structure or healthy and damaged condition. All points within the domain define the healthy condition, while external points identify a damaged condition. SVM training is performed only with reference to healthy data.

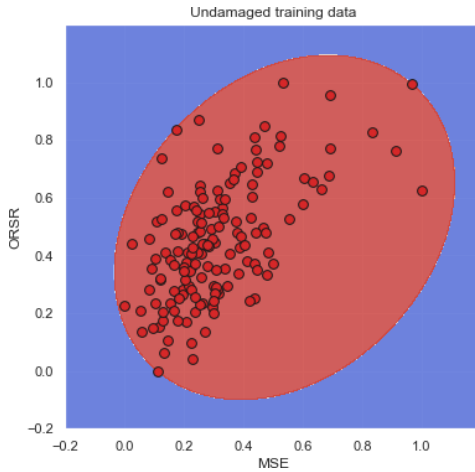


Figure 12 – OC – SVM domain, healthy case

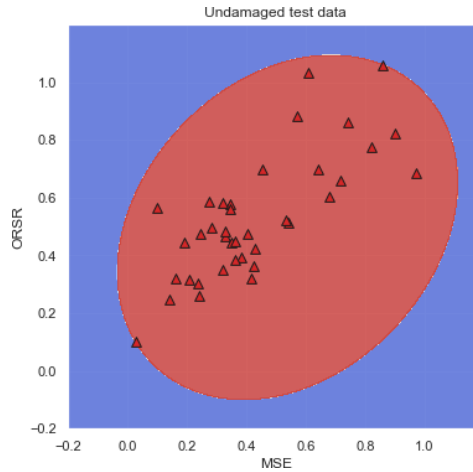


Figure 13 – OC – SVM domain, damaged case

For each set S_{ij} , the probability of damage (PoD) was computed as follows (eq. 23):

$$PoD_{ij} = \frac{d_{ij}}{n_{ij}} \cdot 100 \quad 23$$

where d_{ij} is the number of samples classified as damaged by the OC-SVM. Finally, the overall structure score for each case S_i was computed by averaging the PoD values of each sensor (eq. 24):

$$PoD_{avg_i} = \frac{(\sum_{j=1}^n PoD_{ij})}{n} \quad 24$$

A low value of PoD_{ij} indicates a low probability that the signal i recorded by the j -th sensor belongs to an undamaged state. On the other hand, a high value indicates a high

probability of belonging to damaged state. Same observations are valid for the $PoD_{avg,i}$ value.

Experimental results are reported in Table 2. PoD_{avg} values reflect the a priori known damage conditions of the structure: damage probability is low for Case 1 (i.e., undamaged case), while it is high for all the remaining cases (i.e., damaged cases). Focusing on the damaged cases, PoD_{avg} values higher than the $\sim 89\%$ are always reached, except for Case 2 and Case 6, where PoD_{avg} values of $\sim 70\%$ resulted as outcome. In Case 2, PoD_{avg} is decreased by the PoD values related to the central sensors. However, these PoD values are plausible since central sensors were oriented in the +Y direction while the damages were simulated in the +X direction, thus preventing the damage identification.

Table 2 - Results

Id. Sensor	Case 1	Case 2	Case 3	Case 4	Case 5	Case 6	Case 7	Case 8	Case 9
1	0.00	99.47	100	100	100	98.72	100	100	100
2	5.26	8.02	100	100	100	72.65	100	100	100
3	15.79	100	100	100	100	100	100	100	100
4	2.63	100	100	100	100	100	100	100	100
5	7.89	37.97	100	99.47	100	96.37	33.09	100	100
6	10.53	98.93	100	100	100	13.25	100	100	100
7	0.00	96.79	100	100	100	10.27	100	12.27	37.72
8	2.63	4.28	97.86	100	96.26	13.46	58.89	52.31	99.47
9	0.00	98.93	100	100	100	100	100	100	100
10	0.00	81.28	100	100	100	100	99.82	100	100
11	10.53	17.11	100	100	100	46.58	100	100	100
12	0.00	100	100	100	100	100	100	100	100
PoD_{avg}	4.61	70.23	99.82	99.96	99.69	70.94	90.98	88.72	94.77

According to the definition of PoD , the method correctly detects damaged cases with a high probability and the undamaged case with a low probability. So, the PoD values can be interpreted as the probability of belonging to the undamaged or damaged state.

Under the assumption that the generating distributions of the corrupted data are different from those of the undamaged data, the proposed methodology aims to learn the latent distribution of the undamaged data in order to induce the probabilistic encoder to encode the damaged data with different generating distributions. As a result, the probabilistic decoder is unlikely to decode data from distributions other than those learned during the training phase, resulting in a high reconstruction error. In order to check how much the generation distributions of the damaged data diverge from those of the undamaged data, the Kullback–Leibler (KL) divergences (Bu et al., 2018) are presented in Table 3.

Table 3 - Results

Id. Sensor	Case 2	Case 3	Case 4	Case 5	Case 6	Case 7	Case 8	Case 9
1	0.069	0.068	0.088	0.085	0.21	0.225	0.214	0.215
2	0.048	0.048	0.05	0.056	0.172	0.192	0.192	0.192
3	0.063	0.066	0.088	0.075	0.183	0.205	0.214	0.204

4	0.043	0.046	0.058	0.052	0.166	0.203	0.191	0.196
5	0.049	0.049	0.051	0.056	0.18	0.193	0.193	0.193
6	0.041	0.038	0.04	0.042	0.16	0.192	0.185	0.187
7	0.039	0.04	0.042	0.047	0.162	0.187	0.187	0.187
8	0.065	0.066	0.069	0.073	0.192	0.208	0.215	0.205
9	0.044	0.046	0.056	0.052	0.167	0.192	0.192	0.192
10	0.051	0.052	0.057	0.063	0.176	0.198	0.197	0.197
11	0.053	0.055	0.055	0.062	0.181	0.195	0.196	0.196
12	0.045	0.045	0.046	0.055	0.172	0.192	0.191	0.192
KL _{avg}	0.051	0.052	0.058	0.06	0.177	0.198	0.197	0.196

The KL divergences for each sensor and each damage scenario compared with the healthy case are presented in the table.

The last row, on the other hand, shows the average KL divergence across all sensors.

The KL divergence quantifies the difference between two probability distributions. The mean KL values increase as damage increases (from case 2 to 9). Therefore, the latent distributions of damaged data diverge from the healthy case as damage increases. This confirms the initial hypothesis.

This aspect suggests that the latent representations become harder from EVA as damage increases, and the extent of damage is implicitly suggested in the damage identification process of our architecture.

To make a direct comparison between the capability of the described method and the usual dynamic identification techniques for structural damage detection, the procedure was also applied when the steel frame is excited by white noise. In this case, the results are shown in Table 4. We note that, the percentage of points outside the domain for the healthy case is reduced from 4.61% to 2.48%. In the damage cases, instead, the percentage is always close to 100%. Also, in cases 2 and 6, PoD_{avg} improves from about 70% to 90%.

Table 4 - Results

Id. Sensor	Case 1	Case 2	Case 3	Case 4	Case 5	Case 6	Case 7	Case 8	Case 9
1	3.19	100	100	100	100	100	100	100	100
2	3.19	100	100	100	100	100	100	100	100
3	0	100	100	100	100	100	100	100	100
4	7.45	100	100	100	100	100	100	100	100
5	1.07	100	100	100	100	100	100	100	100
6	2.13	100	100	100	100	18.59	100	100	100
7	1.06	100	100	100	100	100	100	36.52	5.33
8	4.26	90.17	100	100	100	100	100	100	100
9	3.19	100	100	100	100	100	100	100	100
10	0	100	100	100	100	81.69	99.93	100	100
11	0	100	100	100	10.47	100	100	100	100
12	4.26	100	100	100	100	100	100	100	100
PoD _{avg}	2.48	99.18	100	100	92.54	91.64	99.49	94.7	92.11

By applying the Frequency Domain Decomposition (FDD) technique to the experimental data for each damaged case, in reference to the first two vibration modes of the structure, a comparison between the results can be performed. In Table 5, for each damage scenario, the modal frequencies are shown. The results show that, except in cases 2 and 3, structural damage can be identified through the analysis of modal frequencies. While in cases 2 and 3, the damage identification is difficult since a threshold is not uniquely established.

Therefore, the methodology allows to distinguish with less uncertainty the different structural conditions thanks to the use of the VAE and the OC-SVM.

Table 5 – FDD results

Mode	Frequency (Hz)								
	Case 1	Case 2	Case 3	Case 4	Case 5	Case 6	Case 7	Case 8	Case 9
1	7.47	7.47	7.32	6.64	5.18	5.96	2.63	2.54	2.58
2	7.76	-	-	7.62		7.81	3.62	3.28	3.37

To test the reliability of the method against noise-induced disturbances, a series of experiments under various noise scenarios were simulated. A Gaussian noise with different sigma levels was introduced to simulate the noise conditions. Since the magnitude of the input signal was of the order of 10^{-3} , the sigma level was gradually increased until this threshold was reached. Figure 14 and Figure 15 show the effect of increasing the noise factor on the data in two different scenarios, namely, when noise is already present during the training phase (fig. 14) and when noise emerges over time after the training phase is completed (fig. 15). The presence of noise alters the performance of the proposed method only when its level reaches a magnitude comparable to that of the signal data (i.e., 10^{-3}), thus revealing that the method is resistant to the level of noise both when it is already present during the training phase and when it emerges over time. The traditional technique based on dynamic identification is not effective when the data is affected by noise. Figure 16, Figure 17 and Figure 18 show the representation of the first singular value of the decomposed spectrum for case 1, 4 and 9 respectively. The curve for the case without noise (i.e., when the data are filtered) is presented in black. The other colors represent the curves obtained with the raw data by adding noise. The representation of the first singular value of the power spectrum is strongly distorted by noise when sigma is between 10^{-6} and 10^{-3} . In fact, resonance peaks- from which the structure's self-frequency of vibration can be read-are not detected. In contrast, when the noise is reduced, the frequencies are uniquely determined. Therefore, the frequency variation used as a damage-sensitive feature- and consequently the traditional method- are ineffective in the presence of noise because the latter affects the detection of the frequencies themselves, i.e., does not allow their identification.

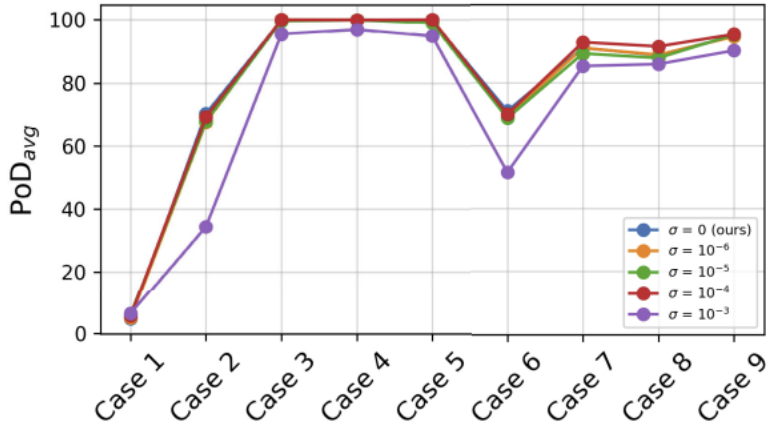


Figure 14 – Influence of noise when it is present during the training stage

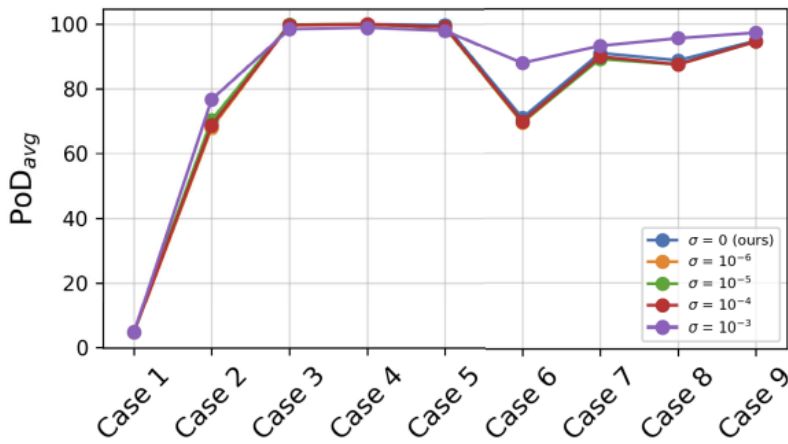


Figure 15 – Influence of noise when it emerges after the training stage

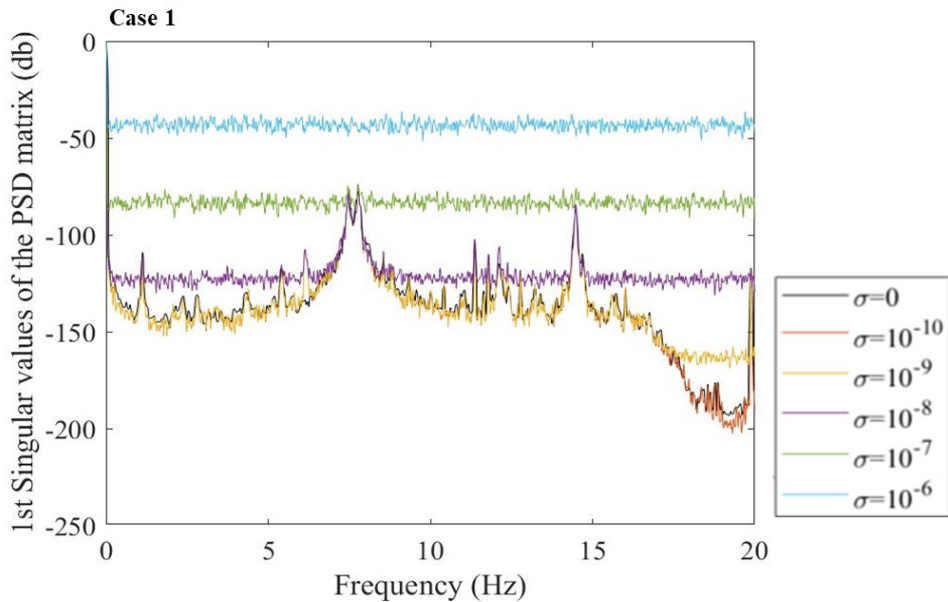


Figure 16 – Influence of noise on the representation of the first singular value of decomposed PSD for healthy case

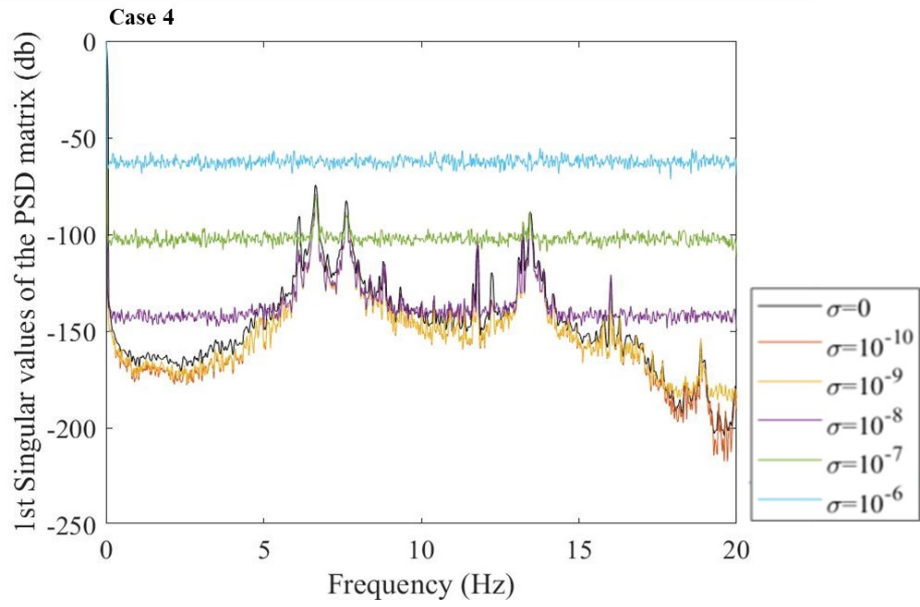


Figure 17 – Influence of noise on the representation of the first singular value of decomposed PSD for case 4 (damaged)

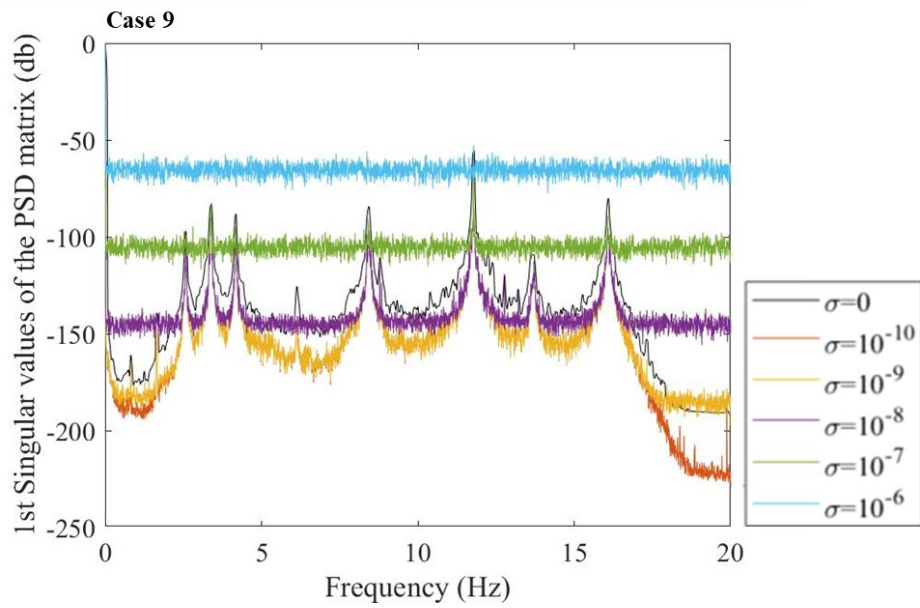


Figure 18 – Influence of noise on the representation of the first singular value of decomposed PSD for case 9 (damaged)

2.6.2. Prestressed concrete joists

The case study is a prestressed concrete joist tested in the laboratory of the Department of Structures for Engineering and Architecture, University of Naples Federico II. Figure 19 shows the geometric properties of the case study, while Table 6 summarizes its mechanical properties.

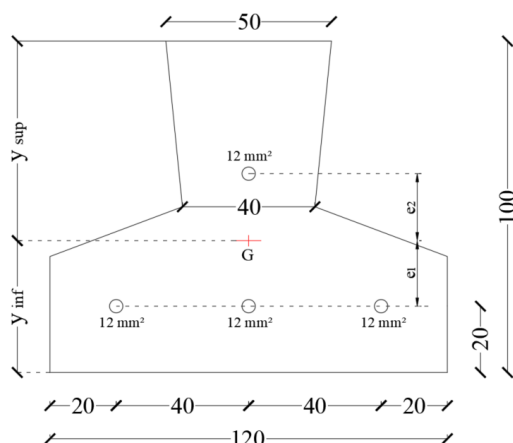


Figure 19 – Geometric properties

Table 6 - Mechanical properties

f_{ck}	Mpa	45.65
f_{cd}	Mpa	25.87
E_c	Mpa	36416.1
A_s	mm ²	12
E_s	Mpa	201000
δ_1	mm	20
δ_2	mm	60
f_{ptk}	Mpa	1860
f_{pk}	Mpa	1496
$f_{p(1)k}$	Mpa	1670
e_1	mm	15.66
e_2	mm	24.34

Considering the length of the joists to be 2.40 m and the distance between supports to be 1.70 m (see Figure 20), the values of the external forces to be applied to overcome the moment of first cracking, resistant moment and resistant shear were defined. Table 7, therefore, shows the moment and shear values tapped which result in: (i) the activation of the cracking phenomenon and (ii) the tapping of the collapse condition.

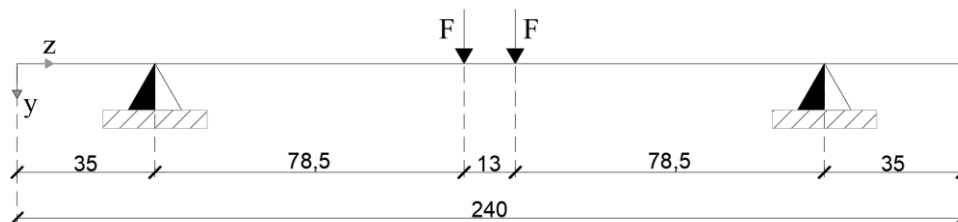


Figure 20 – Static schemes

Table 7 - Moment and shear limit values

Exceeding of	M_{cr}	M_{rd}	V_{rd}
	kNm	kNm	kN
Single force	2.64	3.97	4.89
Total load	5.28	7.94	9.78

The dynamic characterization of the joist was carried out by the simplified formulation considering the supported beam scheme with uniformly distributed mass. The vibration period associated with the n-th mode can be derived from eq. 25 where I denotes the inertia of the section, E the elastic modulus of the material, L the length of the beam contained between the two supports, and μ the linear density.

$$T_n = \left(\frac{L}{n}\right)^2 \frac{2}{\pi} \sqrt{\frac{\mu}{EI}}$$

The frequencies of the first three vibration modes in the y direction are shown in Table 8.

Table 8 - Frequency

n	L	EI	μ	T	f
-	m	ton·m ³ /s ²	ton/m	s	Hz
1	1.70	220.54	0.02003	0.017	57.03
2	1.70	220.54	0.02003	0.004	228.13
3	1.70	220.54	0.02003	0.002	513.29

The joist was subjected to static tests for the application of the artificial intelligence-based method and dynamic tests for the identification of modal properties.

Dynamic test

For this purpose, STIM and EPSON sensors were installed on the joist to acquire acceleration time histories with a sampling frequency of 250 Hz. The tests were conducted in the case of unloaded and loaded joist. For the second case, two additional masses of 26 kg are placed at 65 cm from the ends of the joist. In addition, the tests were performed in both the healthy condition of the joist and the damaged condition. The above-mentioned sensors were arranged considering two types of configurations:

(i) Paired configuration, in which 3 pairs of STIM sensors were placed in two sections located at 114 cm and 160 cm from the left end of the joist. In each section, one STIM sensor was placed on the front side face, one on the back side face and one on the top side face as shown in Figure 21. The EPSON sensor was placed on the upper face of the joist at 110 cm from the left end.

(ii) Longitudinal configuration, in which 4 STIM sensors and the EPSON sensor were placed on the front side face of the joist and two STIM sensors were placed on the back side face. In Figure 22 the sensor placement is shown.

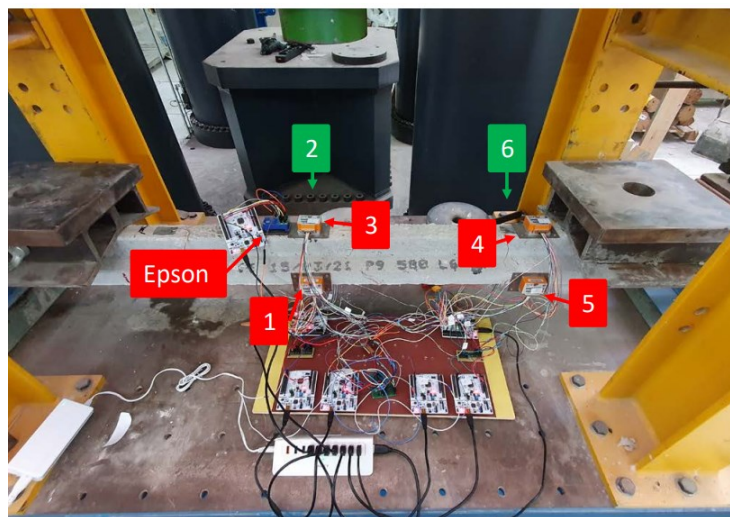


Figure 21 – Paired configuration

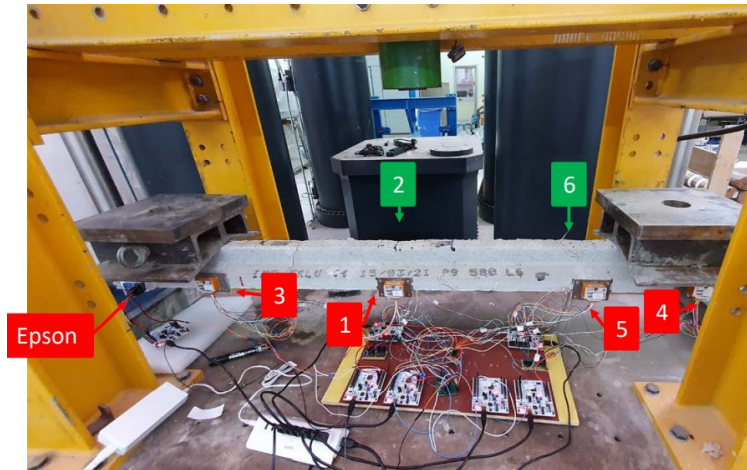


Figure 22 – Longitudinal configuration

For the unloaded joist, a preliminary analysis of the records showed that the STIM-2 sensor was not working properly in the unloaded joist case and the STIM-2 and STIM-5 sensors in the loaded joist case. For this reason, these records – whose duration is less than 30 minutes - were not used in the anomaly detection procedures. Vice versa, for the loaded joist, all sensors were considered.

In the case of the unloaded joist, the damage consists of; (i) a cut in the three strands of the lower register in the middle section of the joist, and (ii) a cut in the middle-strands of the lower register in the section near the sensor 1. The tests were carried out with acceleration recorded with a sampling frequency of 250 Hz.

Since the Nyquist frequency is 125 Hz, it was not possible to derive the frequency values related to vibration modes greater than the first in y; these values, in fact, are greater than 300Hz from numerical model. Table 9 shows the obtained modal frequency.

The simulated damage determines an average frequency change of 12%. In fact, the variation is more evident from configuration 1 (about 17%) than from configuration 2 (about 7%).

Table 9 – Experimental frequency – unloaded joist

Damage	Conf. 1	Conf. 2
	f - Hz	f - Hz
Presence	58.83	51.03
Absence	48.82	47.24

In the case of loaded joist, only the longitudinal configuration case was analyzed, and three damage scenarios were considered. Specifically, it always involves the shear of one or more strands and there are (i) case 1 - shear affects one strand in the middle section; (ii) case 2 - shear affects two strands in the middle section; (iii) case 3 - shear affects the three strands of the lower register in the middle section. Once again, tests were performed with acceleration records obtained with a 250 Hz sampling rate. In this case, the presence of additional mass determines a reduction of the structure's eigenfrequencies. So, it was possible to identify the eigenfrequencies up to the third vibration mode. The results of the dynamic identification process are summarized in Table 10. Let's note that the damage in all three scenarios cannot be identified by the classical identification technique because it does not result in a significant change in stiffness. In fact, the maximum frequency change obtained is about 1%.

Table 10 - Experimental frequency – loaded joist.

Case	Mode 1	Mode 2	Mode 3
	f [Hz]	f [Hz]	f [Hz]
healthy	34.85	49.22	65.98
1 cut	34.96	49.07	66.18
2 cuts	35.03	48.94	65.61
3 cuts	35.04	49.37	65.76

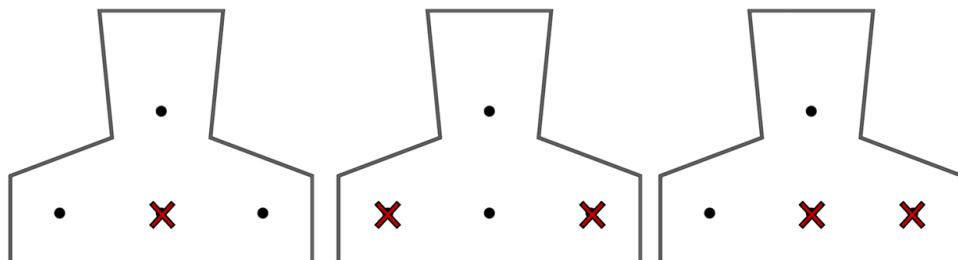
Static test

A static test was designed considering a flexural-type collapse because the load associated to the bending failure is lower than shear failure. The experimental test was conducted on four scenarios: (i) two health conditions (L4.1 and L4.5) and (ii) three damage conditions (L4.2, L4.3 and L4.4). During the static test, a load was generated using a manual hydraulic cylinder with a piston having a minimum stroke of 0.3 cm and a maximum stroke of 5.7 cm. A load cell is used to read the applied load. Finally, this load is applied on the joist as two forces 13 cm apart.



Figure 23 – Static test

Figure 24 shows the location of the damage on the joist: (a) for L4.2, the middle strand is cut in the middle section; (b) for L4.3, the left and middle strands are cut in the middle section; (c) for L4.4, the left and right strands are cut in the middle section.



(a) Damaged condition L4.2 (b) Damaged condition L4.3 (c) Damaged condition L4.4

Figure 24 – Damaged cases: (a) L4.2, (b) L4.3 e (c) L4.4

15 sensors are placed on the joist: six horizontal LVDTs and six strain gauges for strain analysis and three vertical LVDTs for vertical displacement. Figure 25 shows the location of the sensors. The joist has three pairs of LVDTs with a stroke of 20 mm for longitudinal displacements are placed along its side faces (green triangle in the figure),

three LVDTs for vertical displacements are placed along the top base (blue circle in the figure), and three pairs of strain gauges are placed above and below the joist, respectively (red rectangle in the figure).

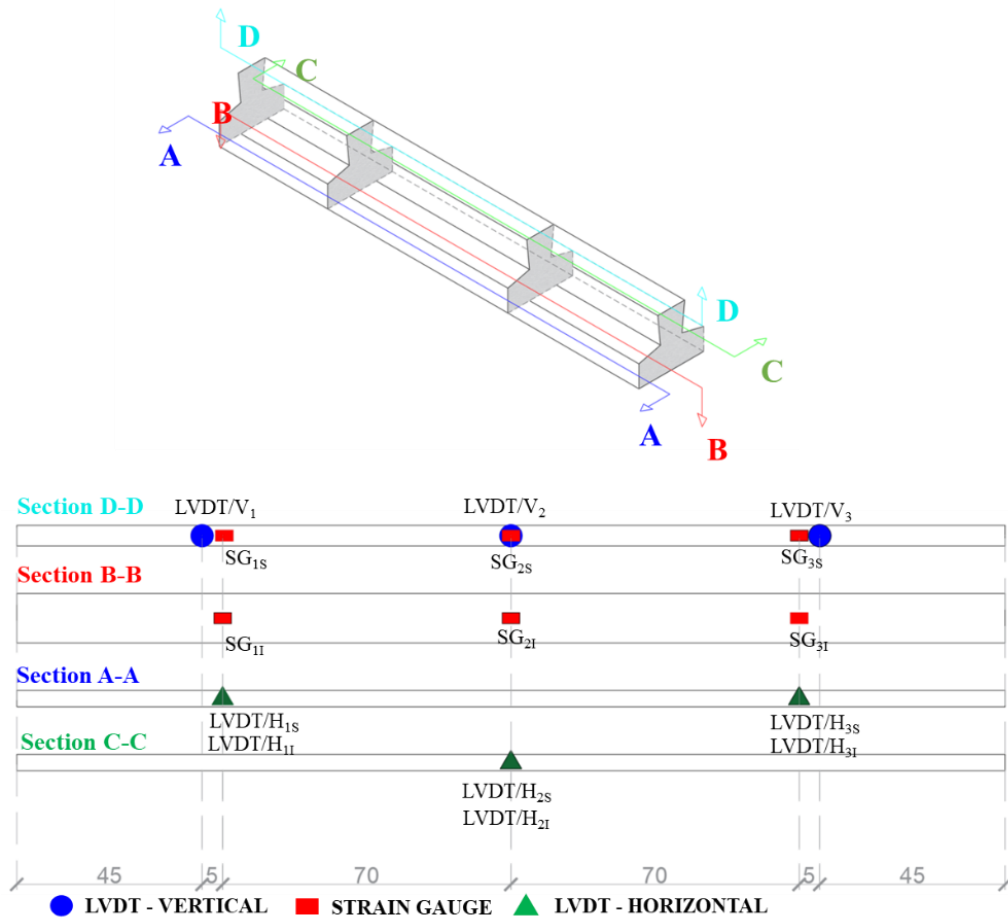


Figure 25 – Sensors' location

Figure 26 shows the force-displacement curve for each analyzed case, where the force is the total applied load while the displacement is the vertical displacement read at the middle section of the joist. In Figure 26, the blue point represents the end of the elastic field (i.e., when the first crack is formed), while the red point represents collapse. Let's note that the joist L4.2 has similar behavior to the L4.1 because the limited damage does not cause significant changes in stiffness and strength. In contrast, for L4.3 and L4.4, the variation is more significant.

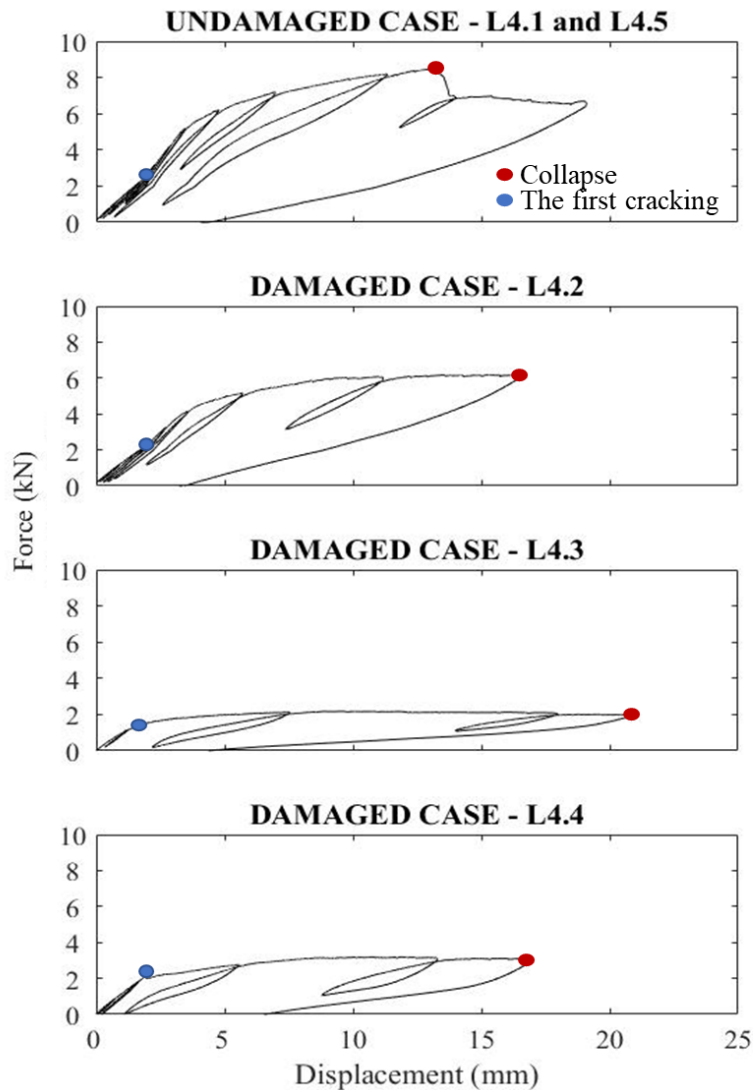


Figure 26 – Force displacement curves

The first phase consists of numerical simulation of the joists' behavior. A linear static analysis was performed to derive the force-displacement curves of the joist. For numerical modeling in OpenSees (Open System for Earthquake Engineering Simulation, <http://opensees.berkeley.edu>), the joists were discretized into 12 sub-elements for the sound case (L4.1) and 24 sub-elements for the damaged cases, each characterized by an initial prestress value, cross-section, and constitutive bond. Specifically, the constitutive bonds of the materials used are (i) a bilinear uniaxial bond with hardening was adopted for steel and (ii) a uniaxial bond with tensile strength was adopted for concrete.

Prestressing of cables in OpenSees was simulated by applying a diffuse pretensioning model, in which the force is applied to each sub-element of the joist. Specifically, for the healthy case, the applied force is 62.5kN and the corresponding moment is 0.3kNm. In the presence of damage, prestress is reduced proportionally to the area of the damaged strands; specifically, the force and moment are (i) 46.9kN and 0.12kNm for L4.2; (ii) 31.25kN and 0.13kNm for L4.3 and L4.4.

Figure 27 shows the comparison between the experimental force-displacement curve represented in red (for cases L4.1, L4.2, L4.3 and L4.4) or blue (for L4.5) and the same curve obtained from the numerical simulation in black for each case. For joist L4.1 and L4.5 there is a perfect correspondence between the numerical analysis and the

experimental behavior in the elastic field – in fact the two curves tend to overlap. For case L4.2, the two curves tend to diverge in the last two cycles where the force value is greater than 1 kN. Finally, for cases L4.3 and L4.4 there is no correspondence between the numerical and experimental behavior from the very first cycles. So, the results show a correct modeling of the healthy case and in the case with damage applied to the central strand (joist 4.2). In contrast, the modeling is inadequate for the other two cases of damage.

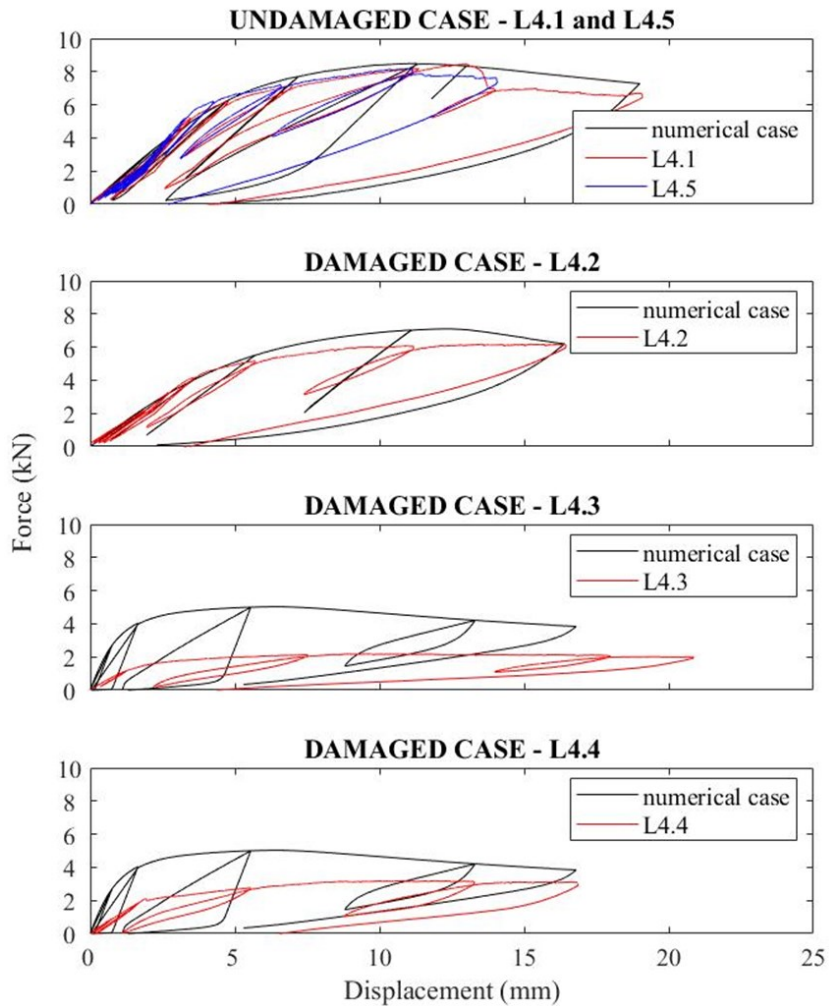


Figure 27 – Comparison between experimental curve (red or blue) and numerical one (black)

Analysis of the recorded data shows that not all sensors are operational during the test. The malfunction of some sensors can be attributed to: (i) inadequate installation of the instrument or (ii) loss of contact with the element during the test due to progressive degradation of the element. Specifically, the application of the methodology was carried out considering only the sensors operating in each test configuration. Information on the working sensors is summarized in Table 11.

Table 11 – Operational sensors

	LVDI/H _{1S}	LVDI/H _{2S}	LVDI/H _{3S}	LVDI/H _{1I}	LVDI/H _{2I}	LVDI/H _{3I}	LVDI/V ₁	LVDI/V ₂	LVDI/V ₃	SG _{1S}	SG _{2S}	SG _{3S}	SG _{1I}	SG _{2I}	SG _{3I}
L4.1	Operational	Operational	Operational	Operational	Operational	Operational	Operational	Operational	Operational	Operational	Damaged	Operational	Operational	Operational	Operational
L4.5	Operational	Damaged	Operational	Operational	Operational	Operational	Operational	Operational	Operational	Operational	Operational	Operational	Operational	Damaged	Operational
L4.2	Operational	Operational	Operational	Operational	Operational	Operational	Operational	Operational	Operational	Operational	Operational	Operational	Operational	Operational	Operational
L4.3	Operational	Operational	Operational	Operational	Damaged	Operational	Operational	Operational	Operational	Operational	Operational	Operational	Operational	Damaged	Operational
L4.4	Operational	Damaged	Operational	Operational	Damaged	Operational	Operational	Operational	Operational	Operational	Operational	Operational	Operational	Damaged	Operational

	Operational sensors
	Not operational sensors
	Sensors damaged during the test

The static measurements were analyzed considering only a range of load between 0 and 2 kN, i.e., when the joist is in the elastic field. The limitation on the use of the data arises from the need to identify a method of structural damage identification that performs well when the minimum structural safety standards are still guaranteed.

The experimental tests were conducted using a sampling rate of 5Hz. Therefore, the signals can be divided into frames with a length s equal to 1 sec – i.e., with 5 consecutive values of the signal itself. The data were reshuffled and normalized between 0 and 1.

Figure 28 and Figure 29 show an example of a graphical representation of the signal reconstructed by a VAE in an undamaged (i.e., L4.5) and damaged (i.e., L4.4) case. The input of the VAE consists of vectorization of all selected sensor signals, i.e., concatenation of their values for each second. Therefore, the reconstructed output does not correspond to any initial signal. Note that in the presence of damage, the reconstructed signal is very different from the original signal. In contrast, in the absence of damage, the error is reduced. Therefore, error metrics are good features to detect the health of the structure.

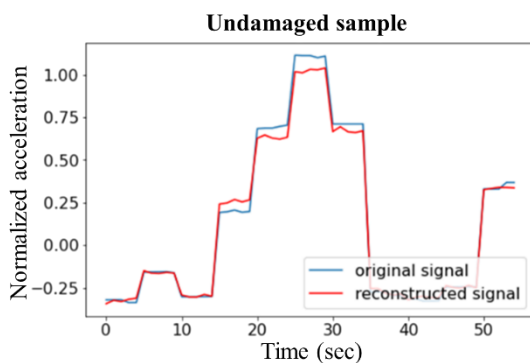


Figure 28 – Comparison between output of VAE and target, healthy case

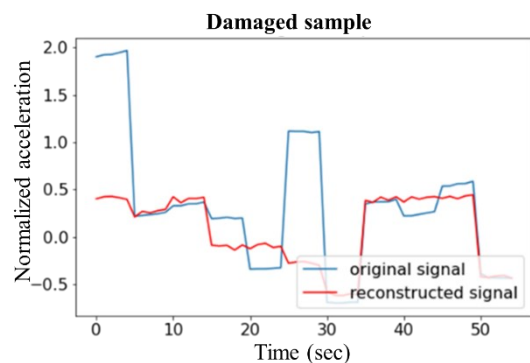


Figure 29 – Comparison between output of VAE and target, damaged case

Figure 30 shows a graphical representation of an OC-SVM trained on undamaged training data (Case L4.1) and tested on damaged test data (L4.2, L4.3 and L4.4). In the case L4.3 and L4.4, most of the points in the test set are not internal to the domain. Conversely, in case L4.2, a good percentage of points are internal to the domain.

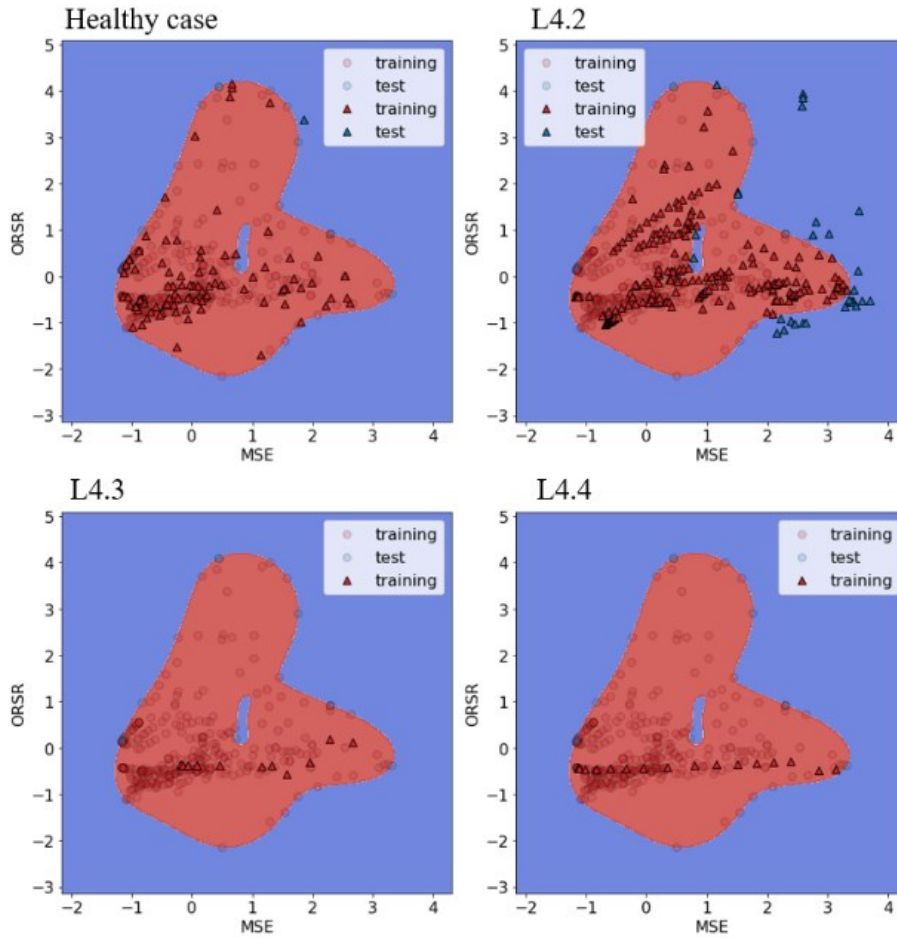


Figure 30 – OC – SVM results

The POD_{avg} are summarized in Table 12. Thus, the healthy cases (L4.1 and L4.5) are classified as healthy condition because the POD_{avg} is less than 5%. Similarly, L4.3 and L4.4 are classified as damaged, and they have a POD_{avg} close to 100%. L4.2 is misclassified because only 40% of the points are outside the domain.

Table 12. Thus, the healthy cases (L4.1 and L4.5) are classified as healthy condition because the POD_{avg} is less than 5%. Similarly, L4.3 and L4.4 are classified as damaged, and they have a POD_{avg} close to 100%. L4.2 is misclassified because only 40% of the points are outside the domain.

Table 12 - POD_{avg} for all cases

	POD_{avg} [%]
Healthy state	4.08
L4.2	41.36
L4.3	96.95
L4.4	91.09

2.7. Conclusions

This chapter introduced the main methodologies for structural monitoring in order to detect anomalies in the structural behavior.

On the one hand, the dynamic identification process to detect the modal properties of structures is described. Modal properties - such as the frequency - can be adopted as indicators of the damage's presence. In fact, structural damage can result in a change in stiffness and/or mass and, therefore, cause a change in the dynamic behavior of the structure.

On the other hand, a methodology based on artificial intelligence i.e., through artificial neural networks is described. So, a framework to perform the damage detection with an unsupervised approach in a SHM system based on a VAE and an OC-SVM was proposed in order to minimize human interactions during the data classification process.

The results of the dynamic identification process can be analyzed through a data-driven approach i.e., without a numerical model for structural damage detection or a model-based approach. They are usually used for updating the numerical model of the structure (model-based approach), which will be discussed in Chapter 3. Conversely, the results obtained through artificial neural networks are analyzed through a data-driven approach i.e., damage detection is carried out based on data variations without the adoption of the numerical model.

The unsupervised approach makes it possible not to use simple and/or sophisticated numerical models. This is an advantage because for complex structures it would be necessary to have preliminary dynamic identification tests to verify the congruence between model and actual behavior. This leads to a reduction in monitoring costs and the time required to assess the health of the structure.

The proposed method makes it possible to automate the entire damage identification process, taking less time than a traditional SHM technique because it works directly on the raw data. In addition, the OC-SVM allows to automate the acceleration classification process, thus avoiding any user-defined decision rules. The probabilistic VAE allows to model heterogeneous data with different distributions. So, in the case of damaged data, the probabilistic encoder models different data distributions than in the healthy case and, therefore, the errors committed by the network increase. Therefore, the error metrics used as damage-sensitive features are valid for the classification of healthy conditions of structures.

The methodology was tested on two different structural types: (i) a scaled steel framed structure and (ii) prestressed reinforced concrete joists. In both cases, the joint use of VAE and OC-SVM allows the identification of structural damage even when it is localized, unlike the usual anomaly detection techniques based on dynamic identification. In fact, in the case of the steel frame, the frequency change is significant only from the 5-th damage scenario. So, from the case 2 to the case 4, it is not possible to detect the damages. Conversely, the artificial intelligence algorithm allows the detection of damage in all examined scenarios. Similarly, this also applies to the prestressed concrete joist. The algorithm was tested with dynamic data i.e., accelerations in the case of the steel structure and with static data in the case of the joist. We note that the algorithm is effective with both types of measurements. However, the best-performing results are obtained with acceleration data because the greater amount of data with which the network is trained in the case of dynamic measurements allows for increased network performance.

Finally, although the framework does not offer the ability to locate damage based on the score of individual sensors, the methodology - tested on real (no numerical) data - is a valid anomaly detection tool adaptable to all existing structural types.

From the state-of-the-art described in the previous chapter, let's note that although artificial intelligence techniques are widely analyzed in the field of structural monitoring, their study is of recent interest i.e., there are many methodologies still under development. This implies that most of the existing applications in the literature concern existing bridges and/or scale reproductions subjected to laboratory testing. Therefore, these applications allow the artificial neural network to be calibrated by assuming the real structure in a healthy condition. However, damage conditions are simulated by numerical modeling or laboratory testing. The applications described therefore fit into this landscape and represent a starting point for future applications on complex real structures.

In the future, the proposed methodology will be applied to complex real structures such as bridges and/or real edifice (i.e., with structural and nonstructural permanent loads and accidental ones). This will provide an opportunity to investigate the goodness-of-fit of the results of the procedure and/or possibly implement a deep neural network that might perform better with complex structures. Since it is important not only to detect the presence of damage, but more importantly to localize it, it would be interesting to extend the procedure to damage localization. Regarding the estimation of the extent of damage or its prediction, aware that a data-driven approach is not sufficient, model type techniques based on traditional approaches will be developed.

Updating of FE models

In the previous chapter, the case studies have shown that artificial intelligence-based monitoring techniques allow to reduce the computational time of large amounts of data, to overcome the manual decision-making phase for detecting the health status of structures, and to operate with raw data. Moreover, for the two specific applications, the artificial neural network-based technique enabled the identification of structural damage with less uncertainty than traditional techniques based on dynamic identification. However, this result could be reversed by changing the type of damage-sensitive feature or by a different location of sensors on the structure. In fact, the accuracy of the dynamic identification process' results depends on the spatial distribution of sensors on the structure as well as the number of sensors and their resolution. In particular, the accuracy of the dynamic identification process can be improved if the executive design of structural monitoring is carried out through the adoption of optimal sensor placement (OSP) techniques. The main OSP techniques allow to derive an efficiency ranking of sensor locations for identifying the vibration modes of the structure. However, these techniques do not define a criterion to select the optimal number of sensors. For this reason, a criterion for selecting the optimal number of sensors is defined from the OSP technique called Effective Independence (EFI) (Testa et al., 2022 b).

Moreover, the data-driven approach followed in the previous chapter - whether using innovative techniques or traditional approaches - is severely limited to the detection and, at most, localization of structural damage. For damage quantification and prediction, on the other hand, it is necessary to use a model-based approach. This approach involves adopting numerical models of the structure that are well representative of the actual behavior of the structure. Generally, simplified structural models are adopted for existing bridges, despite the importance and complexity of the structural types. The model updating - following dynamic identification tests - allows to use (i) on the one hand, an accurate model with which to carry out structural safety checks and (ii) on the other hand, a useful tool for planning operation and maintenance plans following the detection of anomalies. Related to the FE model updating process, a real application will be shown by which it emerges the need: (i) to critically analyze the update steps in order to identify possible anomalies and (ii) to use not only dynamic but also static test results in the update process.

3.1. Optimal Sensor Placement

The optimization of the accelerometer network is a necessary step in the design of a dynamic identification test because the accuracy of the results may depend on several factors, including the sensitivity of the instrumentation to the surrounding noise, the sampling rate, the recording duration as well as the number and spatial distribution of the sensors on the structure. Referred to the sensors' number and position, that limiting the number of instruments allows reducing the computational burden that depends on the volume of data to be processed and the cost of the instrumentation system (Chang and Pakzad, 2014), but it could negatively affect the goodness of the results expected from the identification process.

Some authors proposed methods for optimal sensor placement (*OPS*) based on the estimation of modal displacements derived by numerical model of the structure, e.g., finite element (*FE*) model. Four *OPS* methods are discussed here. These are: the effective independence method (Kammer, 1991; Rao et al., 2014; Liu et al., 2018), the displacement index method (Kammer, 1991; Rao et al., 2014; Liu et al., 2018; Moussas, V. C., & Pnevmatikos, 2019), the driving point residue method (Papadopoulos and Garcia, 1998), and the eigenvalue vector product (Michele Meo, 2004). Each model aims to compute an efficiency index for each sensor position and, consequently, to define a priority ranking list of all the analyzed sensor positions.

Although these methods make it possible to define a ranking of efficiency from a predetermined set of measurement points, there is no defined criterion for selecting the number of sensors appropriately deployed on the structure.

For the application of effective independence (EFI) method, the Fisher matrix, FIM, is defined as a function of the product between the matrix of modal shapes $[\chi]$ of monitored points (i.e., those in which sensors are located, also identified as nodes hereafter) and its transpose. The generic element of $[\chi]$, φ_{ki} , indicates the displacement of *i*-th sensor due to the *k*-th mode. If *S* indicates the number of all possible position of sensors and φ is the modal displacement - read through the FE model - of each node in which sensors are located and for each interested mode, the generic element of the FIM matrix - ψ_{ij} referred to the *i*-th position of sensor and the generic mode *j* - is defined as (eq.26):

$$\psi_{ij} = \sum_{k=1}^S \varphi_{ki} \cdot \varphi_{kj} \quad 26$$

So, the FIM matrix can be represented through the eq. 27.

$$FIM = [\chi]^T [\chi] = \begin{bmatrix} \varphi_{11} & \cdots & \varphi_{1M} \\ \vdots & \ddots & \vdots \\ \varphi_{M1} & \cdots & \varphi_{MM} \end{bmatrix} \quad 27$$

The number of rows of $[\chi]$ is equal to number of sensors, *S*, and the number of columns is the number of considered modes, *M*. Thus, the FIM matrix has *M* x *M* dimensions. The efficiency index is the EFI parameter, and, for the *i*-th sensor, it is calculated via eq. 28.

$$EFI_i = \{\varphi_i\} FIM^{-1} \{\varphi_i\}^T \quad 28$$

where $\{\varphi_i\}$ is a (1 x M) vector collecting the displacements of the i node for M considered modes. The higher is EFI_i , the more important is the sensor with respect to the dynamic identification of the structure.

For the application of the Displacement Index (DI) method, the index is calculated for each node and mode, which is a function of the product between the mass of node M_i and its modal displacement $\{\varphi_i\}$. For each node I and mode j, the displacement index DI_{ij} is calculated via eq. 29.

$$DI_{ij} = \sqrt{\sum_{k=x,y,z} (M_i * \varphi_{ij}^k)^2} \quad 29$$

Where k indicates the direction of the displacement (e.g., x, y, z).

the importance coefficient is obtained by summing for each node the contributions associated with each mode (see eq. 30).

$$DI_i = \sum_{j=1}^M DI_{ij} \quad 30$$

The driving point residue (DPR) method assigns to each node the efficiency index DPR calculated via eq. 31

$$DPR_i = \sum_{j=1}^M \frac{\varphi_{ij}}{\omega_j} \quad 31$$

Where φ_{ij} is the modal displacement of the node i for each mode j with angular frequency ω_j . Again, the most effective nodes are those having higher DPR.

Finally, the eigenvalue vector product (EVP) method is based on the evaluation of the efficiency index EVP index via eq. 32.

$$EVP_i = \prod_{j=1}^M \varphi_{ij} \quad 32$$

Where φ_{ij} is the modal displacement of the node i for each mode j. The optimal positions are those having higher EVP.

Although the techniques can be implemented by considering each node of the FE model that is a potential position for the sensors, defining a preliminary configuration with less sensors based on engineering judgment is usual.

Pachóna et al. (Pachón et al., 2020) proposed to define the optimal position of the sensors according to the results obtained by a preliminary application of the above-mentioned EFI technique and those obtained by an iterative process of dynamic identification on the FE model. In this process the accelerations simulated with dynamic linear analysis are used to apply dynamic identification techniques and to evaluate the frequency errors with respect to the known vibration frequencies of the numerical model by varying the sensors' configuration.

The introduction of the selection criterion on the basis of frequency error makes it possible to reduce the number of sensors needed to obtain sufficient results in terms of both frequencies and modal shapes.

3.2. Selection Criteria

Here, a selection criterion for defining the sensors' optimal number appropriately placed on the structure is described starting from the efficiency ranking obtained by the previously defined OSP methods. In fact, these methods allow to define a ranking of sensor efficiency, but a criterion for selecting the optimal number of sensors is not established.

The method consists of simulating the dynamic identification technique by varying the configuration of sensors consistent with the ranking of the OSP method. The optimal sensors' configuration consists of the first sensors of the ranking that: (i) on the one hand reduces the number of sensors, and (ii) on the other hand minimizes the errors between the identification results and the numerical ones (i.e., from the modal analysis of the FE model).

Specifically, if S is the total number of sensors in the initial configuration, the OSP methods return a ranking of S sensors sorted by decreasing efficiency coefficient. Then, starting from the configuration consisting of the first two sensors in the ranking, several configurations can be analyzed, each with one more sensor than the previous one added in accordance with the above ranking.

Furthermore, by scaling the coefficients with respect to the maximum value of the ranking, each configuration is associated with the cumulative efficiency coefficient (i.e., the sum of the coefficients associated with each position that constitutes the configuration).

For each configuration, it is possible to simulate the FDD technique using the accelerations obtained from the linear dynamic analysis performed with FE model by exciting the structure using Gaussian white noise. This allows to simulate the dynamic identification process i.e., to derive the eigenfrequencies of vibration of the structure. Finally, by comparing the FDD results with those of the FE model modal analysis, it is possible to estimate the cumulative frequency error, E (eq. 33) committed with each sensor configuration in relation to the j identified modes:

$$E = \sum_j |freq_{ID_j} - freq_{NUM_j}| \quad 33$$

In order to describe the methodology, a numerical case study is used (Testa et al., 2021). Then OSP methods are applied to a concrete arch bridge. Figure 31 shows the geometry of the thin-vaulted arch bridge modeled in Sap2000 (CSI, 2019) with beam elements and assuming hinge constraint at the base. The modal analysis of the structure was extended to vibration modes sufficient to activate at least 90 percent of the modal masses in the three directions (i.e., x, y, z). Table 13 shows the frequencies and modal masses of the most significant vibration modes (i.e., associated with nonnegligible modal mass) that should be identified by operational modal analysis.

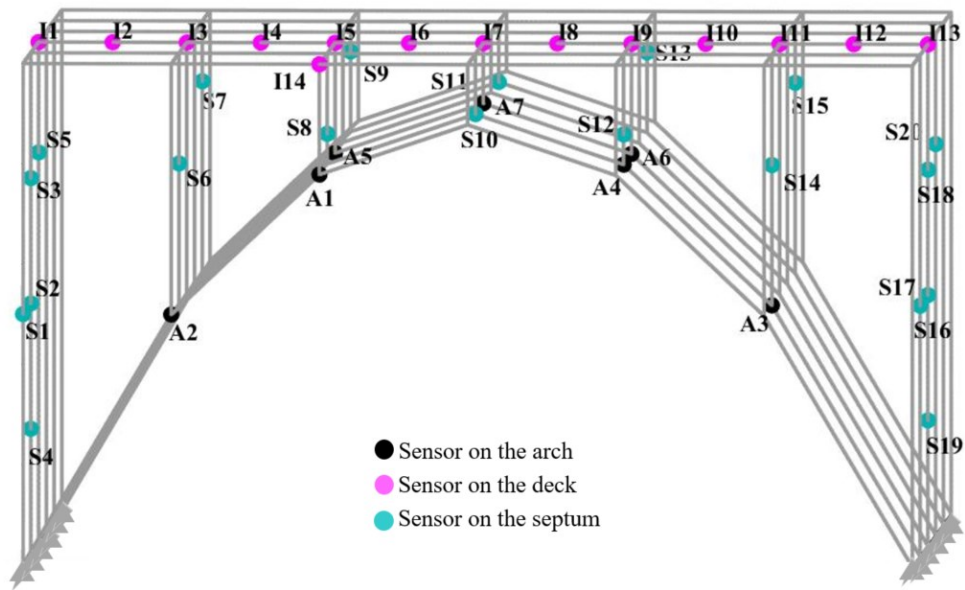


Figure 31 – Initial sensor configuration

Table 13– Analytical modal analysis

Freq. Hz	Mass [%]		
	X	Y	Z
2.03	70	0	0
2.67	0	62	0
3.13	3	0	0
4.44	0	14	0
4.81	12	0	0
7.16	0	9	0
8.4	0	0	22
8.64	1	0	0
8.84	0	0	50
9.98	0	6	0
10.36	1	0	0
12.01	0	0	1
16.52	0	1	0
16.8	0	0	1
20.17	11	0	0
23.56	0	1	0
24.36	0	3	0
25.1	0	0	17
sum	98	96	91

A limited number of sensors' positions have been defined on the FE model. The positions were not evenly distributed in the space, but they were identified starting from structure modal displacements: among the nodes with non-zero displacements, those necessary to identify also the local modes were favored. More specifically, one sensor at the end and in the middle of each span of the central beam and one on the external beam of the deck

was considered; moreover, two sensors for each internal septum and five sensors on the external septa were located. Finally, three sensors were placed on the central arch and two on the outermost arches. Figure 31 shows the final configuration of the 41 triaxial accelerometers (i.e., $41 \times 3=123$ uniaxial accelerometers), identified by a number and a letter (I for deck - magenta, S for vertical wall - green, and A for the arc - black).

The application of the OSP methods allows calculating the efficiency index (i.e., EFI_i in eq. 28, DPR_i in eq. 32, EVP_i in eq. 32, DI_i in eq. 30), named hereafter α_i , for each i -th sensor with i ranging from 1 to 41. For comparison reasons, these coefficients were divided by the maximum index obtained with each method. Figure 32, Figure 33 and Figure 34 show the efficiency of each sensor for the three directions x, y, and z with a color scale in which red and blue correspond to high and low efficiency, respectively. Note that the coefficients α_i of DI method are direction-independent whereas, for the other algorithms α_i are obtained for each direction as a function of the displacements in the corresponding direction.

For the first six modes obtained in the x direction from numerical model, the deck sensors for the EFI and EVP method present a factor $\alpha_i < 20\%$, while $\alpha_i \approx 40\%$ for DPR and $40\% < \alpha_i < 60\%$, for DI. On the other hand, for DI the sensors on the vertical walls have $\alpha_i < 20\%$, while the other methods provide $40\% < \alpha_i < 100\%$. For arc sensors only EFI and DI methods provide $\alpha_i > 20\%$.

For the first seven modes obtained in the y direction from numerical model, the deck sensors have coefficients larger than those computed in x direction, except for EVP. As expected, the sensors on the wall have low α_i values according to all the methods. Finally, the methods provide $40\% < \alpha_i < 60\%$ for the sensors located along the arches expect for the EVP method that provides $\alpha_i < 20\%$.

Similar results are provided by the first five modes in the z direction: for EFI and EVP, the sensors placement is ineffective excepting three positions on the arc, while for DPR and DI, α_i of sensors located along the deck and the arc is larger than those associated to sensors located along the vertical wall.

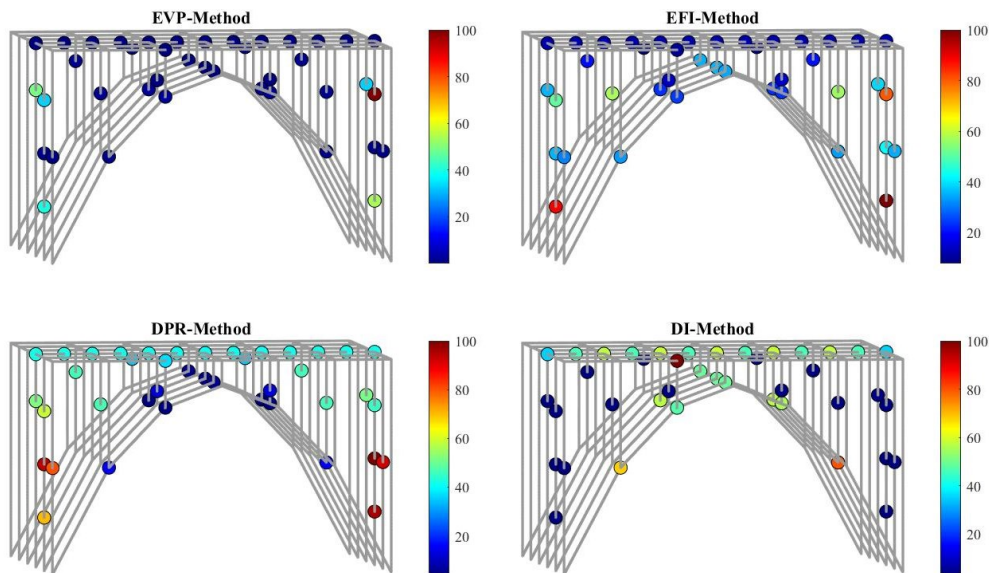


Figure 32 – Efficiency ranking, X direction

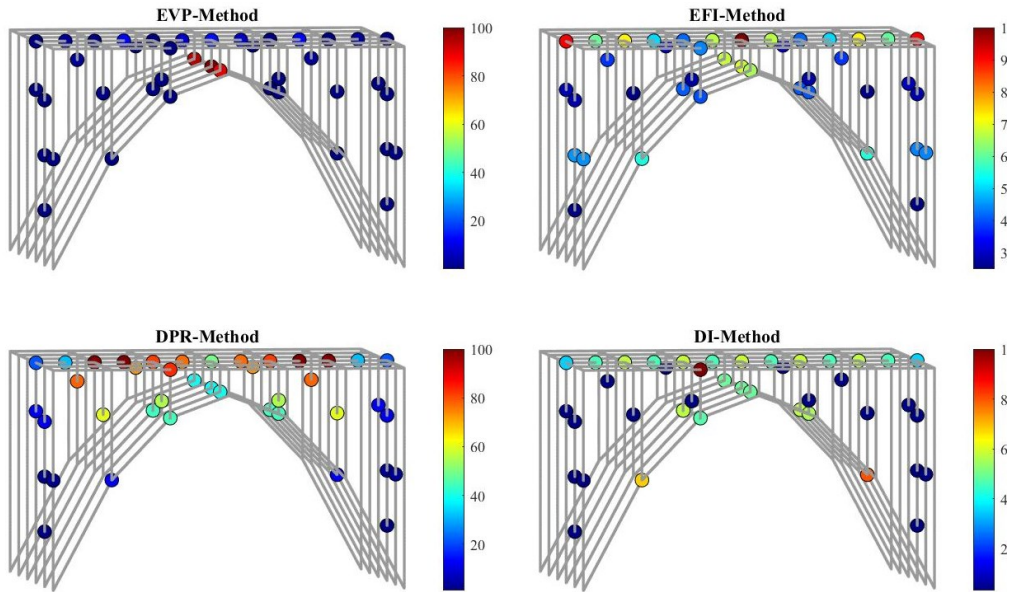


Figure 33 – Efficiency ranking, Y direction

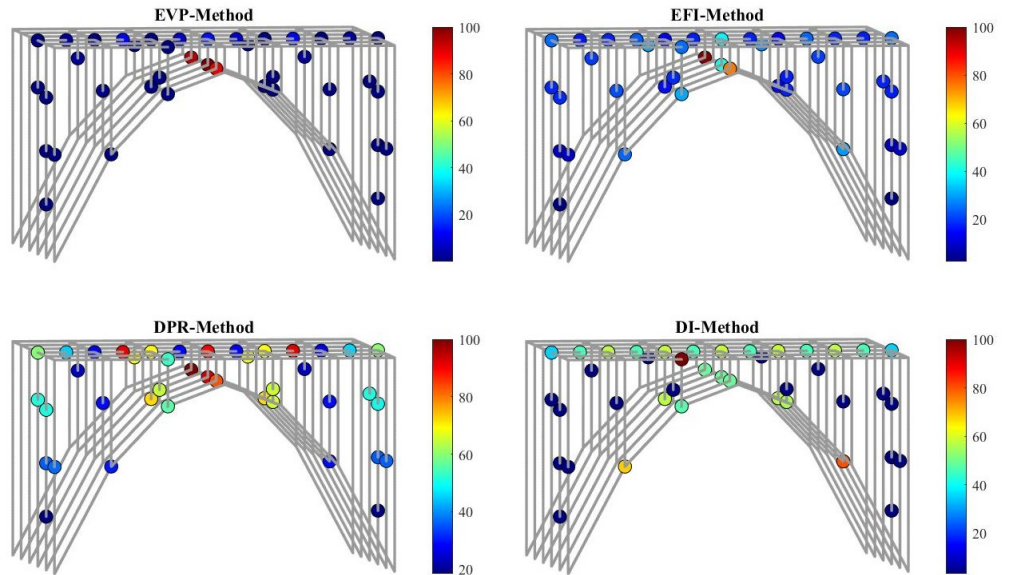


Figure 34 – Efficiency ranking, Z direction

According to results of each algorithm, the sensors are numbered by decreasing importance factor α_i . For each direction and OSP method, several configurations can be analyzed by an iterative process starting with the first two sensors of the ranking. At each step, a sensor is added in accordance with the above ranking, and then the coefficient $\vartheta_i = \sum_{i=1}^S \alpha_i$ is associated to the examined configuration.

The frequency domain decomposition (FDD) is applied to the accelerations simulated by the same FE model, by varying number and position of the sensors. In this case, the FDD technique is applied to accelerations in the three directions (x, y and z) simulated with a linear dynamic analysis exciting the structure with Gaussian noise for 150s with a sampling frequency of 100Hz. For each optimization method, following the corresponding ranking, the FDD technique is applied for each sensor configuration to assess the structural frequencies, ($freq_{ID}$). The results can be compared with those of

the numerical model, ($freq_{SAP}$), and therefore, it is possible to estimate the frequency error E (see eq. 33).

The results are shown in Figure 35, Figure 36 and Figure 37 for the three directions, using a color scale. The marker of each point indicates the number of modes that can be identified: cross for two modes, triangle for three, square for four, five-pointed star for five, six-pointed star for six and circle for seven.

Figure 35 shows that it is always possible to identify six modes of the structure in the direction x with the number of sensors varying according to the optimization method. With the target of six modes, the configuration obtained with the DI-method involves the use of all 41 sensors with an error $E \approx 3$ Hz, while the DPR method allows to reduce the number of sensors (34) but with a larger error ($E \approx 5.5$ Hz). The EFI method involves the use of 12 sensors with the same error provided by the DPR. Finally, the EVP technique requires only the first 7 sensors with the same identified modes, but with larger error, $E > 7$ Hz. To identify only five modes, the methods suggest using only two sensors with an error E between 5 and 5.5 Hz, except for the DI method that requires 7 sensors, with $E < 2.7$ Hz.

Figure 36 shows that in the direction y only the EVP configuration of sensors can identify seven modes of the structure, but the frequency errors are significant. The use of more sensors allows to identify six modes with lower errors (i.e., 8, 19 and 28 sensors with $E \approx 4.5$ Hz, $E \approx 3.5$ Hz and $E < 3.5$ Hz).

Figure 37 shows that, in direction z , at most four modes are identified. The DI method allows to identify four modes using two sensors, with similar errors with respect to those obtained using more sensors, according to the other three methods.

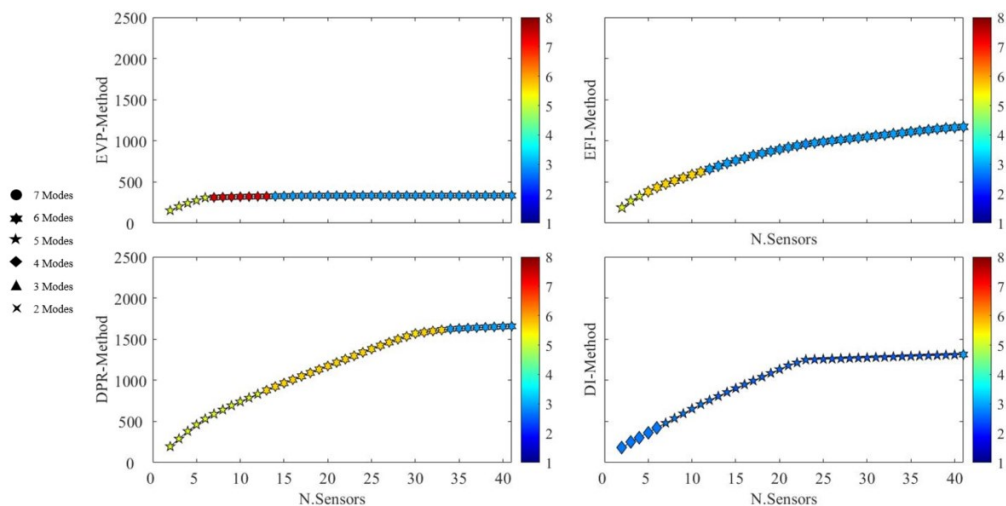


Figure 35 – Efficiency curve with frequency error, X direction

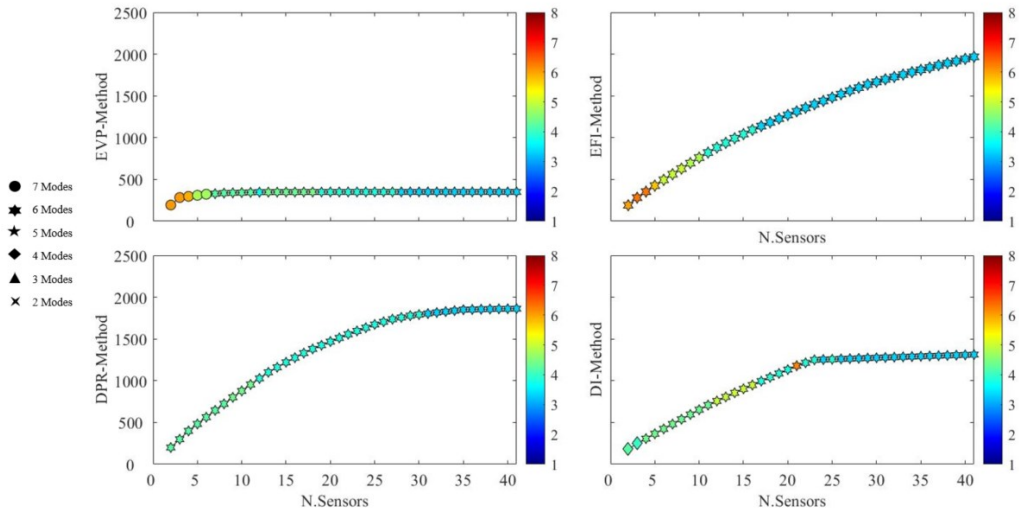


Figure 36 – Efficiency curve with frequency error, Y direction

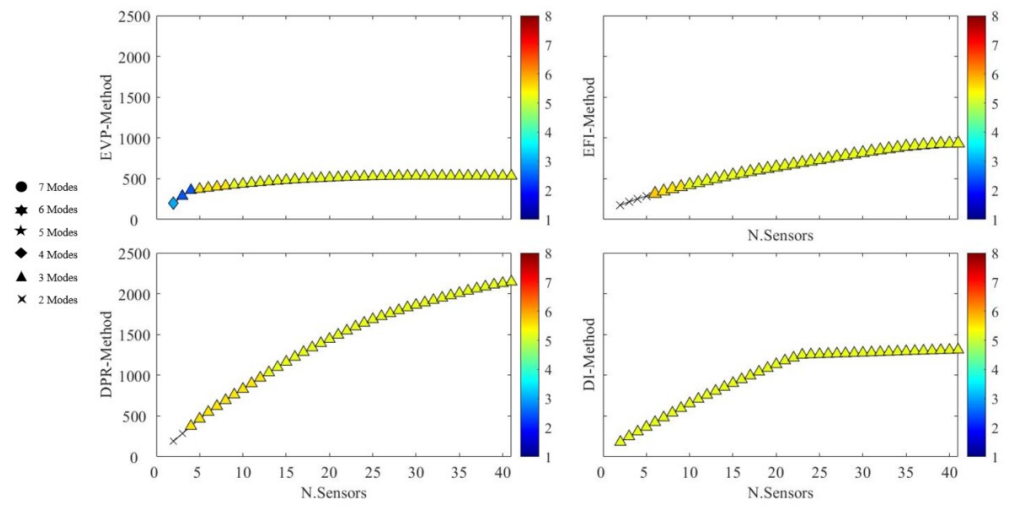


Figure 37 – Efficiency curve with frequency error, Z direction

For each direction and technique, Table 14 shows the minimum number of sensors that identify 6 modes in x, 6 modes in y, and 4 modes in z, with similar frequency error. Since triaxial sensors are often used, the last column lists the number of corresponding triaxial sensors. Both considering uniaxial and triaxial sensors, the configurations obtained with the EFI method reduces the number of sensors.

Table 14 - Results

OSP Method	Sensor's number				
	X	Y	Z	uniaxial	triaxial
EVP	14	28	9	51	36
EFI	12	17	10	39	21
DPR	34	31	13	78	34
DI	41	26	2	69	41

To compare the results with the case of $41 \times 3 = 123$ monoaxial sensors, Figure 38 shows the *MAC* results, for the two sensor configurations for each direction. In *x* direction, the 12 sensors identify the first five modes of the structure, while the sixth mode has $MAC_{6,6}$ (i.e., the 6-th element on the diagonal of the matrix *MAC*) value lower than the corresponding value in the case of 41 sensors. Similar result is obtained for the *y* direction, with the value of $MAC_{5,5}$. In *z* direction, the *MAC* values in the case of 10 sensors are lower and more scattered than those in the case 41 sensors.

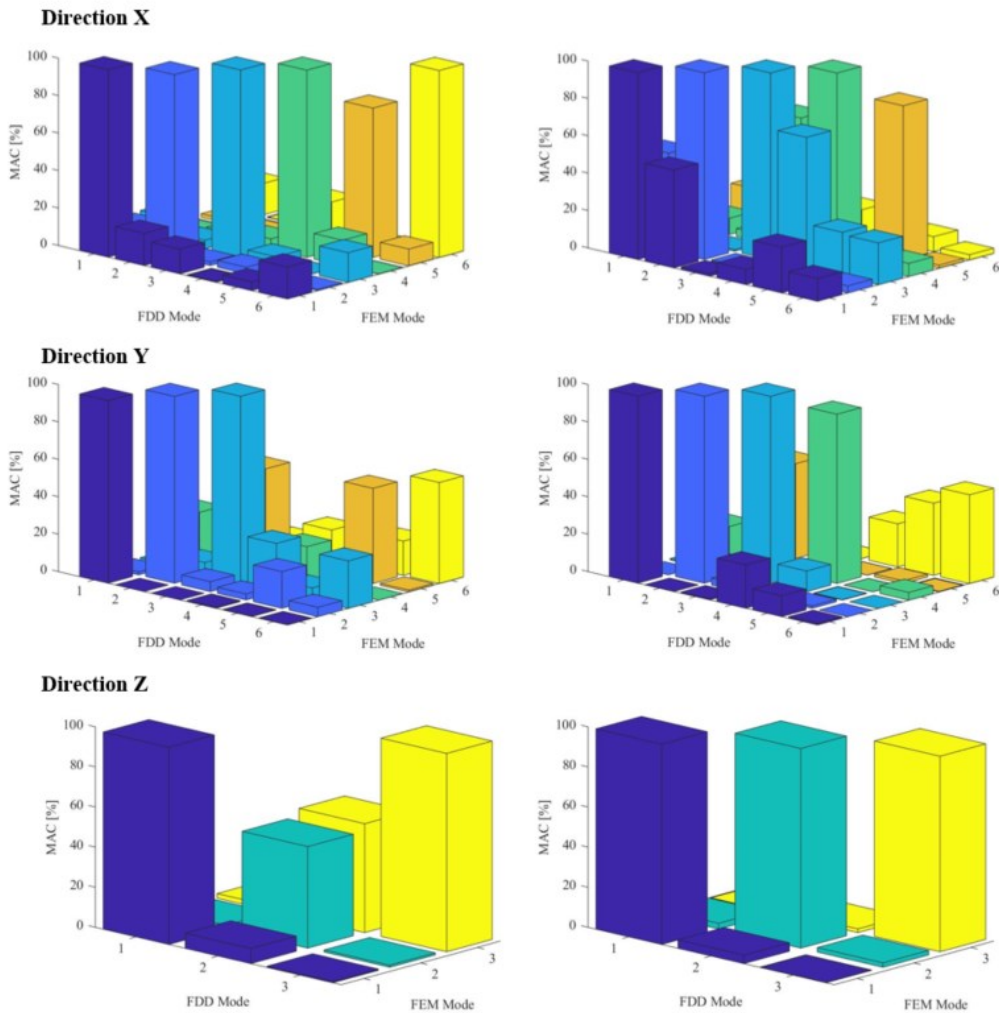


Figure 38 – MAC with all the sensors on the left and the optimal configuration on the right

3.2.1. Railway bridge of Circumflegrea (EAV)

The case study is the Circumflegrea Montesanto - Licola - Torregaveta railway viaduct at the Quarto (NA) station (Testa et al., 2022). The viaduct consists of 45 prestressed concrete decks, and each is supported on two piers spaced 24 m apart. In particular, the span between pier 29 and pier 30 (see Figure 39) was analyzed. The initial FE model is made consistent with the design in terms of geometry, mechanical properties of the materials and the permanent loads acting on the structure.



Figure 39 – The case study

The deck consists of two prestressed reinforced concrete box girders for each track. Each beam is supported by a pulvinus, and there are four transversal beams (two in the cap and two near the middle section). The width of the deck is 9.8 m. The piers have a height of 7 m. The numerical model was created in SAP2000, (CSi, 2019) (see Figure 40), with a hinge-supported static scheme. The piers and pulvinus were modeled as beam elements, while the longitudinal and transversal beams and the slab as shell elements. To simulate the presence of adjacent spans, equivalent masses concentrated on the pulvinus were adopted. The results of modal analysis are shown in

Table 15.

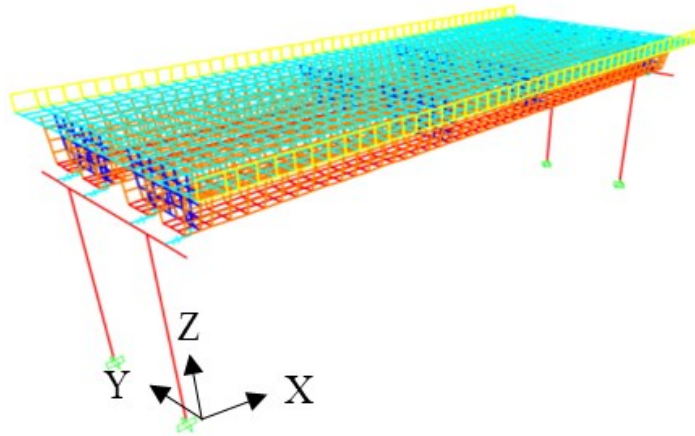


Figure 40 – FE Model

Table 15 – Analytical modal analysis

Mode	f	Mass		
	Hz	Trasl. X	Trasl.Y	Trasl Z
		%	%	%
1	3.32	100	0	0
	6.49	0	0	30
3	7.93	0	25	0
4	9.59	0	6	0
5	10.15	0	62	0
6	12.94	0	1	0
7	13.73	0	0	0
8	19.2	0	0	0
9	21.41	0	0	0
10	23.02	0	5	0
11	23.79	0	0	1
12	24.1	0	0	0

Dynamic Test

Dynamic identification is conducted with uniaxial piezoelectric sensors, characterized by high sensitivity (10 V/g) and low noise floor (0.13 $\mu\text{g}/\sqrt{\text{Hz}}$), placed on the structure. 30 measurement points were considered due to numerous uncertainties about: the degree of constraint present between beam and pile, the mechanical interaction between adjacent spans, and the connection between the two decks via a joint at the level of the two slabs.

3 test setups were designed having only 12 sensors available. The results of each setup were combined with each other in signal processing (Au, 2017).

Figure 41 shows the locations of the accelerometers: in green are the deck sensors, in red those located on the beams, and in blue those on the pulvinus. Specifically, the directions for each sensor are shown in green for setup 1, orange for setup 2, and blue for setup 3. In black are shown the 3 sensors common to all three setups, which are the reference points needed to combine the information of all setups and to obtain the modal shapes of the bridge.

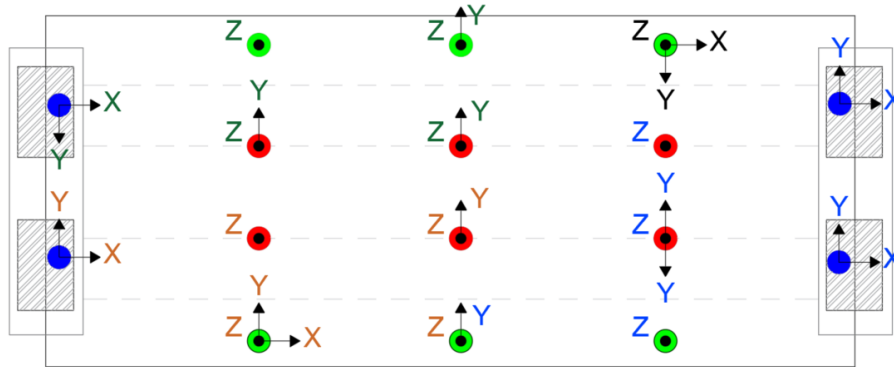


Figure 41 – Sensors’ placement

Time series of 45 minutes (2700 seconds) were acquired for each setup at a sampling rate of 100 Hz. Assuming that many modes will have frequencies in the 0.2 to 25 Hz band (De Angelis et al., 2021), the data were filtered using a Butterworth-type bandpass filter with order 6 in the 0.2 to 25 Hz range and then decimated to a final sampling frequency of 50 Hz. This significantly reduces the amount of samples without loss of information in the frequency range of interest.

The modal frequencies are obtained as the average of the values obtained from each setup (Van der Auweraer H. et al., 2000; Mevel L. et al., 2019). On the other hand, modal shapes are obtained by scaling those of each setup so as to minimize the error - calculated by the method of least squares - relating to the modal shapes of measurement points common to multiple setups (Au, 2011). The procedure is applied to pairs of setups and finally combining the results of all setups with each other. The computations were performed using ARTeMIS Modal Pro software (Structural Vibration Solutions ApS, 2019). The FDD technique allowed to identify 5 vibration modes shown in Figure 42 and Table 16. The operational modal analysis did not identify all the modes predicted by the analytical modal analysis.

Table 16 – Experimental results: frequency

Mode	1	2	3	4	5
Freq. [Hz]	2.49	3	6.79	11.26	19.07

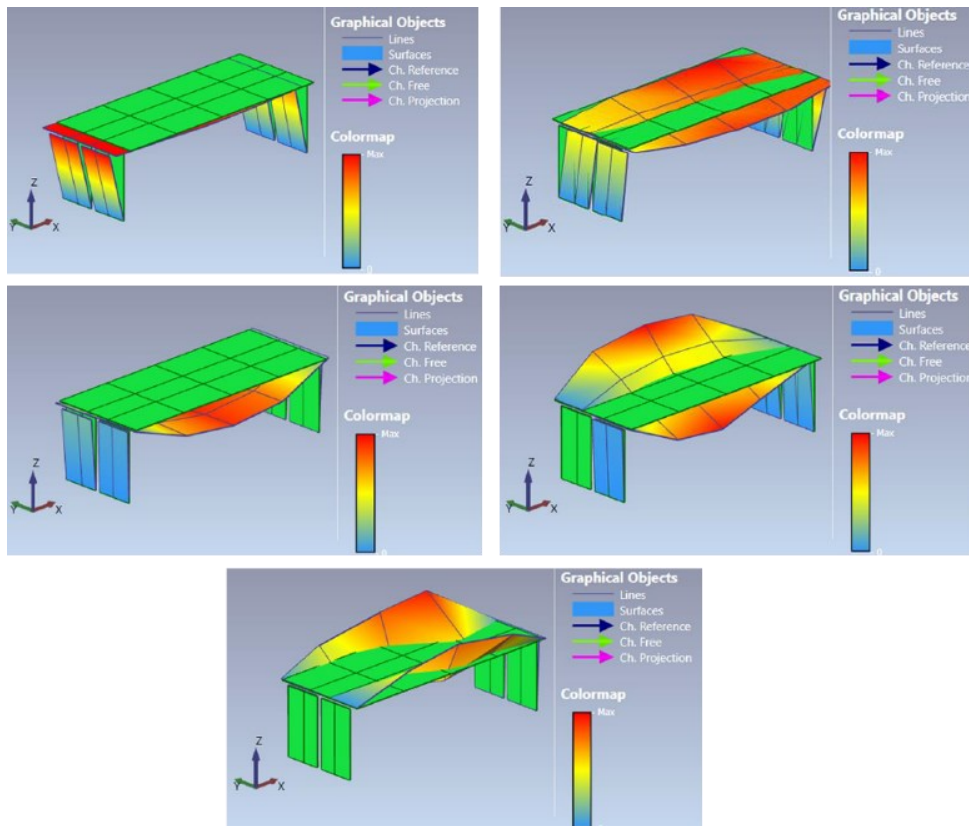


Figure 42 – Experimental results: modal shapes

Model Updating

With reference to the first three modes of vibration of the structure, the comparison between the analytical and experimental modal analysis sheds light on the need to perform updating of the numerical model in order to have a better correspondence with the real structure (see Table 17).

Table 17 – Comparison between real behavior and numerical ones

	Mode 1	Mode 2	Mode 3
	f - Hz	f - Hz	f - Hz
Experimental results	2.49	3.00	6.79
Numerical results	3.32	10.15	6.49

The update of the numerical model concerns the deformability of the constraint between the deck and the pile. Specifically, the hinges – represented by links in FE model - were made deformable in x and y direction by adopting a stiffness of 21000 kN/m in x direction and 22000 kN/m in y direction.

A frequency comparison between the experimental modes and the corresponding numerical modes is shown in Table 18. The correspondence about the modal shapes is shown through the MAC matrix in Figure 43. A good correspondence in frequency and about the modal shapes is evident. For the first two modes the MAC improves (about

65%) compared to the initial case (without updating). Similarly, the converse is true for the fifth identified mode (about 95%).

Table 18 – Frequency comparison

Mode	$f_{exp.}$	$f_{num.}$
	Hz	Hz
1 (1)	2.49	2.48
2 (2)	3	3.04
3 (8)	6.79	6.49
4 (9)	11.26	10.03
5 (11)	19.07	14.9

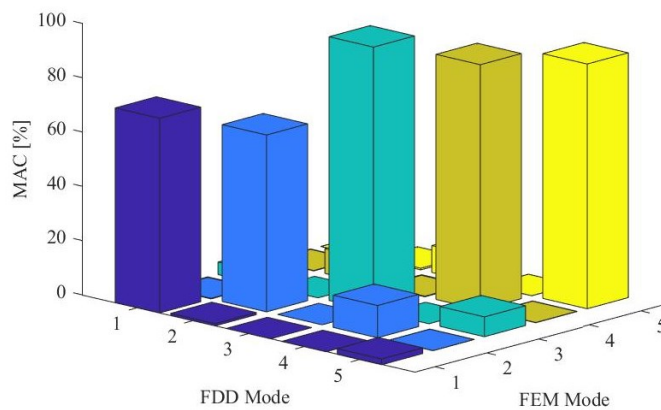


Figure 43 – MAC

OSP Application

Starting from the updated model, the EFI method and the selection criterion based on frequency error were implemented. The initial sensors' configuration is equal to experimental one. The aim of the analysis is to validate the proposed criterion for optimizing the position of the accelerometers and to test the future possibility to reduce the number of sensors. The test was carried out in order to demonstrate that the selection criterion allows to reduce the number of sensors obtaining the same level of accuracy of the results of the dynamic identification process performed with the records of 30 sensors (in 3 setups).

Figure 44 shows the cumulative EFI efficiency coefficient associated with each sensor setup; the same figure also shows the frequency error E (marker color) and the number of identified modes (marker shape). Let's note that, the first two sensors in the EFI ranking (first configuration) allows the identification of two vibration modes with an overall error of 0.10 Hz. Using the first three sensors (second configuration) increases the number of identifiable modes (two modes of vibration) with a higher error (0.30 Hz). Finally, the first three modes of vibration can be identified with the first eight sensors in the ranking with a frequency error of 0.35 Hz.

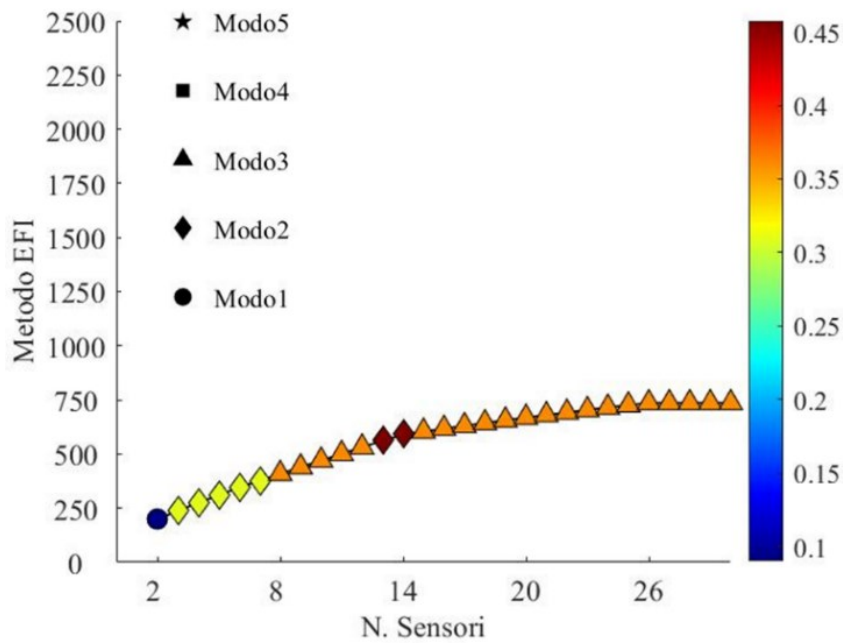


Figure 44 – Efficiency curve

Thus, the experimental data - i.e., the accelerations recorded for each setup - can be processed again using only the first eight sensors of the ranking list i.e., the obtained optimal configuration.

However, the initial subdivision into setups dictates that the fixed triaxial sensor (see Figure 41 - sensor in black) should be considered, regardless of the indications provided by the OSP criterion. Therefore, the identification procedure with experimental accelerations is performed again with the sensor setup shown in Figure 45.

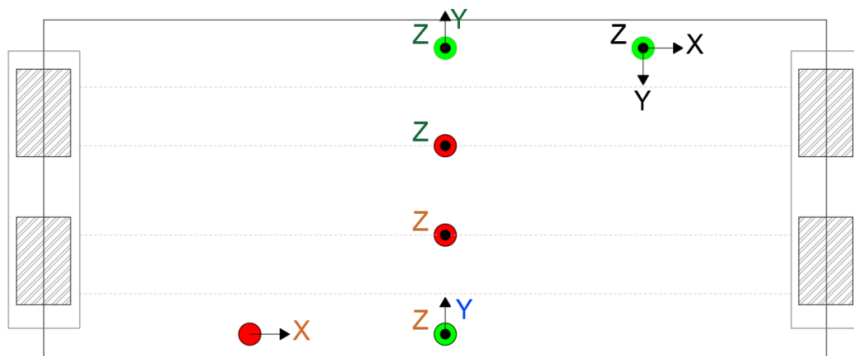


Figure 45 – Optimal sensor configuration

In Table 19, the frequency results are synthesized. The comparison between the frequencies obtained with 30 (f_{SPER}) and 10 (f_{OSP}) sensors shows that the maximum difference is about 1%. Therefore, the optimal configuration allows to maintain the level of accuracy of the dynamic identification. In addition, the number of sensors of the optimal configuration is equal to the number of the available sensors: in other words, if the dynamic identification had been conducted with ten sensors it would not have been necessary to resort to the combination of different sensor setups.

About the modal shapes, there is a worsening in the identification of the second vibration mode, while for the remaining modes the value of the MAC tends to the unit on the main diagonal (see Figure 46).

Table 19 - Frequency comparison

Mode	f_{SPER}	f_{OSP}
	Hz	Hz
1	2.49	2.49
2	3	3.00
3	6.79	6.79
4	11.26	10.65
5	19.07	19.04

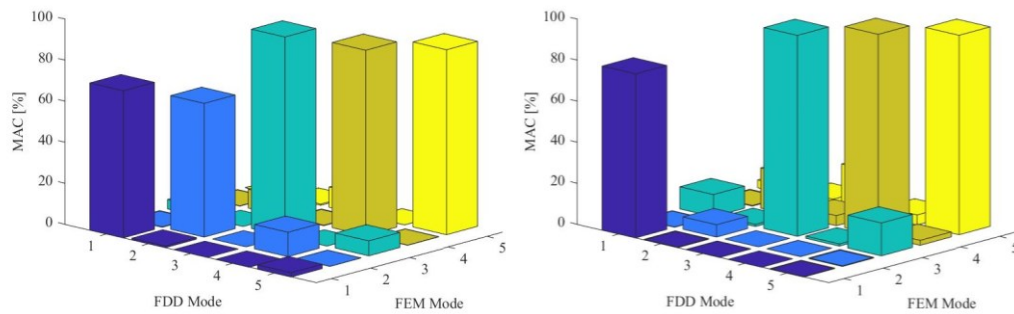


Figure 46 – MAC comparison

Another application of the optimization procedure was performed assuming a regular mesh as the initial configuration of the sensors as shown in the Figure 47. The purpose of the analysis is to define a sensors configuration to be used for future testing. Again, the test shows that the selection criterion allows reducing the number of sensors ensuring the high level of accuracy of the results of the dynamic identification process. The initial configuration consists of 12 biaxial sensors (y and z) located on the beams, 9 triaxial sensors on the slab, and finally one biaxial sensor (x and y) on each pulvinus.

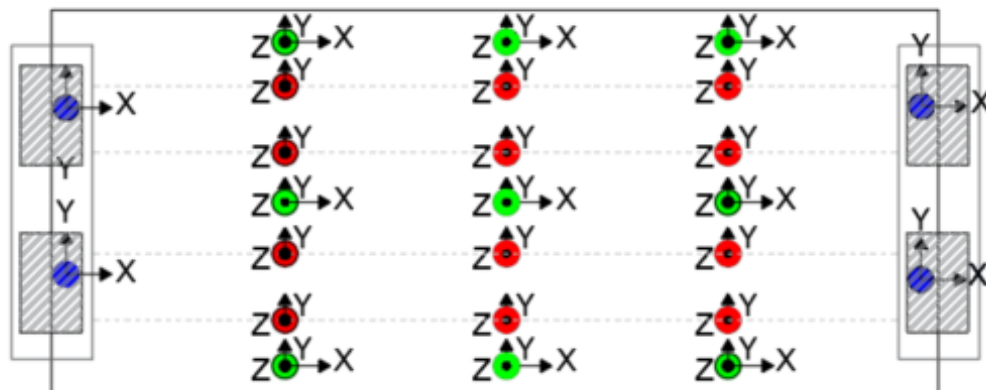


Figure 47 – Initial sensors configuration, regular mesh

In this case, the efficiency curve (see Figure 48) shows that the first vibration mode can be identified with the first 11 sensors of the EFI ranking and with a low frequency error (about 0.1 Hz). Using up to the first 21 sensors of the ranking, two vibration modes are

identified with a frequency error of about 0.3 Hz. Finally, three vibration modes are always identified with a constant error, using the first 22 sensors of the ranking. Thus, the optimal configuration consists of the first 22 sensors of the ranking (see Figure 49).

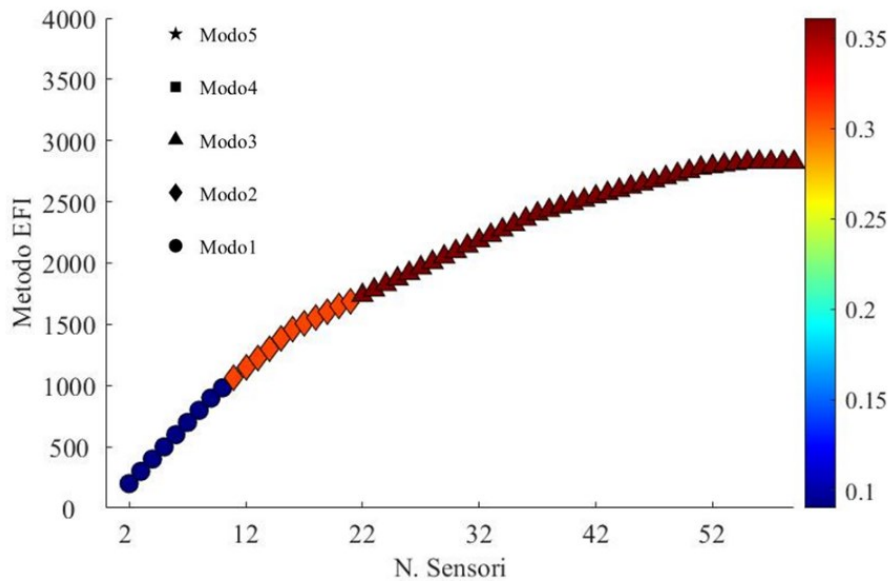


Figure 48 – Efficiency curve

The dynamic identification process - simulated with the accelerations obtained from numerical model at the points identified by the optimization algorithm – allows to identify the first 3 vibration modes with a diagonal MAC (see Figure 50).

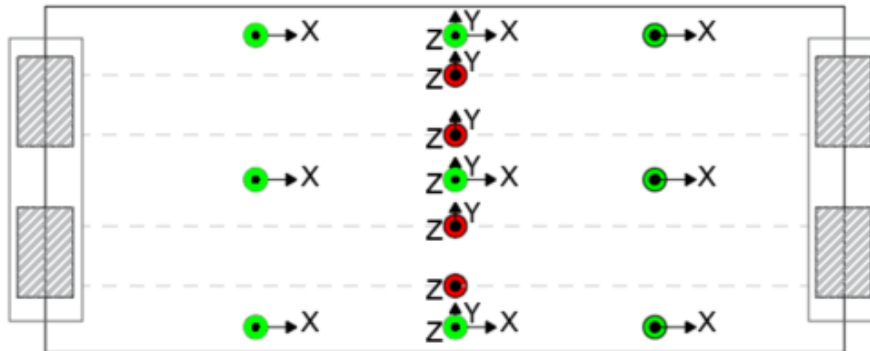


Figure 49 – Optimal solution

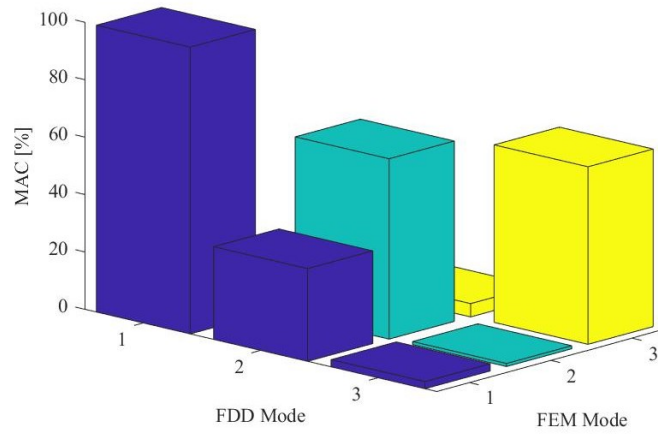


Figure 50 – MAC

3.3. Model Updating

As previously mentioned, in this section the updating process of a real steel-concrete composite bridge is described in order to highlight the need to: (i) perform the updating without the adoption of automatism and, thus, to detect the possible physical phenomena that cause the variations performed on the numerical model; (ii) use the results of dynamic and static tests to update the FE model (Bilotta et al., 2021). In the literature, there are automatic optimization algorithms that act directly on the mass and stiffness matrices of the structure in order to minimize the error between numerical and experimental behavior. Although these techniques make it possible to reduce analysis time, there is a risk of not understanding the causes of the variations introduced in the model such as, for example, the degree of constraint between the deck and the column. For this reason, a manual updating process is preferable because it allows critical analysis of variations. On the other hand, the numerical model updating performed only with static test results does not allow to capture some localized phenomena - often caused by modeling simplifications - that may alter the behavior of the structure.

3.3.1. Tammarecchia Bridge

The case study is the Tammarecchia bridge, located on Ex-Statale 625, and it connects the municipalities of Campolattaro and Circello in the province of Benevento (Italy). The bridge has a total length equal to 36.00 m and it is 12.05 m wide. The deck of steel-concrete composite bridge consists of four single-span beams. The main steel beams (S355J0W) are in welded composition I-section, and they are characterized by a variable height- from a maximum of 1.9 m at the sup-port section to 1.5 m at the middle span. At the extrados of the steel elements, a collaborating concrete slab (C28/35), equipped with reinforcing steel bars (B450C), is made on prefabricated predalle that it is 6cm thick. So, the slab's total thickness is 30 cm. In addition, the external cross-pieces are made in welded composition sections one meter high, and they are connected to the main beams by a bolted connection. Instead, the intermediate crosspieces consist of an IPE600 section, and they are placed every 6.0 m along the longitudinal direction. The deck is supported by reinforced concrete retaining walls the act also as abutments. They have a maximum height equal to 5.4 m of which 2.75m for the arrangement of pulvinus (1.2m thick) and 2.75 m for the gravel (0.4m thick).



Figure 51 – Tammarecchia bridge

In accordance with the structural project provided by the designer, the first finite element model is developed, namely Model 0. Modeling has been simplified. Indeed, the four principal beams are modeled as equivalent steel-concrete composite beams. Beams are modeled as steel frame element (1-D) and the slab's longitudinal contribution is considered increasing the inertial properties of the section. So, the properties of equivalent beams are calibrated taking into account the portion of collaborating slab with the metal profile. The transverse connection between the beams is provided: (i) by the reinforced concrete slab (C28/35) discretized with cross-beams, i.e. transverse frame elements (1-D) connected to the main beams through rigid links and (ii) by the crosspieces (S355) modeled as frame elements (1-D) and connected to the main beams through the use of rigid links (see Figure 52). Figure 52 shows the extruded view of the deck. Finally, the constraint conditions are defined according to the project scheme, i.e., they are simple supports as shown in Figure 53.

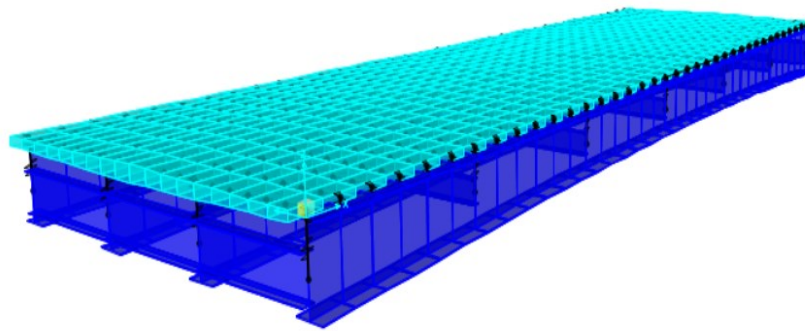


Figure 52 – FE Model

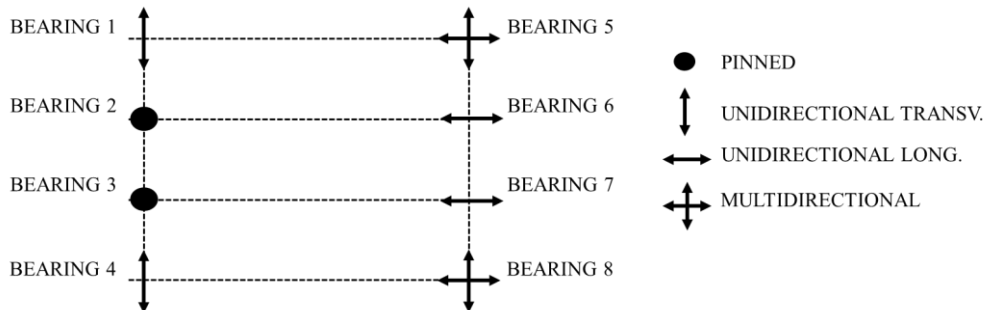


Figure 53 – External constraint

During the testing phase of the bridge ($T=0$), static and dynamic load tests were carried out on the bridge. In the static tests, loads at serviceability limit state (SLS) are applied in order to induce the maximum operating stresses related to the rare characteristic load combination on the structure. For this reason, the designer provided the distribution of the vehicles with their masses on the deck. Four load phases characterized by the presence of different vehicles have been programmed for the load test. In this work, the considered phase is the most severe condition that involves the presence of 8 vehicles on the deck in a specific position.

Figure 54 shows the considered load scheme where the red squares represent the spatial distribution of the vehicles' axes on the deck. For reading the displacements through LEICA LS10 topographic station, the identified 12 measuring points are represented in

Figure 54 with the empty circle symbols. In particular, the displacements were measured near the supports (shoulder A and B) and in the middle span for each beam. The dynamic tests involved the use of piezoelectric triaxial accelerometers (MEMS) connected to an acquisition control unit. Five sensors are placed on the beams 3 and 4 and they are represented with the full circle symbols in Figure 54. Two sensors are placed in the middle of beams, 2 sensors are placed at 3/4 of their length, and 1 sensor is located near the abutment A on beam 4. The accelerations were processed according to the application of the Operational Modal Analysis technique (OMA) (Au, 2017).

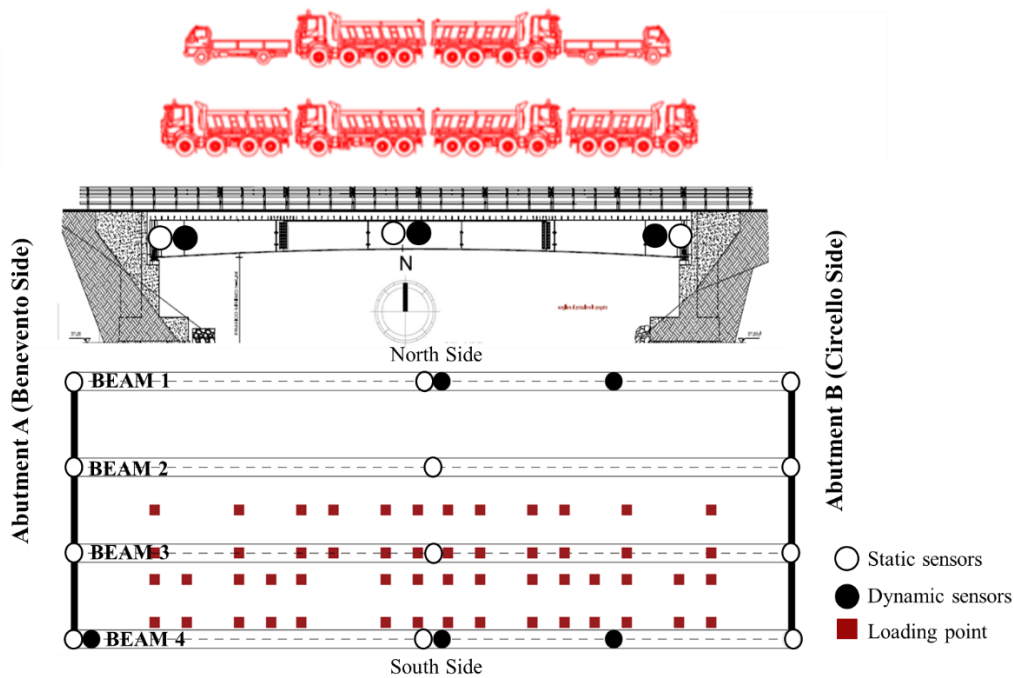


Figure 54 – Tests setup and load schemes

The displacements of each beam are obtained by the static tests, and they are compared with the results of FE model (Model 0). Table 20 shows the comparison between the experimental displacements (Meas.) and the numerical ones (Model 0) in the middle span for each beam (B1, B2, B3, B4). Let's note that the real displacements are generally smaller than numerical ones with significant errors ε (greater than 25%) for each beam. In this preliminary phase, the displacements measured near the supports during the load test aren't shown, because the comparison is not possible. Indeed, the numerical displacements of the supports are zero in the Model 0 due to the imposed constraint conditions in the structural project.

Related to the dynamic tests, the processing of natural frequencies and modal shapes was performed using the Frequency Domain Decomposition technique (FDD). In Table 21, the frequencies obtained by the analytical modal analysis (FE model) are compared with the experimental ones (obtained by FDD). By the dynamic identification results, let's note that the real structure is more rigid than the theoretical design model. In fact, an error of 31% and 24% are observed for the first and second vibration modes, respectively.

Table 20 – Static comparison

Beam	Meas.	Model 0	ϵ
-	[cm]	[cm]	-
B1	0.92	1.2	30%
B2	1.06	2.48	134%
B3	2.97	3.73	26%
B4	3.15	4.87	55%

Table 21 - Dynamic comparison

Mode	FDD	Model 0	ϵ
-	[Hz]	[Hz]	-
1	4.08	2.83	31%
2	4.98	3.77	24%

Since the bridge’s real behavior is different from the prediction of the numerical model based on the structural design, the model update is necessary. It is carried out through three phases in order to highlight the contribution of static and dynamic tests:

- Phase 1: Calibration of the numerical model (Model 1) with the dynamic test’s results and verification of static behavior.
- Phase 2: Calibration of the constraints’ vertical stiffness (Model 2) according to the results of the static test (i.e., using the supports' experimental displacements) and check of dynamic behavior.
- Phase 3: Refinement of the model (Model 3) to improve the match with the transverse deformation of the deck.

In phase 1, only on the base of the dynamic results (i.e., the two experimentally identified modes), the most significant parameters for the model updating were identified through a sensitivity analysis. Figure 55 shows the influence of the concrete elastic modulus on the dynamic response while Figure 56 shows the influence of flexural rotational stiffness of the external constraints. On the hand, the increase of the materials' elastic modulus - within realistic limits- does not allow to achieve a satisfactory improvement. On the other hand, the flexural rotational stiffness of the constraint (R_2) significantly affects the dynamic response. Indeed, an excellent correspondence with the experimental frequencies is obtained assuming $R_2 = 1,5 \cdot 10^6$ kNm/rad for each constraint (see Figure 56).

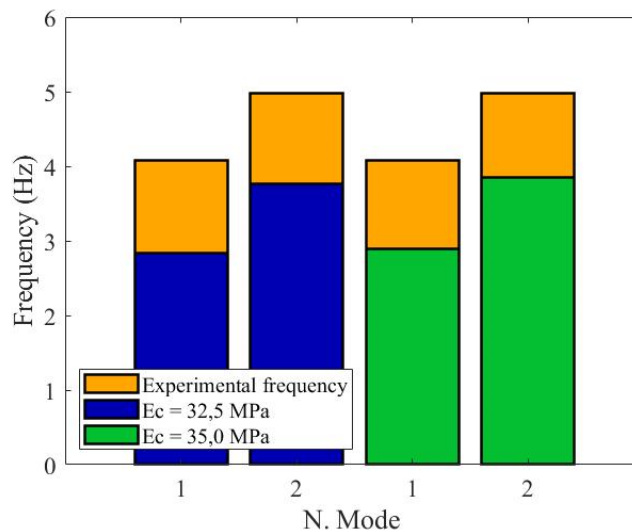


Figure 55 – Sensitivity analysis: concrete elastic modulus

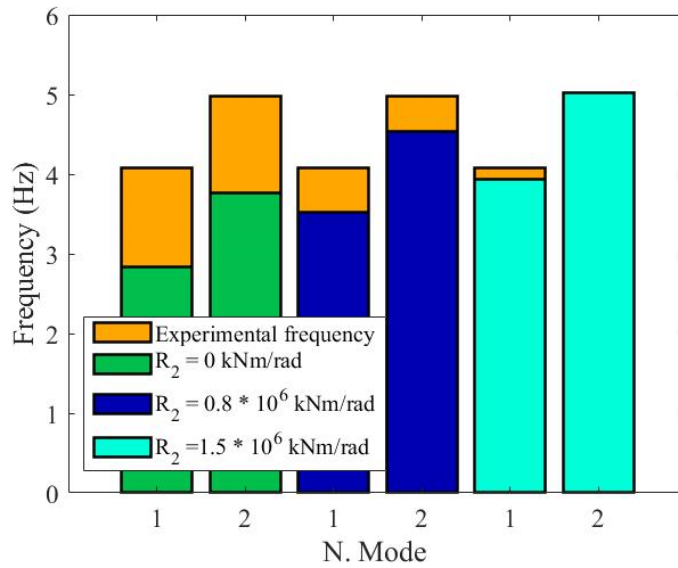


Figure 56 – Sensitivity analysis: flexural rotational stiffness

Assuming R_2 equal to $1,5 \cdot 10^6$ kNm/rad, the difference between the real dynamic behavior and the simulated one through FE model improves. In fact, frequency errors are reduced (about 20%) as shown in Table 22.

Table 22 – Comparison between Model 0 and Model 1 about the modal frequency

Mode	FDD	Model 0		Model 1	
		FE	ε	FE	ε
-	Hz	Hz	%	Hz	%
1	4.08	2.83	31	4.03	1
2	4.98	3.77	24	5.13	3

About the modal shapes, the correlation between experimental modes and theoretical ones was analyzed through the MAC. Figure 57 shows a good correlation between numerical shapes and experimental ones because values on the main diagonal is greater than 0.75 while outside the diagonal values below 0.25.

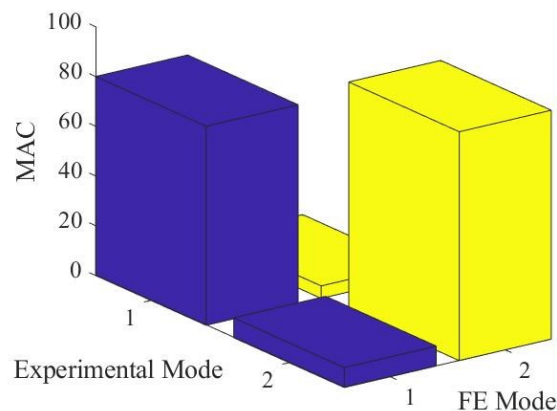


Figure 57 – MAC with Model 1

For the check of static behavior, the experimental load scheme is implemented in the updated model in order to simulate the operating condition (SLE) (see Figure 54). Figure 58 shows the transversal deformation, i.e., the vertical displacement read in the middle section of each beam. The black line represents the experimental measurements, while the blue line the numerical ones. From the comparison let's note that there is an important percentage error on the B2 beam equal to 75%. In particular, the deformation of the numerical model is consistent with Courbon's hypothesis (Courbon, 1971), while the experimental indicates a different distribution of loads in a transverse direction. Instead, for the beam 4 (B4) where theoretically the maximum internal force is expected, the error in percentage between the theoretical and the experimental lowering is equal to 2%. In Table 23, the results are summarized.

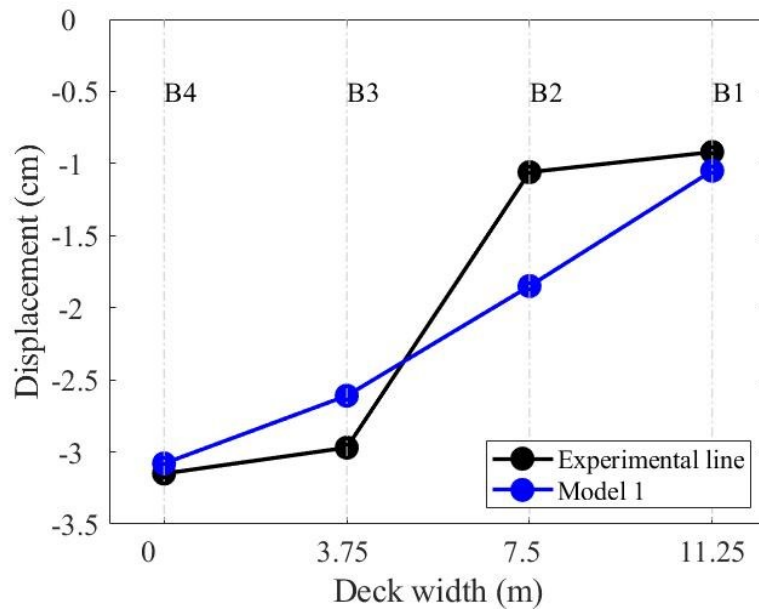


Figure 58 – Transversal deformation – Model 1

Table 23 – Static comparison – Model 1

Beam	Exp.	Model 0	Model 1
-	[cm]	[cm]	[cm]
B4	3.15	4,87 (55%)	3,08 (2%)
B3	2.97	3,73 (26%)	2,61 (12%)
B2	1.06	2,48 (134%)	1,85 (75%)
B1	0.92	1,2 (30%)	1,05 (14%)

In the second phase of model updating (Model 2), the calibration of the constraints 'vertical stiffness is carried out according to the experimental displacements read near the supports. The calibration is an iterative process where the stiffness of constraint varies until the numerical displacement is equal to the experimental one, for each support. So, it is established whether to increase or reduce the stiffness of the vertical spring (U3) at each iteration from the comparison between the numerical and experimental displacements.

However, the calibrated yielding for each support inevitably involves a loss of stiffness of the numerical model, as shown by the reduction in terms of frequencies of the first and second vibration mode (see Table 24).

Table 24 – Dynamic comparison, Model 2

		Model 0		Model 1		Model 2	
Mode	FDD	FE	ε	FE	ε	FE	ε
-	Hz	Hz	%	Hz	%	Hz	%
1	4.08	2.83	31	4.03	1	3.96	6
2	4.98	3.77	24	5.13	3	5.04	2

In addition, there is no significant variation of the transverse deformation in the middle section of beams, as shown in Figure 59. In fact, the blue line that represents the numerical deformation of the Model 1 tend to overlap with the purple line, i.e., the transversal deformation of the Model 2. Both blue and purple lines are very different from the black line that is the experimental measurements.

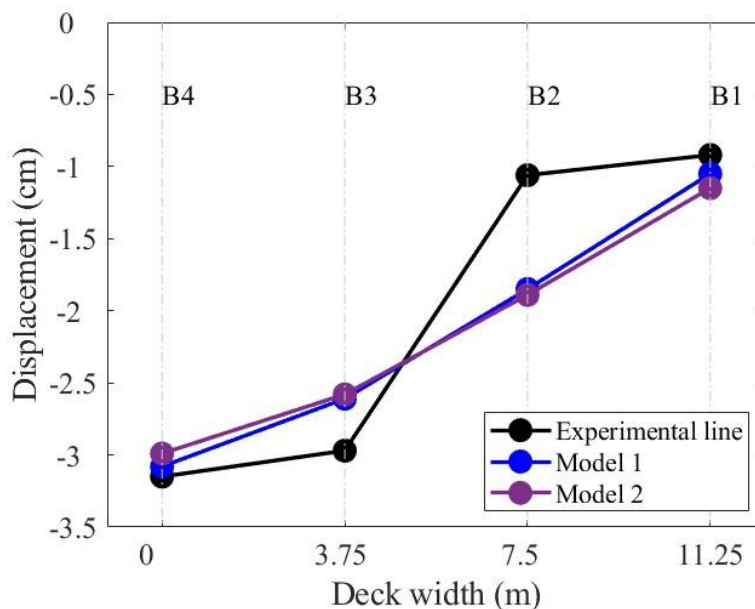


Figure 59 – Static comparison, Model 2

Finally, in the third phase, the model update (Model 3) was refined to obtain a transverse deformation of the deck similar to the experimental one. In this case, the problem is affected by the collaboration between the four beams, that is the connections between the beams and slab and between beams and crosspieces. The possible causes of this physical phenomenon could be: (1) the transversal deformability of the metal profile and (2) the probable presence of localized effects. Related to (1), the real crossbar is connected to the web of the metal profile, but in the numerical model –since beams are modeled as equivalent composed element - the connection is more rigid because the beam has the torsional stiffness of the entire composed section. With reference to (2), the localized effects are attributable to possible slides at the steel-concrete interface and to the weakening of the beam-slab connection due to the presence of prefabricated predalle.

In order to obtain a good correspondence between the numerical and experimental behavior, a sensitivity analysis was performed on the trend of the transverse deformation (in reference to the middle span of beams) varying the internal constraining condition (beam-slab and beam-crosspiece).

Related to the static behavior, Figure 60 shows the transverse deformation obtained by the on-site tests (represented with black line) and the numerical one by Model 0 (grey line), Model 1 (blue line), Model 2 (purple line) and Model 3 (green line).

The identified transverse deformation (represented with grey line) is equivalent to that of Model 2 because it is obtained with a stiffness value equivalent to a perfect interlocking (20,000 kNm/rad). The deformation related to the Model 3 is obtained with the flexural stiffness of the beam-crosspiece connections equal to 12,000 kNm / rad and the bending stiffness of the beam-slab connections equal to 1,000 kNm / rad.

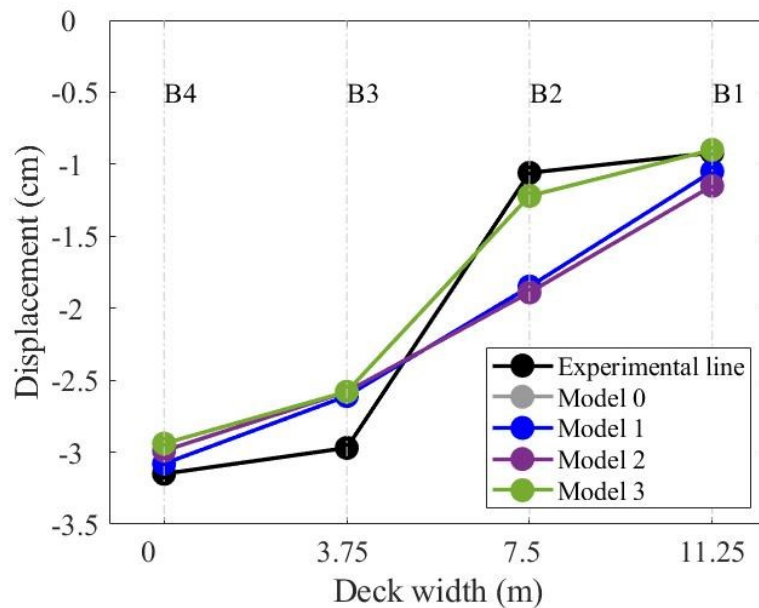


Figure 60 – Static comparison, Model 3

Finally, for Model 1, the displacements obtained by the updated FE model and the experimental ones are particularly different for the B2 beam (i.e., 75%). The trend of the numerical model's deformation is linear according to the Courbon hypotheses, while the experimental deformation shows a transverse distribution of loads different from that hypothesized. This leads to errors of approximately 10% for the B1 and B3 beams. Related to the dynamic behavior, there is a good correspondence in terms of natural frequencies with errors less than 5%.

In the case of Model 2, an excellent correspondence is also obtained in terms of frequencies and modal shapes. However, for the static behavior, the trend of the deformation is not satisfactory because there is a significant error at the B2 beam (i.e., 78%).

In the Model 3, the introduction of flexural releases for the connections between beams and slab and beams and crosspieces and a further update of the supports' flexural stiffness - differentiating between beam types (internal and external ones) - has allowed to obtain a clear improvement for the static behavior.

However, in this case, a worsening is achieved about the vibration mode 2 due to the reduction of torsional stiffness. In fact, according to Kollbrunner and Basler

(Kollbrunner and Basler, 1969), the secondary torsion is not negligible compared to the primary one for this bridge. Since the secondary torsional stiffness depends on flexural one, the application of flexural releases produces a reduction of system's torsional stiffness. For this, it has been decided to accept a maximum frequency error equal to 10%.

Table 25 and Table 26 summarize the results shown in terms of transverse deformation and modal frequencies respectively.

Table 25 – Vertical displacement

Beam	Meas.	Model 0	Model 1	Model 2	Model 3
-	[cm]	[cm]	[cm]	[cm]	[cm]
B1	0.92	1.20 (30%)	1.05 (14%)	1.15 (25%)	0.90 (2%)
B2	1.06	2.48 (134%)	1.85 (75%)	1.89 (78%)	1.22 (15%)
B3	2.97	3.73 (26%)	2.61 (12%)	2.58 (13%)	2.58 (13%)
B4	3.15	4.87 (55%)	3.08 (2%)	2.99 (5%)	2.94 (7%)

Table 26 - Frequency

Mode	Sper.	Model 0	Model 1	Model 2	Model 3
-	[Hz]	[Hz]	[Hz]	[Hz]	[Hz]
1	4.08	2.83 (31%)	4.03 (1%)	3.96 (3%)	4.16 (2%)
2	4.98	3.77 (24%)	5.13 (3%)	5.04 (1%)	4.55 (9%)

In figure the results shown for the case study of Ponte Tammarecchia are summarized. For each model, the percentage of error between the numerical vertical displacements and the experimental ones for each beam in the middle section is shown in the graph above. The red dotted line indicates the acceptable error limit (15%).

For each identified vibration mode and for each model the error in terms of modal frequency and MAC is shown below. Once again, the red line indicates the accepted limit of 10%.

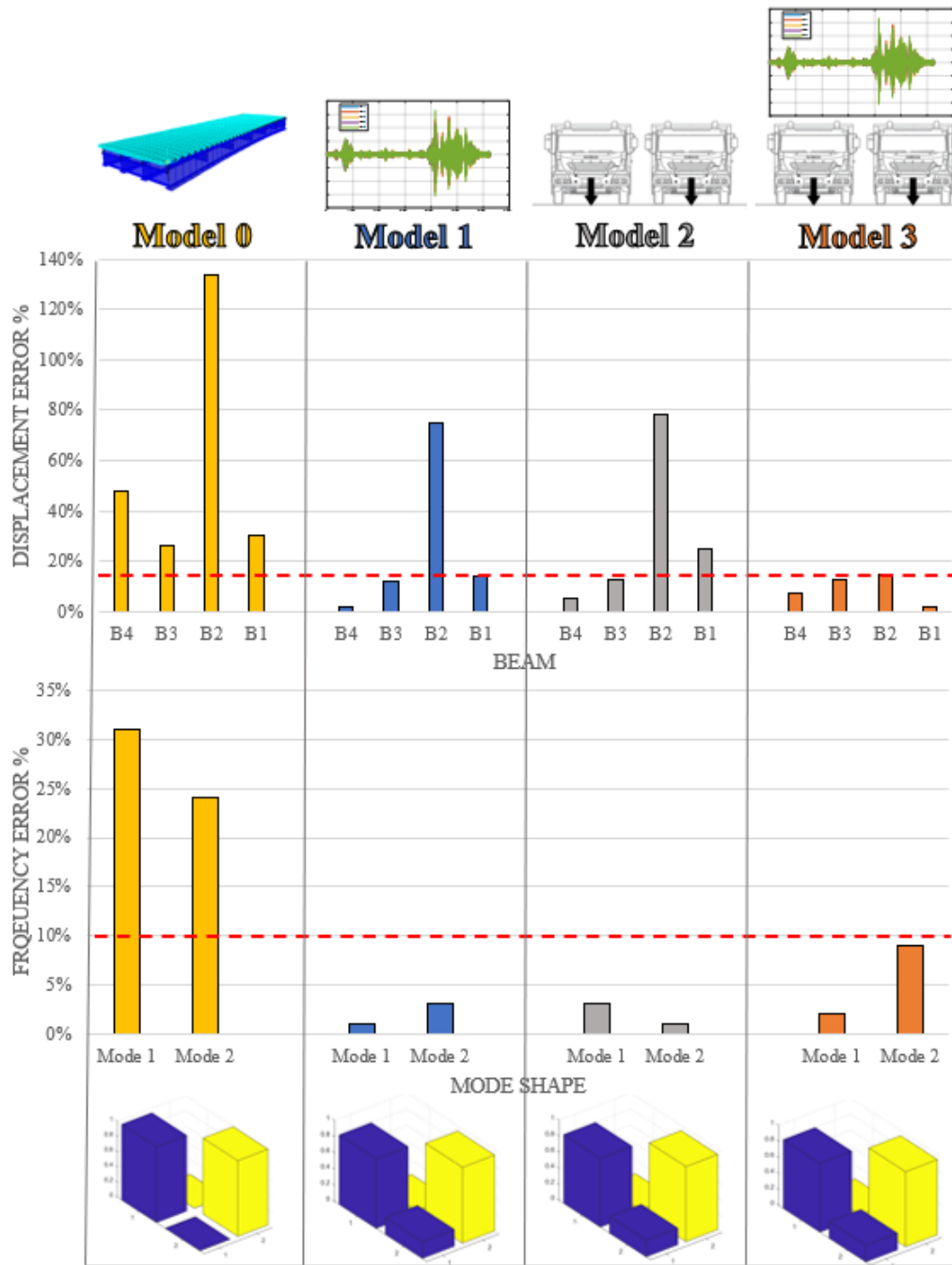


Figure 61 – Comparison of updated models

3.4. Conclusions

In this chapter, two topics for structure monitoring based on dynamic identification are aproned namely sensor optimization techniques and model updating. Indeed, dynamic identification allows the identification of structure's dynamic proprieties that can be used in order to: (i) update the numerical model and (ii) identify structural damage over time either through a data driven approach by establishing a damage threshold or a model-based approach with the FE model of the structure. The described case studies showed that the executive design of a monitoring system requires optimization techniques for selecting the sensors' number and location. In particular, the adoption of optimal sensor placement techniques makes it possible to increase the accuracy of the dynamic identification process by optimizing the number and location of sensors. The EFI technique allows to derive an efficiency ranking of sensor locations, but a criterion for selecting the optimal number is not defined. The proposed criterion based on numerical simulations of the FDD technique allows to define an optimal sensors configuration that minimizes the number of instruments and maximizes the level of accuracy of the FDD results. For the described case study, the FE model of the bridge was updated on the basis of the dynamic identification results and then used to implement a method of Optimal Sensor Placement. The process of model updating has allowed to reduce the uncertainties of modeling and then, to refine the numerical model. After, the FE model is used for the design of a network of sensors. The selection criterion - added to the OSP method and applied to the configuration of sensors coinciding with that of the dynamic test - allowed to reduce the number of sensors guaranteeing the same level of accuracy of the FDD. The OSP method applied to the regular mesh of sensors allowed to define the possible sensors configuration to be used for future testing.

About model updating, the use of dynamic results in the model update process does not allow to predict some phenomena due to local effects (for example, the transverse deformation of the non-linear scaffold). Conversely, the update performed with the use of static results fails to represent some global phenomena (for example, secondary torsion). The combined use of dynamic and static tests enables to obtain a representative numerical model of actual structural behavior for the load levels reached during the tests. The updated model can be used as a tool for detecting anomalies over time, but also for structural safety checks. Regarding the OSP methods, note that the definition of the optimal configuration of the sensors cannot be released from the use of the FE model of the structure on which to perform preliminary analysis. Therefore, the definition of the optimal configuration must be realized by means of a numerical model corresponding to the real behavior of the structure.

This implies that: (i) on the one hand preliminary site testing with a network of sensors defined on the basis of possible expected structural behavior must be carried out in order to be able to perform the model update; (ii) the presence of future damage on the structure can significantly alter the dynamic behavior of the structure that would no longer correspond to the FE model. The latter should therefore be updated again.

The use of state-of-the-art techniques based on genetic algorithms does not ignore the problem identified. On the other hand, the employment of techniques of artificial intelligence with supervised approach that is simulating all the possible conditions of damage on the structure, would allow to bypass the problem with a high computational burden. In the future, the issue will be invested in more detail.

Traffic load models for accurate safety checks

The previous chapters reviewed the main structural monitoring techniques in order to identify the health status of existing bridges under operational conditions. However, the safety of existing bridges must also be checked against the ultimate limit state.

For safety checks, the updated model by dynamic identification is a necessary tool to be able to derive the stresses and deformations caused by the traffic loading schemes required by the regulations. However, the load schemes imposed by the standard may be too conservative for existing bridges compared to the usual traffic flow they are subject to. Therefore, this section describes a methodology for estimating the rare percentile of traffic load starting from the actual distribution of traffic flows affecting the road network in which the bridge is embedded.

The aim is to obtain the annual distribution of maximum internal forces in the bridges. This output allows to (i) probabilistically frame the code-based traffic loads through a network-specific micro-simulation and (ii) to perform structural safety assessment of the bridges with a network-specific characterization of the uncertainty in the traffic loads, compared to conventional code. The presented study is based on the adoption of micro-simulations, involving the entire real transportation network. In fact, since the traffic flow on a specific bridge or highway section is the result of a dynamic combination of time-varying demand (D) and supply (O) flows, simulation of the O/D flows of a closed network is essential to be able to reconstruct the density and distribution of vehicles on each bridge or other segment, unless time inflows and outflows are monitored for that bridge.

To obtain the annual frequency distribution of structural actions on the bridges in the network, a methodology consisting of two main parts. The first part is devoted to modelling the daily demand-supply scenarios for the network of interest in order to be able to simulate the traffic flows on the road network for one year. The output of the simulation consists of the spatiotemporal trajectory of each specific vehicle circulating on the road network. In the second part, the simulation output is transformed into bridge loads i.e., a probabilistic analysis of traffic-induced structural actions is performed after the vehicle axle forces acting on the bridges have been determined and following structural modelling of the bridges (Testa et al., 2023).

4.1. A56 – Tangenziale di Napoli

The A56 - Tangenziale di Napoli is an urban highway that connects the various districts of Naples (southern Italy), through fourteen interchanges, avoiding the streets of city center. On the one hand it connects with the city's airport and several major highway backbones to the north and the rest of southern Italy, and on the other with the suburban area of the Campi Flegrei and Litorale Domitio. Its construction began in 1968, and in 1972 a first part was opened to the public; however, it was not until 1992 that it was opened in its full (current) configuration. The length of the highway is about 22 km (from Capodichino Airport to the end of Campi Flegrei, not including the length of the interchanges) and the design capacity was eighty thousand vehicles per day; however, the actual traffic in 2019 was about three times the design capacity. It is currently operated by Tangenziale di Napoli S.p.A., a company belonging to the national group of highway operators, Autostrade per l'Italia S.p.A. The highway has uncontrolled access and toll booths at each exit junction. There are eight toll classes based on the number of axles per vehicle. A point-to-point speed control system is in place (Cascetta et al., 2011). The A56 highway has three lanes in each direction. It has about 2 km of tunnels and, most importantly, multi-span bridges with a total length of more than 3 km (excluding viaducts at interchanges). The viaducts are of various structural types, with the predominance of single-supported prestressed concrete spans. However, continuous beams and steel-concrete composite structures are also present. The network cannot accommodate special vehicles larger than those that can circulate freely on the Italian highway system, due to the size of the toll booths.

4.1.1. A56 Bridges: Miano Agnano, Calata San Domenico and Arena Sant'Antonio

Three viaducts along the network were selected as benchmarks for calculating the effects of simulated traffic loads in terms of structural demand, namely the Miano-Agnano (No. 1), Arena Sant'Antonio (No. 2) and Calata San Domenico (No. 3) viaducts, whose locations along the road network are shown in the map in.



Figure 62 – Location of case studies on the A56 – Tangenziale di Napoli

The three viaducts are characterized by twin superstructures, one in each direction, mostly consisting of consecutive spans simply supported and one-or-two reinforced concrete piers with cap beams.

The superstructure of the Miano Agnano and Arena Sant'Antonio viaducts consists of precast prestressed concrete beams, post-tensioned with spans between supports of 35.5 m for the former and pretensioned with typical spans of 40.0 m (23.0 m for the end spans) for the latter, joined together by cast-in-place reinforced concrete deck slabs and transverse beams—a structural system that has seen widespread use in Italy since the 1960s (Menn, 1990). In both cases, a typical span includes four precast beams, with a span-to-depth (slenderness) ratio of about 14.

The following study considered a limited number of spans of each bridge, highlighted as red boxes in Figure 63. In fact, since the superstructures have two independent decks for each traffic direction, a total of three structural models are required.

(a) Viaduct no. 1



(b) Viaduct no. 2



(c) Viaduct no. 3



Figure 63 – Cases study: (a) Miano Agnano, (b) Arena Sant’Antonio, (c) Calata San Domenico viaducts

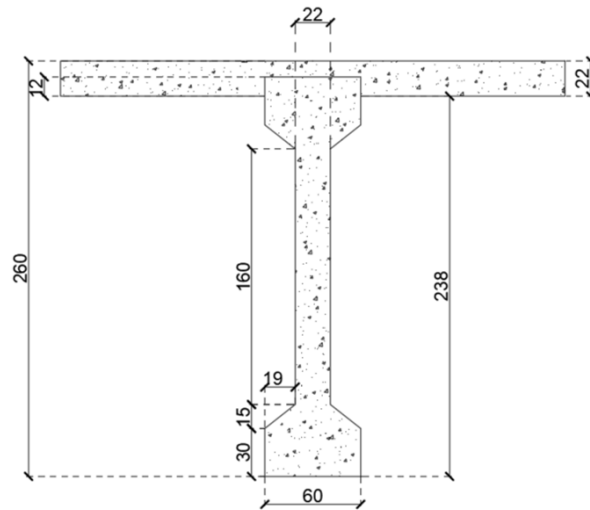
For each viaduct case study, the structural behavior of a representative segment was modeled using one-dimensional finite element models. The basic assumption of these models is that the materials constituting the structural members remain within the linear elastic range under the loading conditions considered here and the inertial effects of load application can be neglected. Material properties for each viaduct were obtained from a series of in situ and laboratory tests commissioned by the network operator.

In the case of viaducts Nos. 1 and 2, the superstructure was modeled using a grid of flat girders because the open cross-section (see Figure 66) beam-slab is potentially subject to transverse bending deformations, and the model also took into account the flexural

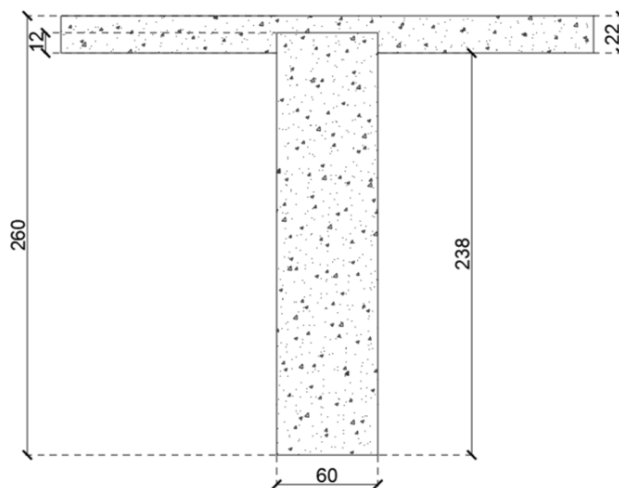
stiffness of the cap beams because the effect of these on the distribution of bending moment between beams may be nonnegligible.

When the primary longitudinal beams are prestressed and the transverse partitioning is provided by simply braced deck beam and slab elements, the literature generally considers flat grid models to be a good compromise between relatively simple numerical modeling and a realistic representation of transverse stiffness, since the latter may be affected by some limited cracking under service conditions.

The span of viaduct 1 has a length of 38.50 m with 4 beams of height 2.40 m. The beams are placed with 3.30 m spacing and present a variable cross-section along the longitudinal development. In fact, in the middle section they have an I-section with area equal to 13.974 cm^2 (see Figure 64a), while in the abutment they have a rectangular section (see Figure 64b). There are 4 rectangular crosspieces of 0.25 m thickness, 2 of which are at the end and 2 placed 3.60 m from the middle section of beams. Also, the pulvinus has a variable cross-section (see Figure 64c) and the connection between beams and pulvinus is performed by rigid links.



(a)



(b)

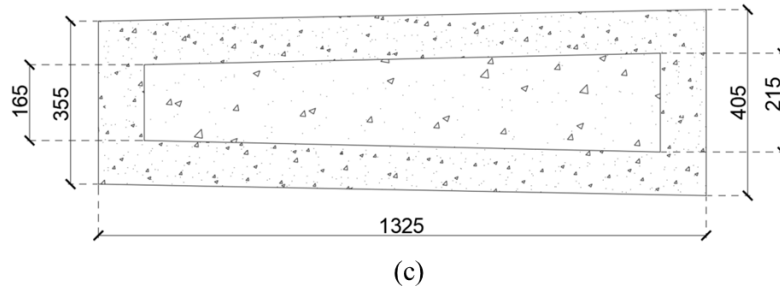
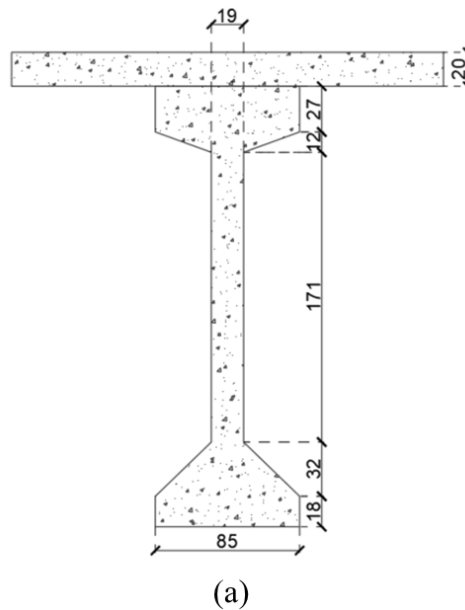
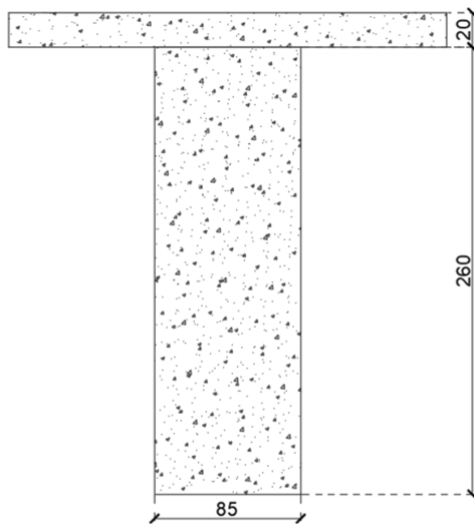


Figure 64 – Miano Agnano: (a) middle section of beam, (b) beam’s section at the support, (c) top view of pulvinus - dimensions in cm

The span of Viaduct 2 has a length of 23,00 m and it consists of 4 beams arranged with 3.25-m spacing with variable section of dissymmetrical double-T type at the middle section and rectangular at the bearing section (see Figure 65). Again, there are 4 rectangular crosspieces of 0.30m thickness of which 2 are at the end and 2 are placed about 7.50m from the end. Finally, the beams are supported on one side on the end abutment and on the other side on the pulvinus. The connection between beams and the pulvinus is made by rigid links, while the abutment is schematized by fixed hinge-type supports.





(b)

Figure 65 – Arena S. Antonio: (a) middle section of beam, (b) beam’s section at the support - dimensions in cm

For the Viaduct No. 3, the in-plane deformability of the cross-section of the multi-case girder was modeled using a grid of longitudinal and transverse beams, where each longitudinal frame element was assigned the flexural and torsional stiffness of each individual case. While each transverse frame element is associated the transverse flexural stiffness of the top and bottom slabs.

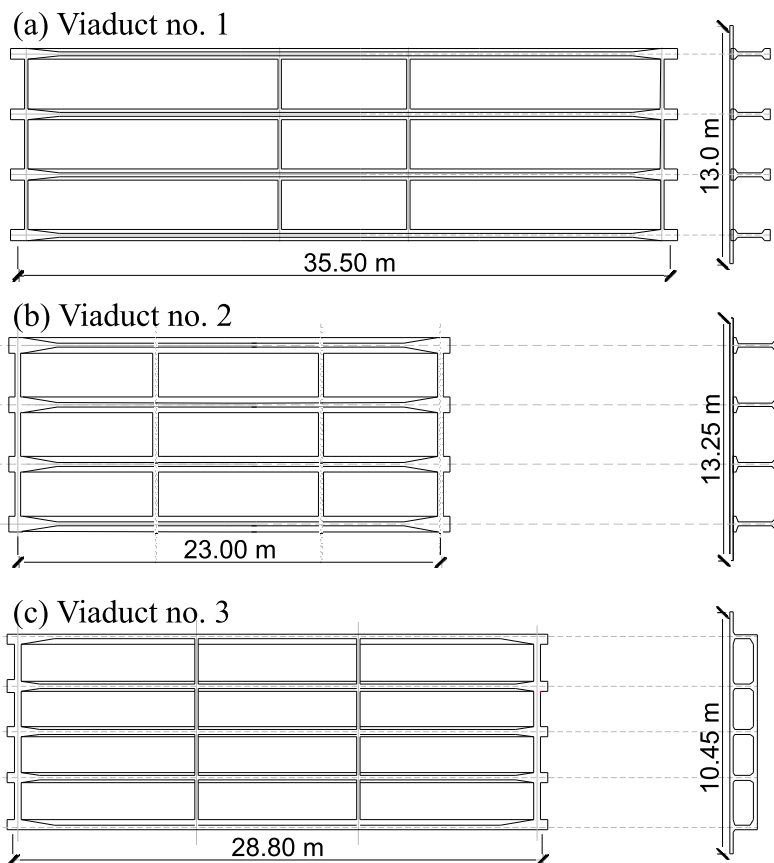
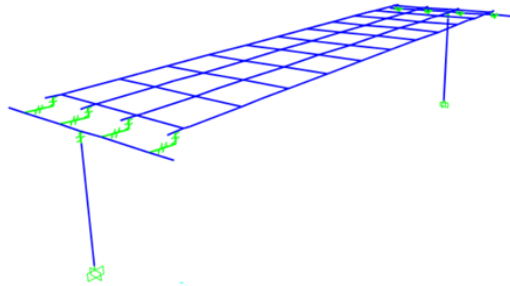
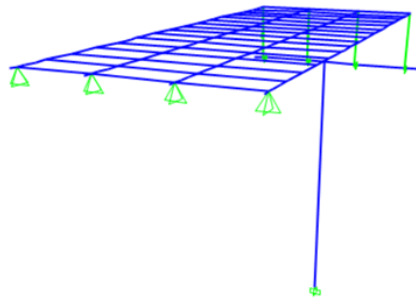


Figure 66 – Cross section: (a) Miano Agnano, (b) Arena Sant’Antonio, (c) Calata San Domenico viaducts

(a) Viaduct. No 1



(b) Viaduct. No 2



(c) Viaduct. No 3

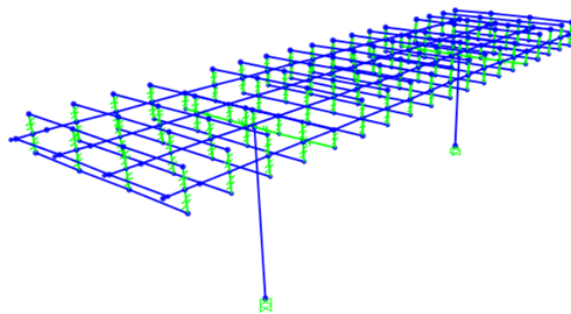


Figure 67 – FEM Model: (a) Miano Agnano, (b) Arena Sant’Antonio, (c) Calata San Domenico viaducts

4.2. Regulatory standards

Current regulations require that safety checks of existing bridges be carried out at the cross-sectional level and according to the limit state approach. This approach can be adopted through three levels of complexity, namely Level III probabilistic type, Level II simplified probabilistic type and Level I semi-probabilistic type. Regardless of the approach adopted, the achievement of a limit state (i.e., a condition where the structure no longer performs the designed performance) is defined analytically through the limit function:

$$\xi(X_1, X_2, \dots, X_n) \rightarrow \text{if } \xi < 0 \text{ the structure is unsafe; otherwise, if } \xi \geq 0 \text{ it is safe} \quad 34$$

where X_1, X_2, \dots, X_n are the random variables involved in defining ξ - namely safety margin - as material properties, effect of actions and strengths.

Then the probability of collapse can be defined as:

$$P_f = P(\xi < 0) \quad 35$$

the reliability index β descends from this probability. For further details, see (Cosenza E., Manfredi G., 2016)

Currently, existing infrastructure is verified using simple procedures based on the method of partial factors of safety (Level I), i.e., by comparing the effects induced by external actions, such as permanent and traffic loads amplified by partial factors of safety, with the corresponding load-bearing capacity calculated from the mechanical properties of the constituent materials. This comparison can be expressed through Eq. 36 where E_d represents the design structural demand and R_d the capacity i.e., the nominal design strength of the cross-section.

$$E_d = \gamma_{G1} \cdot G_1 + \gamma_{G2} \cdot G_2 + \gamma_Q \cdot Q_k \leq R_d \quad 36$$

G_1 and G_2 represent the stresses caused by the effect of structural and nonstructural permanent loads, respectively, and Q_k those due to traffic loads. The partial safety factors, on the other hand, are given as $\gamma_{G1}, \gamma_{G2}, \gamma_Q$ for each type of action, respectively. The operational safety margin of the structure ξ can be conventionally quantified as the distance between capacity R_d and demand E_d .

G_1 and G_2 are calculated on the basis of the nominal densities of materials prescribed by the code, in combination with the design geometry of the structure. Conversely, the characteristic value of the traffic effects – that is the value with exceedance return period of 1000 years on average - is generally obtained by conventional loading schemes prescribed by the code. These schemes consist of a combination of point and distributed forces that can be considered as traveling on the superstructure along the axis of the bridge.

The load schemes according to American (AASHTO, 2020; ASCE/SEI 7 -22, 2022) and Italian standards (EN 1991 - 2, 2003) (hereafter referred to as NTC2018) must also be arranged according to conventional lanes, the number of which is a function of the width of the bridge carriageway surface (w) as shown in Table 27.

Table 27 – Conventional lanes according to NTC2018

Width of driveway area (w)	Number of conventional lanes	Convention lane width (m)	Width of the remaining area (m)
$w < 5.40 \text{ m}$	1	3.00	$(w - 3.00 \text{ m})$
$5.40 \text{ m} \leq w < 6.00 \text{ m}$	2	$w/2$	0
$6.00 \text{ m} \leq w < 6.00 \text{ m}$	$Int\left(\frac{w}{3}\right)$	3.00	$(w - 3.00 \text{ m} \cdot n)$

For bridges of Category 1 - on which heavy vehicles can cross - the standards require the adoption of a two tandem axle applied on square-shaped tire footprints (40 cm side) on three conventional lanes equal to 300 kN on the first, 200 kN on the second and 100 kN on the third, respectively. In addition, there is a uniformly distributed load of 9 kN/m² on the first lane and 2.5 kN/m² on the remaining. Figure 68 shows the summary scheme with reference to the conventional first lane. With this, the characteristic value of the stress should be calculated by arranging the conventional traffic load model in the most unfavorable arrangement for that specific action.

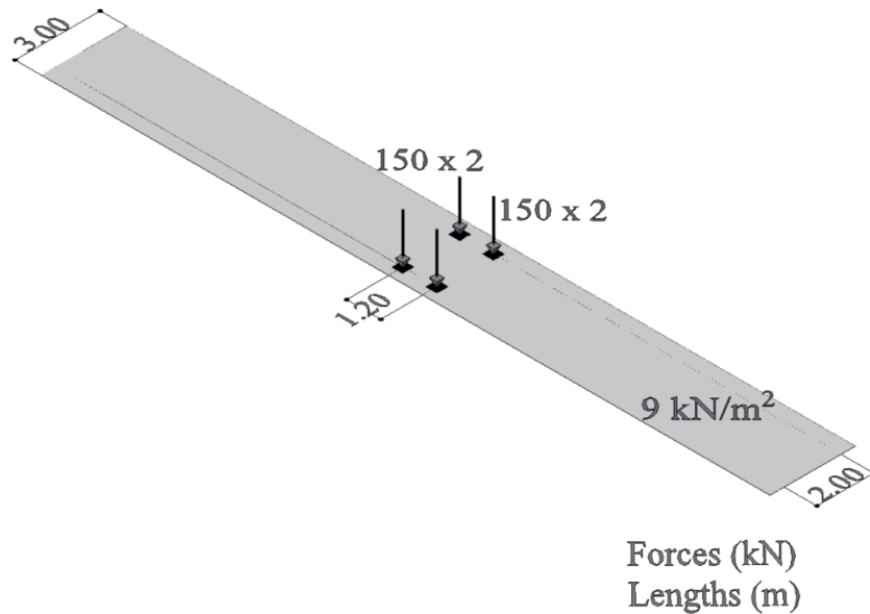


Figure 68 – Schema di carico 1 previsto dalle NTC2018 in riferimento alla prima corsia convenzionale di carico.

Recently, the emerging need to check the safety of aging road infrastructure in Europe and elsewhere has highlighted that most of existing bridges may not meet regulatory reliability requirements for new structures (adequacy condition). In addition, some structures need to remain open to traffic.

For this reason, DM2020 guidelines (CS.LL.PP., 2020) introduce partial safety factors and alternative traffic load models to be used in the decision-making process to determine whether a bridge can remain operational (open to traffic until the bridge is retrofitted) or passable (open to traffic with restrictions). Therefore, to facilitate the adoption of traffic limitations in terms of maximum weight of passing vehicles, these load models involve vehicles whose dimensions and axle loads correspond to specific weight limitation thresholds.

Specifically, DM2020 provides for the classification of existing bridges according to three states: (i) adequate bridge when safety checks are met with the standard load models; (ii) operational bridge when reduced partial safety factors are adopted with the standard load model; and (iii) transitable bridge when the safety checks are met using the load schemes shown below.

Figure 69 and Figure 70 show the load scheme used to determine whether a bridge can be opened to heavy traffic; the vehicle weight threshold to be imposed is 440 kN (equal to the sum of the indicated point loads) in the former case and 260 kN in the latter. Unlike the Eurocodes, DM2020 does not associate a specific exceedance return period with the actions produced on bridges by this alternative loading model. Not only that, but the partial safety factors prescribed for the safety verification of Equation 36 also differ between the two cases of standardized and transitable bridges. These factors are listed in Table 28. Table 28 shows the values of the partial safety factors provided by DM2020 and NTC2018 respectively.

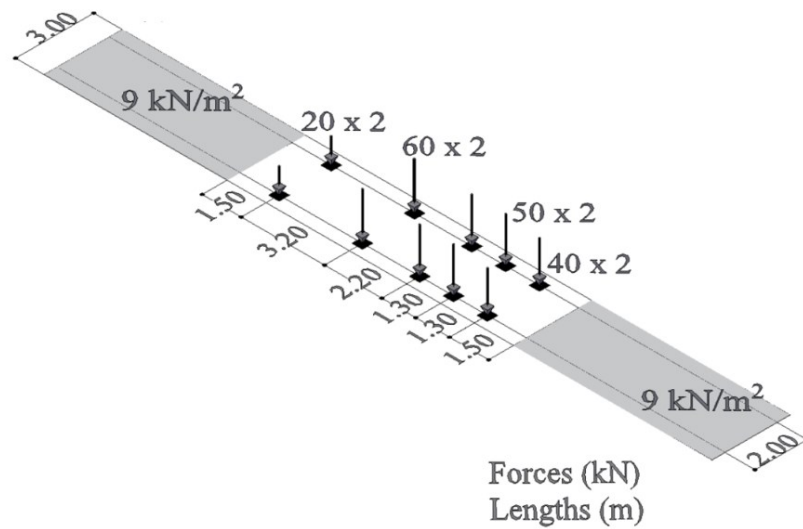


Figure 69 – Load scheme with 440 kN, DM2020

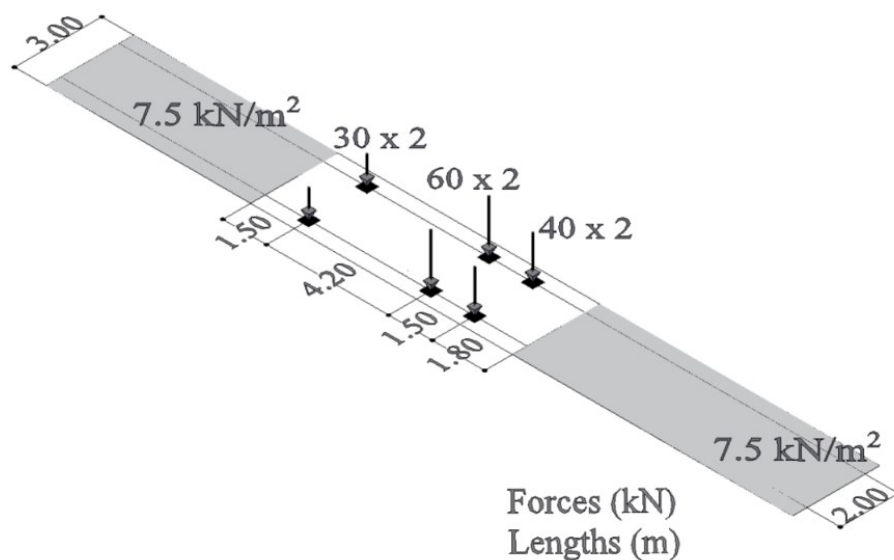


Figure 70 – Load scheme with 260 kN, DM2020

Table 28 – Partial safety factors provided by DM2020 and NTC2018

			γ_{Qk}
NTC2018	$G_{1k} - G_{2k}$	-	1.35
	Q_k	-	1.50
DM2020	$G_{1k} - G_{2k}$	ADEGUATEZZA	1.35
		OPERATIVITA'	1.26
		TRANSITABILITA'	1.26
	Q_k	ADEGUATEZZA	1.50
		OPERATIVITA'	1.20
		TRANSITABILITA'	1.60

4.3. Traffic Model

Microscopic traffic simulation is used to propagate traffic demand on the highway network and to calculate the dynamic configuration of structural loads. Traffic simulations aim to estimate a probabilistic model of hourly O/D demand flows for a reference period of one year. This required one year of survey data acquired from the network operator. The data consisted of detector counts at all exit intersections (from toll booths), in addition to upstream counts from the point-to-point (P2P) speed control system (Cascetta et al., 2011).

Once an annual sample of this distribution is propagated through the network, the simulated traffic shares the same statistical characterization as the measured traffic data (i.e., 2018 counts) from which the O/D demand model was estimated.

To simulate an entire year, 365 simulations were run, each lasting 24 hours. This approach was chosen because the state of the network, in terms of traffic, at the initial instant of the simulation, t_0 , must be known to reproduce the traffic evolution over time $t > t_0$.

Since the initial microscopic traffic state - which consists of the location, speed, route, and destination of each vehicle in the network at t_0 - is almost never observed or estimated, the only accurate solution to the initial state problem is to run a simulation of the entire day. In this case, a near-empty initial state condition of the network can be assumed starting the simulation at night.

Regarding the input demand, an interval of one hour was considered suitable to reproduce the traffic dynamics on the network with adequate resolution for the purpose of this analysis. Therefore, 365 daily series of 24 origin-destination flow matrices were estimated, for a total of 8760 hourly matrices.

For this purpose, the network operator made available hourly traffic counts-including those of all highway exit sections-for an entire year (i.e., 2018). Specifically, the O/D matrices provide travel demand in terms of the total number of vehicles coming from a specific origin and moving to a specific destination on the network, in a specific one-hour interval.

The statistical characteristics underlying the estimation problem were identified as (i) the inter-day variability of link flows, measured by their coefficient of variation (CoV), and (ii) the intra-day correlation of link flows, measured by the Pearson correlation coefficient (PCC) (Punzo et al., 2014). By applying the measured CoV and PCC to a small number of baseline O/D matrices, hourly matrices of all days in a year were estimated.

4.3.1. Cluster Analysis

A preliminary analysis of the flows showed that the annual data can be divided into four groups, depending on when data are collected that is during the summer or winter months and during working or nonworking days, such as weekends.

Traffic flow data are used in a cluster analysis to identify typical days in one year, i.e., days having similar O/D matrices' characteristics. After that the clusters are identified and the typical days are defined, a second-level cluster analysis is performed in order to identify hourly clustering and, so, to detect the hours of a day with similar characteristics. For this analysis, two representative points of the network were identified, namely the Corso Malta and Fuorigrotta exits (exit interchanges). Then a k-medoids algorithm (Mannor et al., 2011; Arora et al., 2016) was applied to pairs of hourly traffic flows at the two locations, with different cluster numbers. The results of the algorithm for the

case of four clusters are shown in Figure 71. In this figure, the points belonging to the same cluster are shown with same color (red, green, cyan and purple for clusters 1 to 4) and the centroid of each cluster is marked with a yellow cross. The number of clusters adopted (four) was the best compromise found by the k-medoids algorithm to group the data. As expected, the clusters identified correspond to specific time slots of a day. However, the clusters do not correspond to the same time slots in the transition from one period to another. As an example, in reference to weekdays with school, the purple dots correspond to the 6 a.m.-10 p.m. time slot, the cyan dots correspond to the 10 a.m.-9 p.m. time slot, green is representative of the 9 p.m.-12 p.m. slot, and red corresponds to the 12 p.m.-6 a.m. slot.

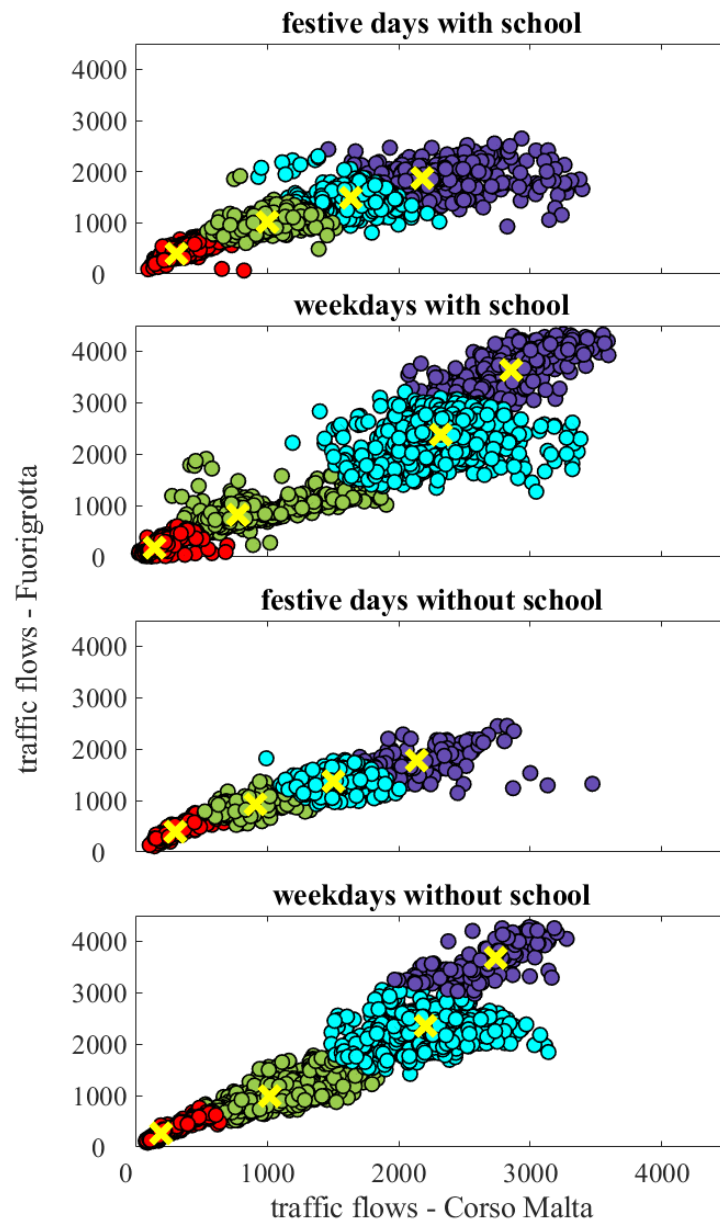


Figure 71 – Cluster analysis

Since the found clusters are not scattered, it was assumed that for each time slot: (i) the spatial structure of the O/D flow is invariant within a time slot (i.e., given a period, all hours in a time slot share the same spatial structure of the O/D flow) and (ii) the common

spatial O/D structure is estimated for the cluster centroid (i.e., using the observed traffic counts during the day and hour corresponding to the centroid).

For each period and each cluster centroid, an O/D matrix was estimated using a generalized least squares estimator (Cascetta et al., 2011), combining information from observed link flows with a-priori estimates of O/D matrices available from previous network operator planning studies. As a result, sixteen hourly base case O/D matrices (four clusters per period) were estimated. In turn, these matrices were used as a priori information to estimate the 24-hourly matrices of the representative day in each period. For each period, the four hourly O/D matrices estimated for the base case were used to define a typical day for that period. That typical day is characterized by a number of hourly O/D matrices per time slot, each equal to the O/D matrix of the centroid of that time slot from the cluster analysis. As mentioned above, the daily series of O/D matrices for the other days in a period were estimated by considering the CoVs of the total flow of links on the network in each specific hour of the cluster and the PCC of the total flows of links in the 24 hours of the period. These two statistics were assumed to represent the daily variability of O/D flows and the within-day correlation of O/D flows within a time slot. As an example, Figure 72 shows the histograms of total flows during the "weekdays with school" period (of 2018) for four the time slots (6 a.m. to 10 a.m.).

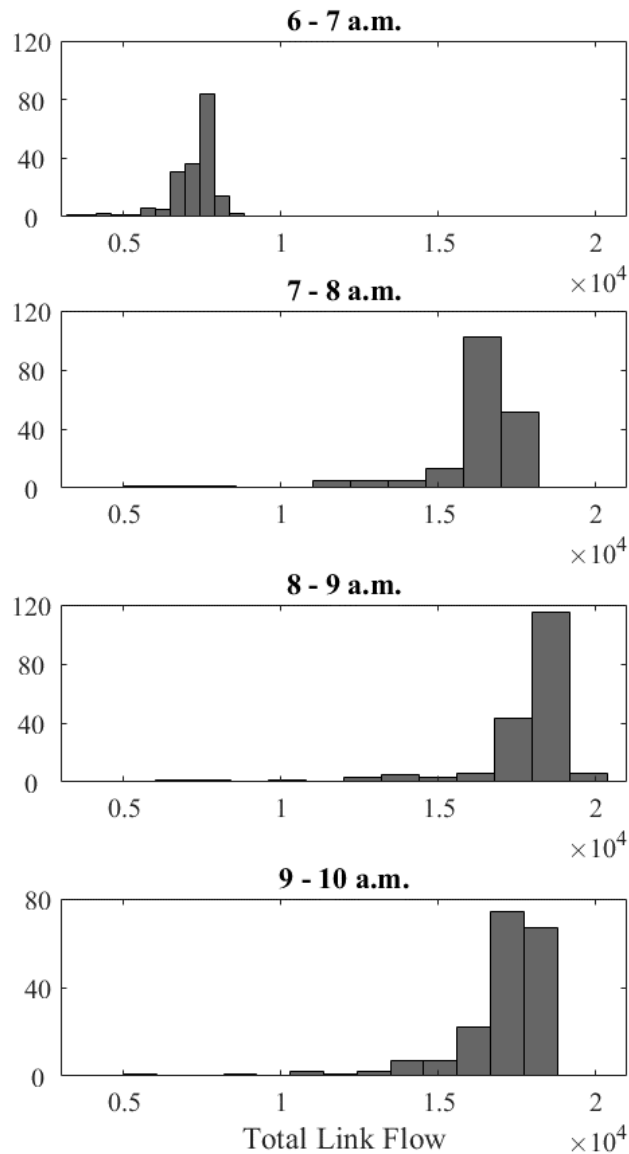


Figure 72 - Total flows for "weekdays with school" from 6 to 10 a.m.

4.3.2. Daily O/D Matrix

The PCC matrix of total flows for 24 hours referred to the weekday period with school in 2018 is shown in Figure 73, where reddish colors indicate PCCs close to unity. The figure shows that there is a high correlation between flows in the 6 to 11 a.m. as direct consequence of highly congested patterns during peak hours. In general, daytime flows are poorly correlated with nighttime ones because the two flows have completely different travel motivation patterns (i.e., a high traffic flow during a morning is not related to the nocturnal flow that could be observed).

Given a period based on typical daily matrices of CoVs of hourly total flows and correlations of flows within a day, a multivariate Gaussian copula was defined (Rafati Fard and Shariat Mohaymany, 2019).

The O/D flow copula was defined by the vector of 24 averages and 24 standard deviations of the O/D flow of each hour (where the averages were obtained from the O/D correction procedure and the standard deviations were obtained by the product

of each mean with the corresponding CoV of the total outflow from the network, in the same hour, calculated from the data), and the 24 by 24 correlation matrix of the total outflow from the network calculated from the data, which was assumed to represent the temporal correlation of the O/D flows as well. Then, the 24-hour series of O/D flows were generated from the copula for the number of days in that period via Cholesky decomposition. Repeating the same approach for each of the four periods considered yielded 365 sets of 24-hour O/D matrices, which constitute the sampled input for the one-year traffic microsimulations.

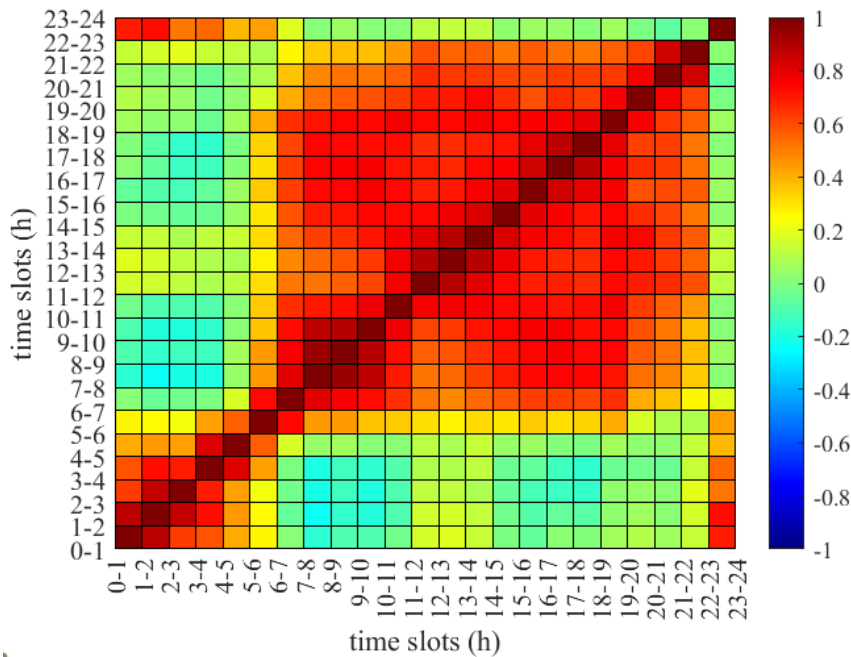


Figure 73 - PCC matrix of total flows for 24 hours, weekday period with school 2018

4.3.3. Traffic characterization

The geometric characterization of the vehicles running on the infrastructure is necessary to fully define the traffic model. To take into account the heterogeneity of vehicles, a multiclass traffic model was developed, in which each vehicle class has a specific set of parameters.

On the one hand, the network operator has provided four macro-classes based on toll classes (denoted by the numbers II, III, IV and V), depending on the number of axles, from two to five. On the other hand, according to the Italian highway regulations (D.Lgs n.285/1992, 1992), sixteen vehicle subclasses have been defined to also consider the variability of vehicle geometry (i.e., position of axles) within each toll class, so that the structural load of each vehicle can be properly evaluated. Table 29 shows the toll classes and additional subclasses considered.

Table 29 – Vehicle classification

Toll Class	Type	ID	L	L ₁	L ₂	L ₃	L ₄	L ₅
	-	-	m	m	m	m	m	m
II	Car < 4.5m	car1	3.75	0.70	2.40	-	-	-

	Car \geq 4.5m	car2	4.60	0.90	2.80	-	-	-
	truck	A2	8.40	1.30	6.00	-	-	-
	Bus	B2	10.70	2.40	5.40	-	-	-
	Van	VAN	4.85	0.90	3.10	-	-	-
III	truck	A3	9.85	1.40	4.80	1.40	-	-
	articulated lorry	AA3	12.50	1.40	3.70	5.90	-	-
	trailer truck	AT3	18.75	1.40	5.60	7.90	-	-
	Bus	B3	15	2.80	9.50	1.30	-	-
IV	truck	A4I	10.23	1.50	1.95	3.20	1.60	-
	truck	A4II	13.26	1.45	4.10	1.35	1.35	-
	articulated lorry	AA4	12.50	1.45	3.70	5.00	1.35	-
	trailer truck	AT4	18.75	1.40	5.60	4.85	5.80	-
V	articulated lorry	AA5I	16.50	1.45	3.40	1.30	5.90	1.30
	articulated lorry	AA5II	16.50	1.40	3.70	4.70	1.30	1.30
	trailer truck	AT5	18.75	1.40	4.80	1.35	5.00	5.45

Figure 74 shows an example of vehicle subclass geometry, defined by the total vehicle length, L , and axle distances. The lengths and distances between axles used to define the vehicle geometries for each subclass were evaluated based on data provided by vehicle manufacturers. Specifically, the average values of the available specifications were assigned to each subclass. Further details can be found in Annex A.

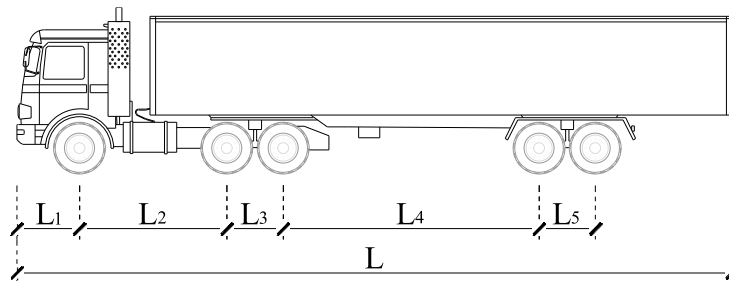


Figure 74 – Example of vehicle geometry

The road network operator provided the percentage of vehicle transits in 2018 by toll class (98.94 percent, 0.28 percent, 0.36 percent, and 0.26 percent from class II to class V, where the number corresponds to the axle number), then a further subdivision was made into each of the sixteen subclasses assuming that the distribution of vehicle types circulating on the network is the same as the vehicle fleet in the official regional database of registered vehicles (Automobile Club D'Italia, <https://www.aci.it/>). The percentage of each subclass of vehicles within the toll classes is shown in Figure 75.

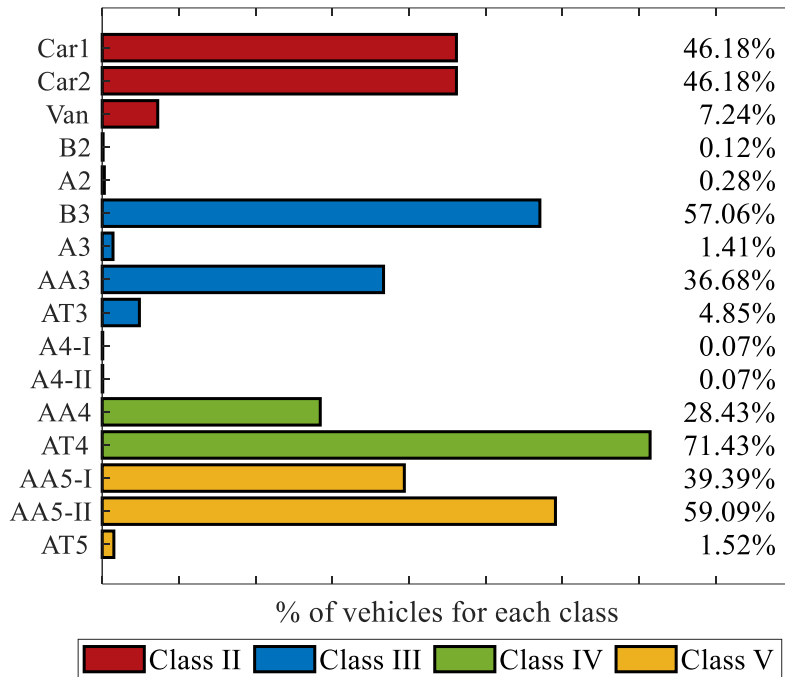


Figure 75 – Percentage of each vehicle class within the toll class

4.3.4. Calibration of vehicle behavior

The simulation model (implemented in Aimsun, <https://www.aimsun.com/>) required a minimization of differences between observed and simulated lane flows.

Simulation-based calibration was performed according to the methodology described in the literature (Ciuffo et al., 2008). The calibration procedure uses an OptQuest/Multistart heuristic (Ugray et al., 2005), to search for values of continuous and discrete parameter sets, denoted β and γ , respectively, that satisfy an optimization function:

$$\{\beta, \gamma\} = \underset{\beta, \gamma}{\operatorname{argmin}} \{ \operatorname{RMSE} [M^{obs}, M^{sim}(x_1, x_2, \dots, x_h, \beta, \gamma)] \} \quad 37$$

where RMSE, is the root mean square error between the observed M^{obs} and simulated M^{sim} sets of traffic measurements. Finally, x_1, x_2, \dots, x_h are the O/D fluxes of the time interval h . Note that the parameters to be found are constrained to be within the assigned limits.

The optimization problem in equation 37 was applied sequentially to different parameters using different sets of measurements. First, the mean and standard deviation of service rates at exit toll booths were calibrated. Peak hour exit flows at the Corso Malta toll booths were considered, since vehicle queues feed these toll booths continuously during peak hours (i.e., a period when the toll booths operate at full capacity, and thus the resulting exit times depend only on the toll booth service rates). Indeed, accurate calibration of toll booth capacity is critical to realistically reproduce the spillover of queues from the exit ramp to the highway that occurs daily at the Corso Malta exit junction.

A calibration of the ramp exit model parameters was performed to qualitatively reproduce the specific behavior of vehicles at that critical ramp exit node. Desired speeds, maximum acceleration and deceleration rates, reaction times, and speed acceptance (a parameter representing a vehicle's level of compliance with the speed limit) for light vehicle (LD) classes (i.e., cars and VANS) and heavy vehicle (HD) classes

(i.e., buses, trucks, and lorries) were calibrated by solving equation 37 using highway lane flows-available from the P2P speed control system; see (Cascetta et al., 2011). For a discussion of the Gipps model, which is the car-following model applied in Aimsun, its parameters and corresponding constraints, see (Ciuffo et al., 2012; Punzo et al., 2012). Note that all HD vehicle classes share the same parameter values. Finally, further refinement of the toll booth service rate parameters was made to account for the variation in calibrated toll booth flows (at capacity) due to the calibration of the car-following model parameters. Table 30 – shows the vehicle acceleration (a), normal deceleration (b_n) and maximum deceleration (b_m) i.e., deceleration under normal traffic conditions and under dangerous situations. In addition, the calibrated parameters for the reaction time for a stimulus RT , to the stop RT_1 , or to the barrier RT_2 , are listed. In addition, the calibrated value for the speed acceptance parameter for HD vehicles was 0.83 (0.85 for A2 trucks) and for LD vehicles was 0.91 (0.86 for buses).

Table 30 – Behavioral parameters of vehicles

Veh.	a	b_n	b_m	RT	RT_1	RT_2
-	m/s ²	m/s ²	m/s ²	s	s	s
LD	3.00	4.00	6.00	0.40	0.80	0.80
HD	2.50	3.00	6.00	0.90	1.60	1.60

4.3.5. Traffic microsimulation

The traffic simulation provides information regarding vehicle flow, density, and average speed, at some predetermined locations along the simulated network. Since the default output of the software is not exhaustive for research purposes, additional information was extracted through an application programming interface. In fact, the simulation output data required for this study include vehicle trajectories, i.e., the position and speed of each vehicle (characterized by a unique ID, class, length, and width), recorded at a sampling rate of 10 Hz.

As an example of the simulation results, Figure 76 shows two traffic snapshots on a road segment, one corresponding to congested traffic conditions and another showing a free traffic situation. In addition to the vehicle trajectories, other two information are needed to obtain the load configurations: (i) the geometry and (ii) the weight of each vehicle. From this, the axle positions of each vehicle and their forces on the deck are derived.

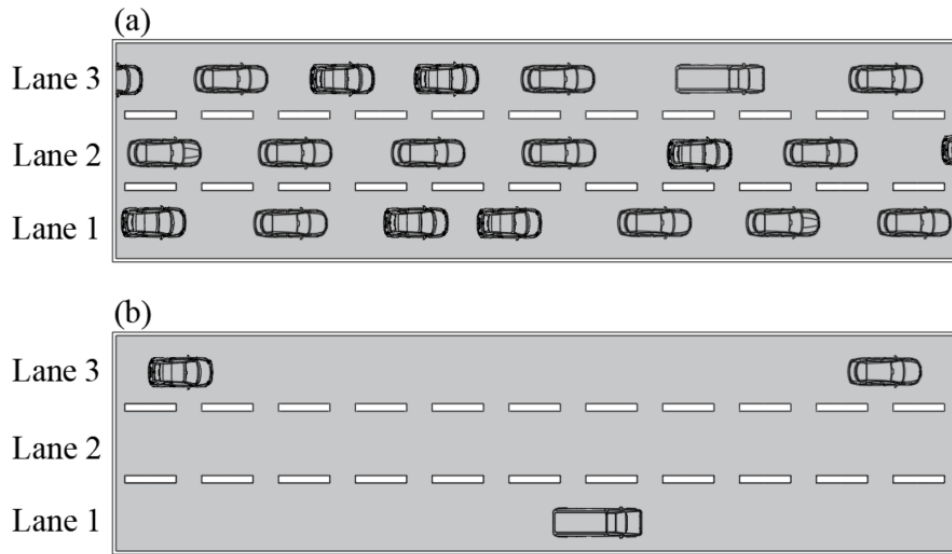


Figure 76 - Simulated trajectories: (a) congested condition and (b) free flow condition

4.4. Annual distributions of maximum stresses

In this section, the methodology required to derive the load configurations on the three bridges and the obtained results about the annual maximum stress distributions are described. For these distributions, it is necessary to define (i) the assignment of a total weight to each vehicle, (ii) the axle distribution, and (iii) the definition of the load configurations from the results of the micro-simulations.

4.4.1. Vehicle weight and axial forces

For the subclasses of cars and vans, deterministic weight values were attributed from manufacturer specifications (ANFIA, <https://www.anfia.it/>), while for the subclasses of buses, trucks, and lorries, weight attribution was based on empirical distributions (Lu et al., 2002). More specifically, this study provides data on truck traffic collected from 1991 to early 2001 from the WIM system of the highway network of the State of California in the United States. The report aimed to represent axle load frequency distributions for various axle groups within all types of trucks traveling on the highway network. Although the study provides a breakdown of the data by collection period (day/night), seasonal weather conditions, and geographic location of the monitored sections within the road network, only the frequency distributions of axle load by year provided for each truck type are considered here. Figure 77 shows the empirical weight distributions considered. In the figure, these distributions are plotted for eight vehicle categories, labeled using the nomenclature from the original study. These categories correspond to very light vehicles (C5 in gray), vehicles whose weight is between 100 and 200 kN (C4, C6 and C8 in black), vehicles whose weight is between 200 and 400 kN (C10 and C11 in blue) and vehicles within the same range characterized by bimodal weight distributions (C9 and C12 in red).

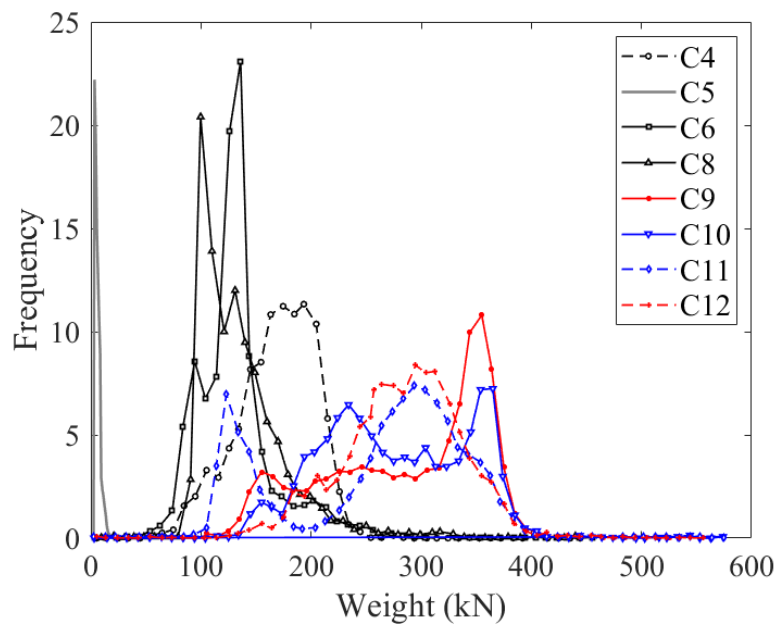


Figure 77 - Frequency distributions of marginal load by year

Each vehicle subclass, except for cars or vans, was assigned one of these empirical annual weight distributions, as shown in Table 31. Then, a total weight value was assigned to each vehicle of the simulation by sampling the associated distribution.

Once the weight of each vehicle was obtained, its distribution among the axles (which are of three types, S for single wheels, T2 for tandem wheels, or T3 for tridem wheels) was determined from the support reactions of simple static diagrams representing the chassis of the vehicles considered (Grakovski et al., 2020).

For example, Figure 78a shows the simply supported beam used to represent the frames of the subclasses of cars, buses (labels B2, B3 in Table 29), vans, trucks (labels A2, A3 in Table 29) and trailer trucks (labels AT3, AT4, AT5 in Table 29). Figure 78b shows the static scheme associated with articulated lorries (labels AA3, AA4, AA5_I, AA5_{II} in Table 29), which is obtained as a composition of two simply supported beams. Figure 78c shows the static scheme associated with trucks with trailers (A4_I and A4_{II}), which is a continuous beam. The vehicles are uniformly loaded, and the vehicle's own weight was included in the uniformly distributed load for simplicity. This assumption is considered acceptable because in practice the loading of vehicles is generally evenly arranged. Therefore, each beam support reaction, expressed as a fraction of the total load, represents the percentage of weight that each axle applies to the road or bridge deck as a static load. For more details, see Annex B. Table 31 summarizes the results obtained for each type of vehicle, where the last column shows the percentage of axle load. Finally, we note that the tandem axis, T2, was represented by a single support reaction, because the distance between the axles is less than a discretization length along the road fixed to 1.50 m. Similarly, the tridem axes are represented by two equal reactions.

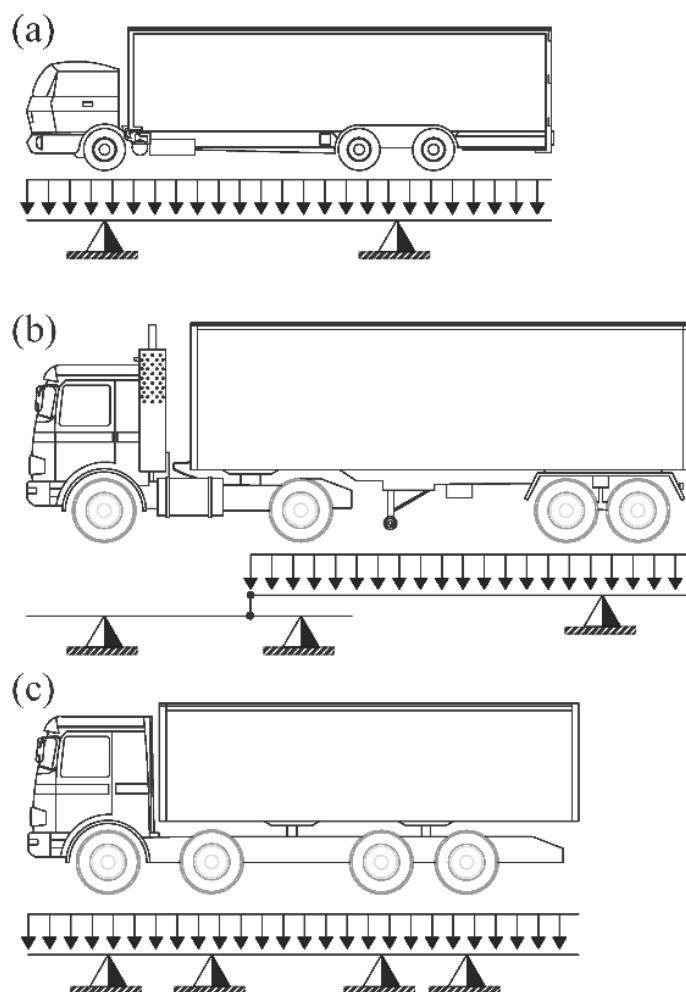


Figure 78 – Static schemes

Table 31 – Percentages of total weight distribution for each axis

Veh ID	No. of axles	Axle type(s)	Dist.	Load % per axle
A2	2	S+S	C5	51; 49
B2	2	S+S	C4	46; 54
A3	3	S+T2	C6	37; 63
B3	3	S+T2	C4	47; 53
AA3	3	S+S+S	C8	38; 18; 44
AT3	3	S+S+S	C11	20; 36; 44
A4 (I)	4	S+S+S+S	C8	26; 24; 13; 37
A4 (II)	4	S+T3	C8	24; 38; 38
AA4	4	S+S+T2	C8	36; 13; 51
AT4	4	S+S+S+S	C11	21; 29; 31; 19
AA5 (I)	5	S+T2+T2	C9	22; 22; 56
AA5 (II)	5	S+S+T3	C10	25; 5; 35; 35
AT5	5	S+T2+S+S	C12	19; 33; 16; 32
A = truck			S = single axle	

B = bus	T2 = tandem
AA = articulated lorry	T3 = tridem
AT = trailer truck	

4.4.2. Traffic load schemes

The traffic micro-simulations return the position of each vehicle for each predetermined time step (in the specific case every 0.1 sec). To obtain the vehicle positions along the bridge deck, the bridge deck was discretized into 1.5 m x 3.0 m cells, and each cell can be loaded by a single vehicle axis at a time. Figure 79 shows, as an example, two vehicle configurations recorded on Viaduct No. 1 at a given instant of time on a school weekday, while Figure 80 shows the two axle force configurations corresponding to the traffic snapshots in Figure 79. From these traffic load configurations, the corresponding internal forces to which the bridge is subjected can be calculated using the FE models described above, at least under the simplifying assumption of considering only the static effect of gravity loading, neglecting the inertial effects due to vehicle acceleration/deceleration.

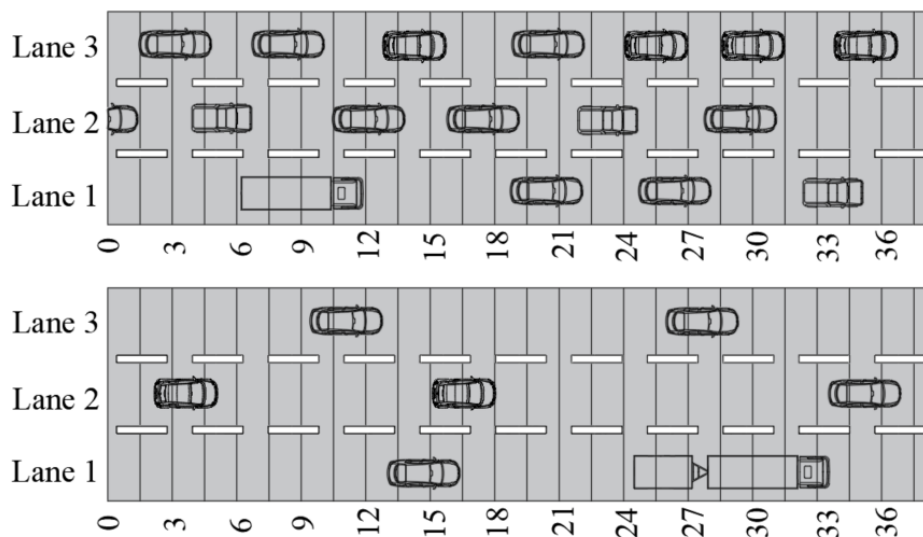


Figure 79 – Spatial distribution of axis

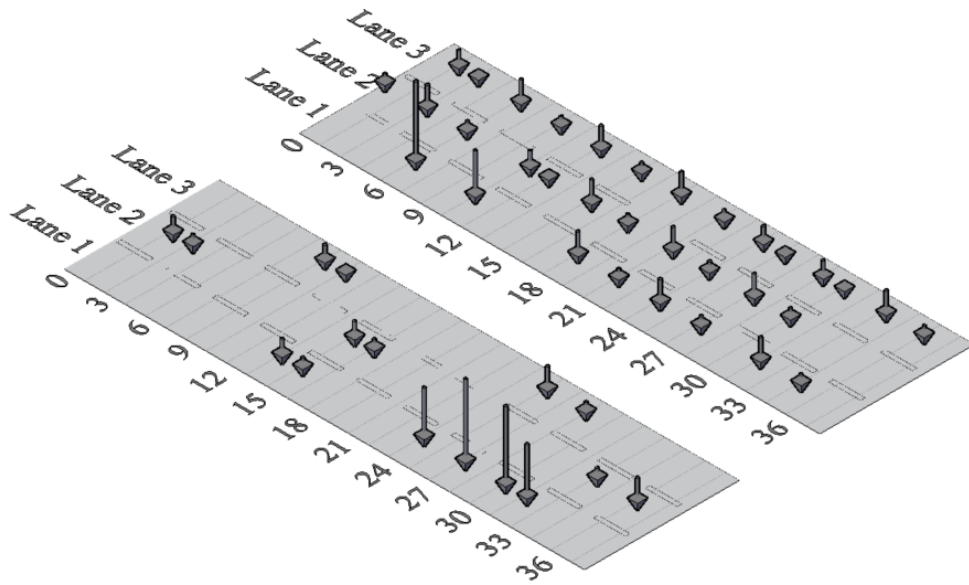


Figure 80 – Spatial distribution of forces

4.4.3. Results

In the representative spans of the examined viaducts, the critical stresses governing the capacity of the structures are the bending moments in the middle section of the prestressed concrete longitudinal beams and the shear forces of the same beams near their supports. Following the procedure described in the previous paragraph, for each simulated traffic time-step, the corresponding arrangement of loads on the superstructure is assigned and, finally, the bending moments and shear forces at the reference cross-sections are obtained using the FE models. From these results, the largest (absolute) value of each internal forces can be determined for each simulated traffic day.

For each of the four typical days, the simulated daily maxima are considered as realizations of four random variables Q_j for $j = 1, \dots, 4$, which follow extreme value distributions (EVs) of type II (Benjamin and Cornell, 2014). Figure 81 and Figure 82 show histograms of the daily maxima moment and shear respectively, for each of the 4 type days. The EV distribution well approximates all shown histograms. Therefore, the cumulative distribution for the j -th typical day is given by 38:

$$P[Q_j \leq q] = e^{-\left(\frac{u_j}{q}\right)^{k_j}} \quad 38$$

where u_j and k_j are parameters of the distribution. For generic day type j , the parameters are estimated by matching the first and second moments of the distribution with those of the simulated daily maxima.

For all four typical days, and for each bridge, the values are shown in Table 32 .

Table 32 - Parameters of the distributions for moment (M) and Shear (V) for each typical day

	<i>M</i>		<i>V</i>	
	k_j	u_j	k_j	u_j
<i>Weekend days with school</i>	12.49	1639.1	13.81	181.16
<i>Weekdays with school</i>	13.96	1672.3	14.02	185.16
<i>Weekend days without school</i>	11.82	1604.2	14.13	179.60
<i>Weekdays without school</i>	14.62	1679.4	13.43	182.04

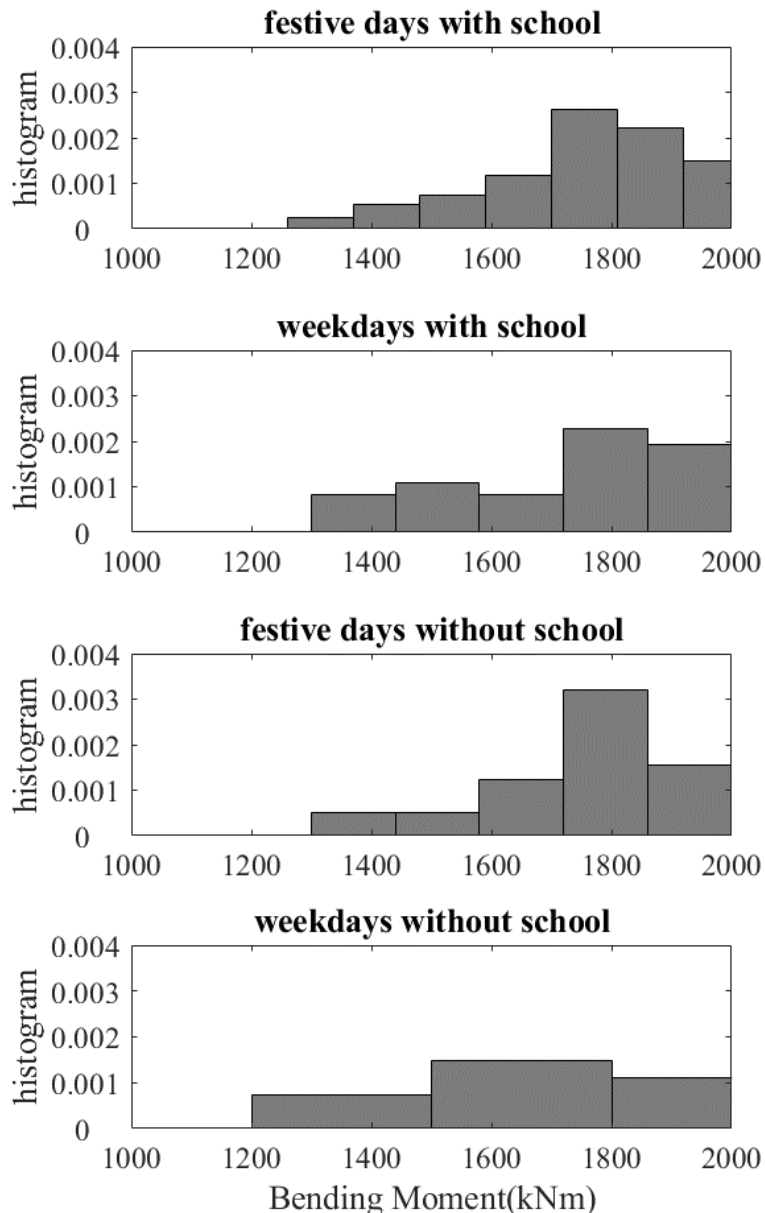


Figure 81 – Distribution of Maximum Daily Bending Moment at the middle section

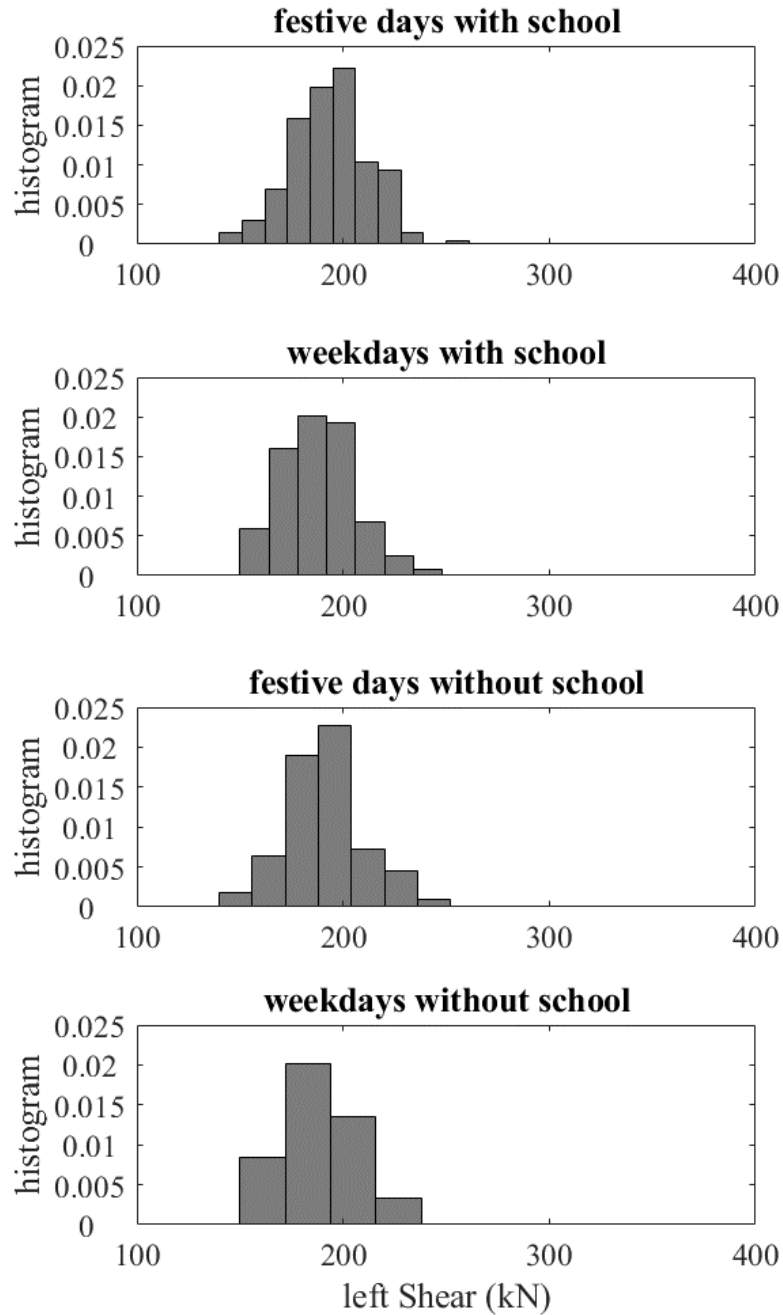


Figure 82 – Distribution of Maximum Daily Shear at the support

After applying the EV model to the data of each typical day, the probability distribution of the maximum annual traffic-induced action on the primary beams of each viaduct, Q^* , was assessed by assuming independence among the four clusters of typical days and among the traffic demands on each day of the clusters; Therefore, it can be derived by equation 39. **L'origine riferimento non è stata trovata.:**

$$P[Q^* \leq q] = \prod_{j=1}^4 P[Q_j \leq q]^{n_j} \quad 39$$

where n_j is the number of days in a year for the j -th typical day and $P[Q^* \leq q]$ is the cumulative distribution for that day. This result can be used to calculate the upper tenth percentile of the maximum annual distribution, $q_{0.1\%}$, that is, the value of the stress for which $P[Q^* > q_{0.1\%}] = 0.001$. This percentile value represents actions with a return period of 1000 years, the same as the characteristic value Q_k required by the code.

First, results are shown comparing only traffic-induced actions, i.e., structural and nonstructural permanent loads are not considered. Figure 83 shows the distribution of the maximum annual bending moment in the middle section due to traffic loading, for each viaduct. The vertical lines on the figure represent some noteworthy values. In particular, the percentile $q_{0.1\%}$ is indicated by a blue line. The red line indicates the maximum bending moment value obtained from the simulation loading schemes. The distances between the blue and red lines thus provide an indication of the large extrapolation to obtain the percentile $q_{0.1\%}$ from a probability model. Finally, the green and black lines specify the values of the load schemes of DM2020 (440kN) and EN1991-2, respectively.

For viaducts no. 1 and no. 3, Figure 83 shows that the percentile $q_{0.1\%}$ is lower than both code-compliant ones. In the figure, the return period - i.e., the time between two events that lead to a value of bending moment value greater than the predetermined one - is shown for each value of bending moment. For bridges no. 1, the return period associated with the EN1991-2 and DM2020 loading schemes is about 2000 and 100 times larger respectively, than the corresponding one associated with $q_{0.1\%}$. Similarly, for bridge no. 3, the return periods are 1000 and 100 times larger. In contrast, for Viaduct no. 2, the values of M calculated with the traffic simulation data and the DM2020 load scheme deviate by only 10%. Similarly, the return periods associated with EN1991-2 and DM2020 are about 400 and 4 times greater than the corresponding one associated with $q_{0.1\%}$. This implies that the loading schemes of EN1991-2 and DM2020 cause the rarest bending moment values.

Figure 84 provides the same information of Figure 83, only for the shear, V , at the supports of the viaduct deck. For viaducts no. 1 and no. 3, the ratios between simulated and code-prescribed actions for V are quite similar to those for M , while for viaduct no. 2, the shear calculated according to DM2020 is lower than that calculated with simulation and its estimated return period is only 69 years. This may indicate that the traffic limitation control (i.e., the weight threshold of 440kN) must be very strict for the safety of this viaduct, because the probability that, in the absence of control, the limit will be exceeded on this viaduct is higher than on the other two viaducts.

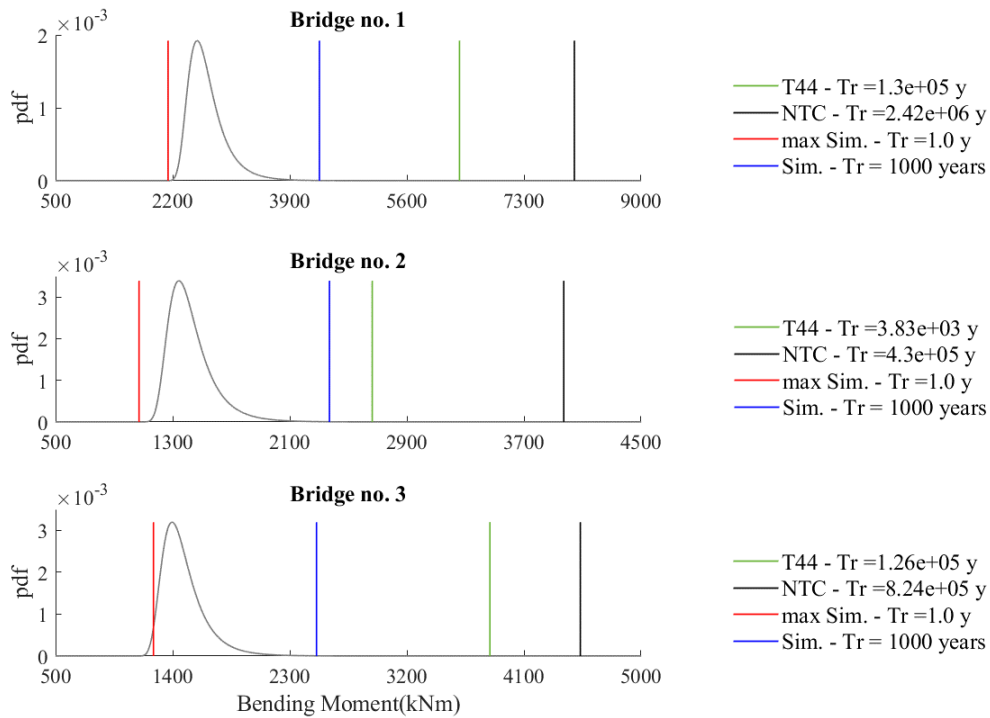


Figure 83 – Distribution of Maximum Annual Bending Moment: (1) Miano Agnano, (2) Arena Sant’Antonio, (3) Calata San Domenico

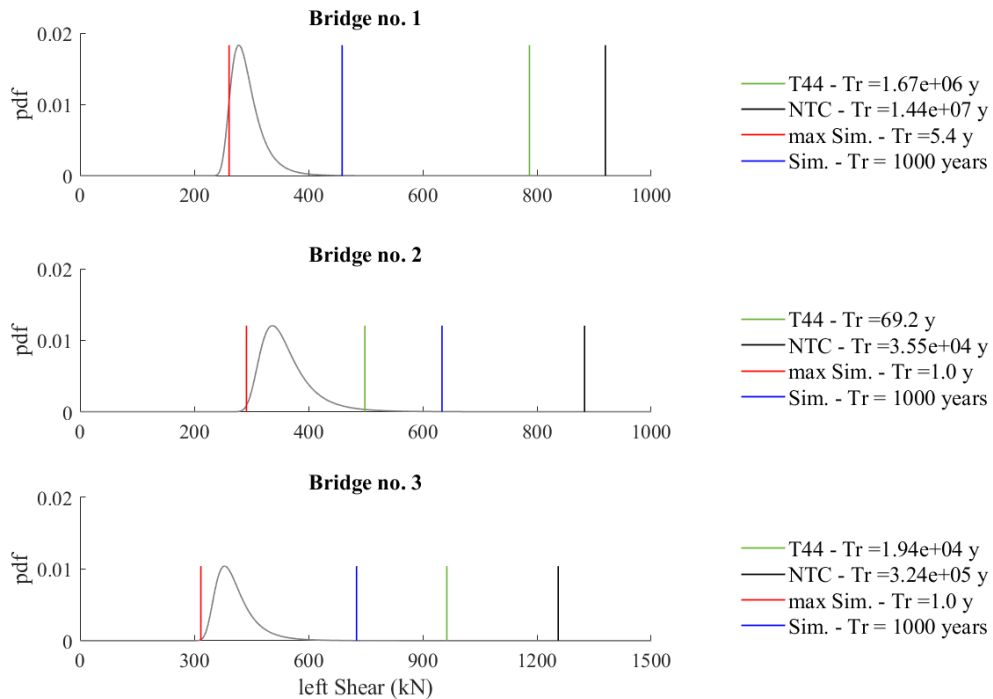


Figure 84 - Distribution of Maximum Annual Shear: (1) Miano Agnano, (2) Arena Sant’Antonio, (3) Calata San Domenico

Figures 83 and 82 present the return periods associated with the rare percentiles of the stresses obtained through the NTC2018 and DM2020 code and simulation traffic models in the legend. For these bridges, note that the return periods associated with the rare percentiles of the stresses caused by the normative loads are greater than 1000 years. In

other words, with reference to the bending moment for bridge No.1 for example, the stress value is very rare i.e., it is averaged out every $1.3 \cdot 10^5$ years.

Conventionally, however, $q_{0.1\%}$ is estimated with reference to a return period of 1000 years.

Table 33 summarizes the ratios between the $q_{0.1\%}$ percentiles from the simulations and the code specified Q_k .

If the bridges warrant the standards of the regulations - that is, the maximum stress due to the code loads is less than the respective strength – and the ratio of $q_{0.1\%}$ and the code specified Q_k is less than unity, then the bridge's level of safety is underestimated. In other words, the bridge has a higher resilience capacity than the maximum stress it could experience based on its usual load levels.

For the EN1991-2 load model, the values of these ratios vary between 0.50 and 0.72. Hence, the bridge-specific action percentiles are generally lower than their code-prescribed counterparts. In this case, the verifications conducted with the normative loading schemes are precautionary because the margin of safety achievable with the rare percentile is about 44% for bending moment and about 40% for major shear on average greater than the corresponding one achievable with the code.

For the DM2020 load model, the values range between 0.58 and 1.27.

In this case, the ratio greater than unity indicates that the margin of safety achievable with the percentile calibrated for the specific bridge is greater than the code correspondent. In fact, the maximum stress obtained with normative loads has a return period of less than 1000 years i.e., the conventional traffic-limiting load model corresponds to action values that would otherwise be exceeded on average less frequently than once in a thousand years. However, the ratio greater than unity found in one case indicates that the limiting condition corresponds to actions that are apparently exceeded more often. In other words, when the ratio is greater than unity, the conventional model results in less rare stress values with higher exceedance probabilities. In this case, the rare percentile of the distribution is greater than the maximum value obtained with the norm scheme and, therefore, traffic restriction may be necessary. Therefore, these data highlight the importance of a control system for traffic limitation measures.

Table 33 - Ratios of percentiles of simulations and codes - traffic load only

<i>Viaduct</i>	<i>EN1991-2 load model</i>		<i>DM2020 transitable to heavy traffic load model</i>	
	M	V	M	V
<i>No.1</i>	0.54	0.50	0.68	0.58
<i>No.2</i>	0.60	0.72	0.89	1.27
<i>No.3</i>	0.55	0.58	0.65	0.75

Next, the variable actions due to traffic loads were combined with the actions due to permanent loads according to the regulatory equations. Therefore, margins of safety should be calculated based on the factored values of M and V due to the combination of traffic, permanent and possibly other loads. Table 34 shows the ratios between the design actions E_d obtained by considering the bridge-specific traffic load characteristic values obtained from simulation and those of the code-prescribed values, both calculated using the partial factors of safety. These ratios were calculated for both types of loads. These

ratios were calculated for both moments and shear forces for all three bridges. The resulting values are between 0.77-0.84 for the EN1991-2 load model and 0.78-1.13 for the DM2020 load model (440 kN), respectively. These ratios can be considered as relative measures of the safety margin of each viaduct between the two definitions of traffic-induced actions. We note that these safety margins may also vary between bridges with similar structural configurations belonging to the same road network.

Table 34 - Percentile ratios of simulations and codes - in combination

<i>Viaduct</i>	<i>EN1991-2 load model</i>		<i>DM2020 transitable to heavy traffic load model</i>	
	M	V	M	V
<i>No.1</i>	0.77	0.75	0.84	0.78
<i>No.2</i>	0.79	0.84	0.95	1.13
<i>No.3</i>	0.80	0.74	0.84	0.85

4.5. Conclusions

In the current code-based approach to bridge safety assessment, traffic loads are defined based on the exceedance return period of the structural actions they determine. This may require detailed traffic monitoring, which is rarely feasible at the infrastructure scale. The study sought to understand whether traffic microsimulations, together with structural modeling, could replace/complement monitoring.

The study considers the real case of the urban highway of Naples (Italy), which hosts about two hundred and forty thousand transits per day and has several major viaducts.

Calibration of input for traffic simulations consisted of (1) analysis of daily and hourly clusters of toll data to define origin-destination matrices, including uncertainty characterization; (2) definition of vehicle population based on regional registration data; and (3) other assumptions referring to toll queuing and driving behavior characteristics. Simulations for the entire transportation network provided the trajectories of every vehicle on the network in the year under consideration. This information, in conjunction with finite-element structural models of the bridges, allowed the determination of structural actions with the distribution of maximum internal forces derived from traffic loads.

For three viaducts, the safety margin implied by the simulation-based structural assessment was compared with that derived from the application of conventional traffic loads recommended by the Eurocodes and the current Italian guidelines for bridge evaluation. It was found that, in the case considered, the bending moments of the 1000-year return period are between 55 percent and 60 percent of the characteristic values of EN-1991-2, while the corresponding shear force maxima are between 50 percent and 70 percent.

The most significant results of this study are as follows: (i) micro-simulations seem suitable for determining structure-specific traffic loads; (ii) code-assigned loads tend to result in significantly lower margins of safety of structural action than the simulation-based counterpart; and (iii) traffic-induced loads are structure-specific, and thus simulation of the entire network was shown to be necessary. Despite these results, two caveats also emerge: (iv) the calibration of the traffic model can be compromised by the availability of traffic flow data (or lack thereof) and is critical to the defensibility of the results; (v) the traffic-induced actions with the desired return period, obtained as the low percentile of the fitted probability model, were larger than the observed maxima from the simulated data by a factor of about two, indicating that longer time intervals may need to be simulated; (vi) the study neglected, for simplicity's sake only, issues such as traffic accident simulations and the inertial effects of traffic loads on bridges. Ultimately, it is believed that this study can contribute to the development of practical approaches for the safety assessment of transportation infrastructure.

Conclusions

In recent years, special attention is given to the safety of existing bridges due to significant variations in traffic load from design standards and natural degradation of materials. This PhD thesis addresses some issues on existing bridge concerning: (i) innovative health monitoring system and (ii) the calibration of traffic loads based on actual traffic data of the road network.

Structural health monitoring

About structural health monitoring, two data processing techniques were analyzed for structural damage identification namely (i) frequency domain decomposition (FDD) for dynamic characterization of structures and (ii) artificial neural networks. The dynamic identification process makes it possible to derive the dynamic characteristics of structures with which it is possible to (i) update the numerical model and (ii) identify structural damage over time. The FDD technique allows to obtain eigenfrequencies and modal shapes of the structure using the accelerations recorded by sensors.

This technique can be used to identify structural damage if it causes a change in stiffness such that the dynamic behavior is altered. Therefore, the identification process - repeated over time - allows to assess the health condition of the structure on the basis on frequency or modal shapes changes. In particular, the application of the reviewed case studies showed that when the damage is little extensive and localized i.e., it does not significantly affect the stiffness matrix, the frequency change is insignificant and, therefore, the margin of uncertainty on the assessment of the health condition of the structure increases. In addition, the definition of a damage threshold is necessary in order to determine the presence of damage. Since the goodness of results of a dynamic identification process depends on the number and spatial distribution of sensors on the structure, it is appropriate to design the accelerometer network using optimal sensor placement (OSP) techniques. The usual techniques of optimal sensor placement make it possible to derive a ranking of the efficiency of their positions, but a selection criterion of the optimal number is not defined.

In this thesis, the EFI technique is described in order to draw up the ranking list. A selection criterion, based on simulation of the FDD technique, is then proposed to reduce the number of sensors-appropriately placed on the structure-while ensuring a high level of accuracy of identification results. The described application to the railway bridge evidences that the selection criteria with EFI method allows to define an optimal sensors configuration that minimizes the number of instruments and maximizes the level of accuracy of the FDD results. However, the definition of the optimal configuration must be realized by means of a numerical model corresponding to the real behavior of the structure. Therefore, the updating of the FE model of the structure is necessary at the outset and whenever a damage condition occurs that alters the real structural behavior.

The artificial intelligence techniques allows to detect some structural anomalies using the unsupervised approach.

With this approach, the structural damage is identified without the use of FE model of the structure. Indeed, since the training phase is performed only with data recorded on the healthy structure, it is not necessary to simulate all possible damage conditions by FE model. Conversely, with a supervised approach, training of the artificial neural network must also be performed with data in a damaged condition. Therefore, via FE model, it is necessary to simulate the possible damage conditions in order to extract the training data of the network. A damage detection framework based on a VAE and an OC-SVM has been proposed. The method allows to automate the entire damage identification process taking less time than a traditional SHM technique because it works directly on the raw data. In addition, the process is automated, i.e., any user-defined decision rules are avoided through the use of OC-SVM. The error metrics used as damage-sensitive features are valid for the classification of the structural health condition because the use of VAE allows to model heterogeneous data with different generation distributions. So, in the case of damaged data, the probabilistic encoder models different data distributions and the error committed by the network increases. The methodology was applied to two different structural types - tested in the laboratory - under different damage scenarios in order to demonstrate the validity of the technique. Moreover, for the case of prestressed joists, the algorithm was applied on both static and dynamic measurements. The results show that, although the algorithm is effective with both static and dynamic measurements, the results obtained with acceleration data perform better because the volume of data with which network training is performed is larger. The comparison of this framework with dynamic identification techniques, on the other hand, highlights the potential of the innovative neural network-based method for identifying structural damage even when it is little extensive and localized. Finally, the framework does not offer the ability to localize damage based on the score detected by individual sensors.

The case studies that are shown in this thesis show that: (i) on the one hand, dynamic identification techniques are strongly established both for the purpose of updating the numerical model and for structural damage identification; (ii) on the other hand, the applications of artificial intelligence techniques to the field of civil engineering are in a continuous state of advancement especially with regard to the testing phase to real case studies and the optimization of the network training process.

In the future, the author would like (i) to validate the proposed methodology to real case studies, (ii) to make the methodology effective for structural damage localization, and finally, (iii) to use transfer learning processes for neural network training to optimize the process.

In the future, we will extend the procedure to the location of the damage. For this, EXplainable Artificial Intelligence (XAI) methods can allow a greater understanding of the results of deep learning models and, thus, they may be useful to damage localization. Moreover, since it has been verified that network performance increases with the amount of data with which the training is performed, transfer learning techniques will be deepened. In fact, it is found that the biggest problem in the application of artificial intelligence techniques to structural monitoring is currently the shortage of large amounts of data on real structures. Transfer learning techniques are used in deep learning to retrain a neural network model, in order to solve a problem similar to the one for

which it was designed. This would then allow you to extend the data set - even using numerical simulations.

Traffic load model

About the traffic load schemes, since the probability of exceeding the code-prescribed traffic effect on a specific bridge in a time interval depends on the characterization of traffic on the transportation network to which the bridge belongs and considering that detailed traffic monitoring is rarely feasible at the infrastructure scale, this study sought to understand whether traffic microsimulations could replace/complement monitoring. The study considers the real case of the urban highway in Naples, Italy. Simulations for the entire transportation network provided the trajectories of each vehicle on the network in the considered year. This information - joint with the finite element structural models of the bridges - allowed the assessment of the distribution of maximum internal forces derived from traffic loads. For three viaducts, the safety margin implied by the simulation was compared with that derived from the application of normative traffic loads.

The study showed that: (i) the micro-simulations seem fit-for-purpose for structure-specific determination of traffic loads; (ii) the code-assigned loads tend to determine structural action safety margins significantly lower than the simulation-based counterpart; (iii) the traffic-induced loads are structure specific, and then the simulation of the entire network has been shown necessary. These results notwithstanding, two caveats also emerge: (iv) approach should beware that, the calibration of the traffic model may be impaired by the availability of traffic flow data (or lack thereof) and is critical for the defensibility of the results; (v) traffic-induced actions with the desired return period, obtained as a low percentile of the fitted probability model, were larger than the maxima observed from simulated data by a factor of roughly two, indicating that longer time intervals may need to be simulated; (vi) the study neglected, only for simplicity, issues such as simulations of traffic accidents and the inertial effects of traffic loads on the bridges.

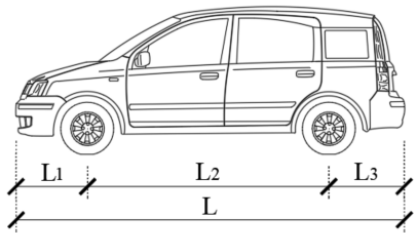
In the future, the methodology could be used to calibrate correction coefficients of partial safety factors for structural safety checks of existing bridges.

Annex A

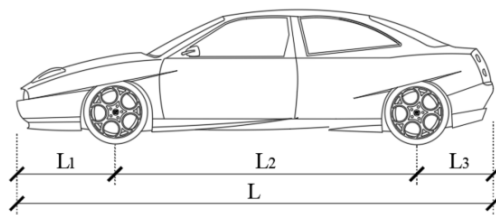
In this section, the geometries of the vehicles considered in the micro-traffic simulation are reported.

The table shows the distances between axles for each type of vehicle.

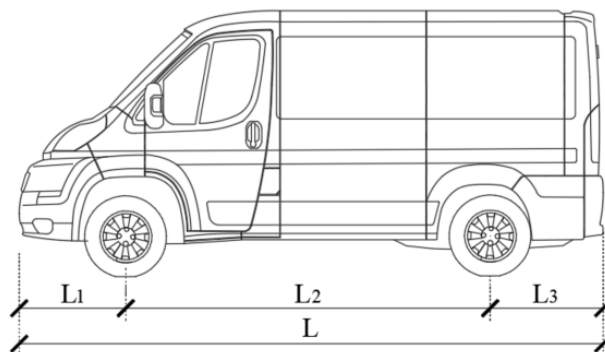
Toll	Type	ID	L	L ₁	L ₂	L ₃	L ₄	L ₅	L ₆
	-	-	m	m	m	m	m	m	m
II	Car < 4.5m	car1	3.75	0.70	2.40	-	-	-	-
	Car ≥ 4.5m	car2	4.60	0.90	2.80	-	-	-	-
	truck	A2	8.40	1.30	6.00	-	-	-	-
	bus	B2	10.70	2.40	5.40	-	-	-	-
	van	VAN	4.85	0.90	3.10	-	-	-	-
III	truck	A3	9.85	1.40	4.80	1.40	-	-	-
	articulated	AA3	12.50	1.40	3.70	5.90	-	-	-
	trailer truck	AT3	18.75	1.40	5.60	7.90	-	-	-
	bus	B3	15	2.80	9.50	1.30	-	-	-
IV	truck	A4I	10.23	1.50	1.95	3.20	1.60	-	-
	truck	A4II	13.26	1.45	4.10	1.35	1.35	-	-
	articulated	AA4	12.50	1.45	3.70	5.00	1.35	-	-
	trailer truck	AT4	18.75	1.40	5.60	4.85	5.80	-	-
V	articulated	AA5I	16.50	1.45	3.40	1.30	5.90	1.30	1.85
	articulated	AA5II	16.50	1.40	3.70	4.70	1.30	1.30	4.10
	trailer truck	AT5	18.75	1.40	4.80	1.35	5.00	5.45	0.75



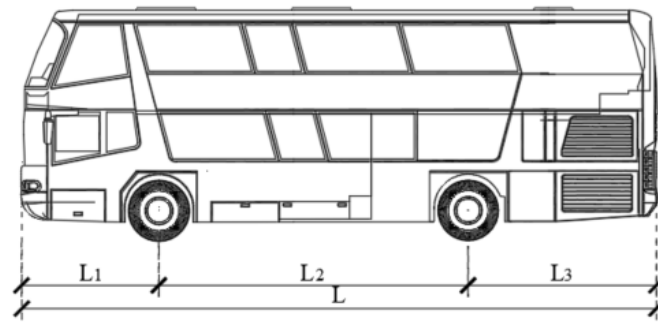
Car < 4.5m – ID: car1



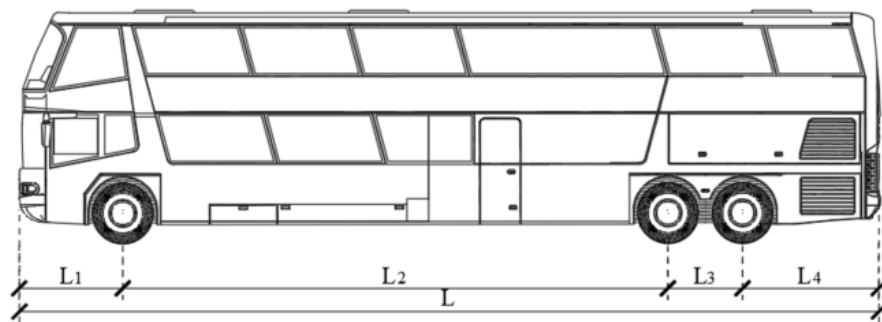
Car ≥ 4.5m – ID: car2



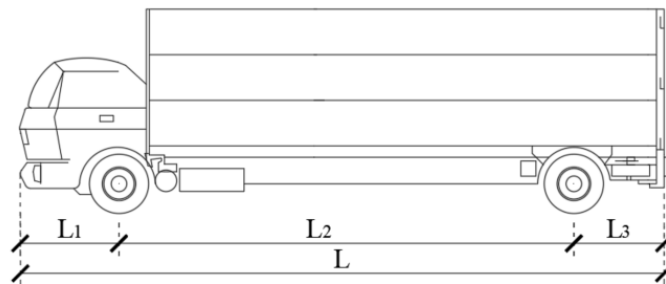
Van – ID: VAN



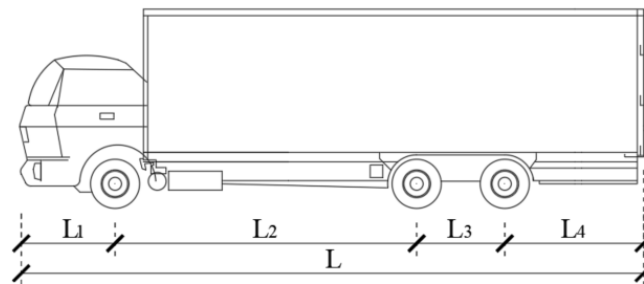
Bus – ID: B2



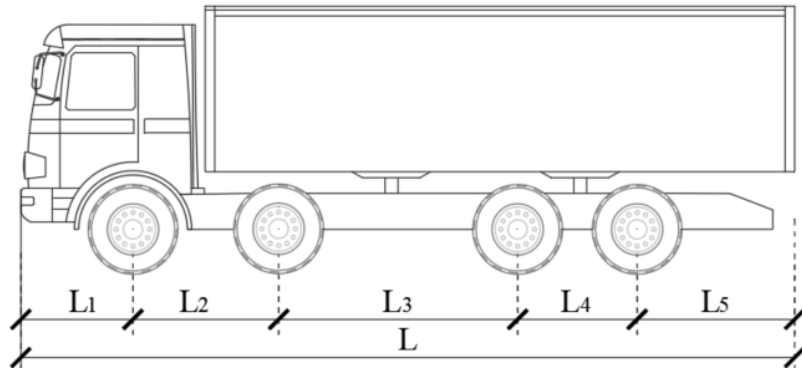
Bus – ID: B3



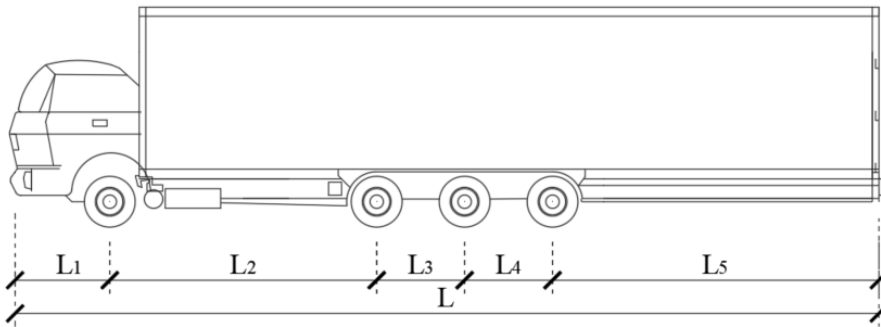
Truck – ID: A2



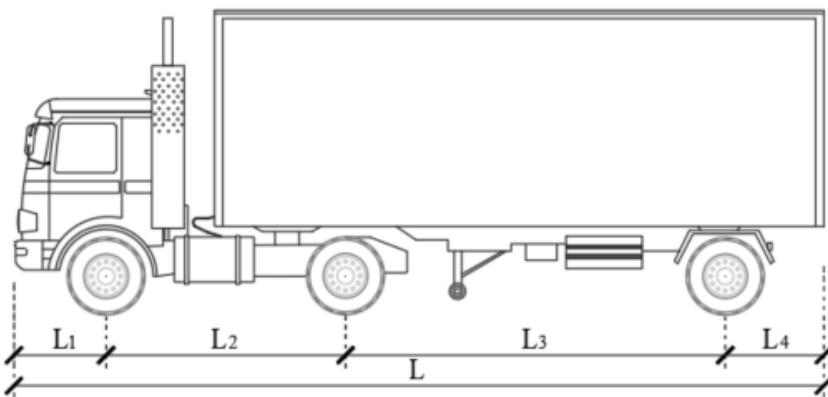
Truck – ID: A3



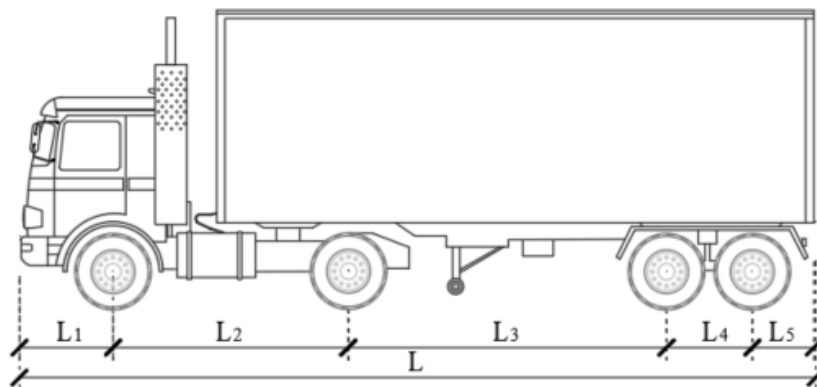
Truck – ID: A4I



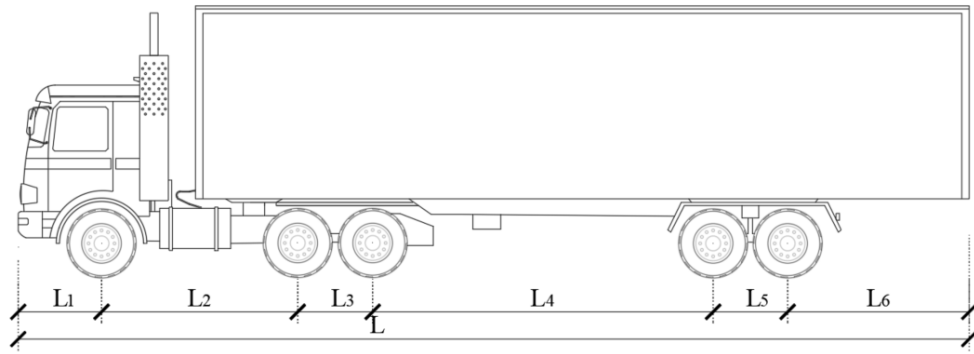
Truck – ID: A4II



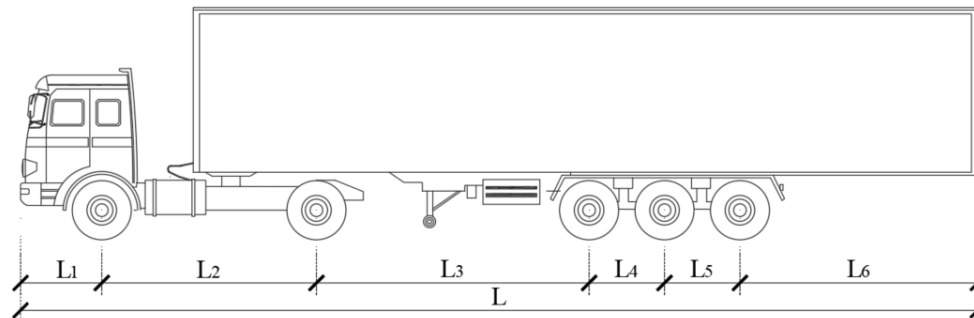
Articulated lorry – ID: AA3



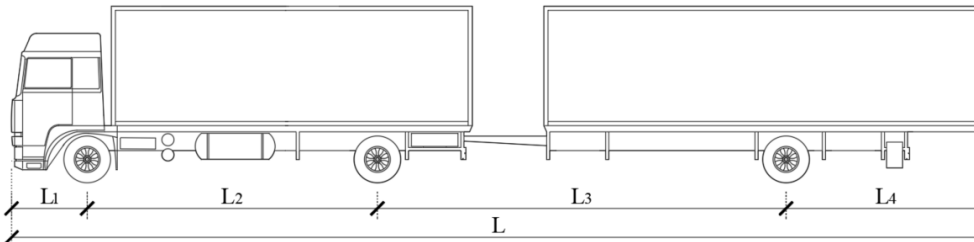
Articulated lorry – ID: AA4I



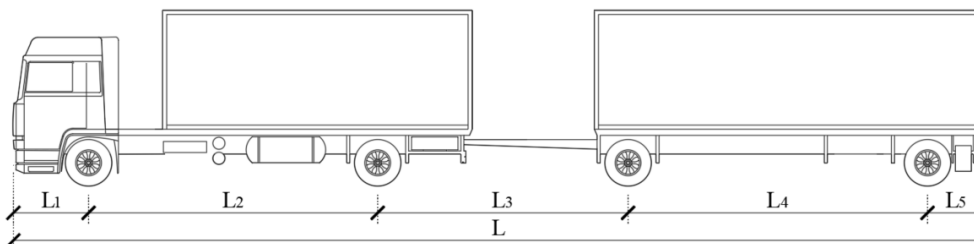
Articulated lorry – ID: AA5I



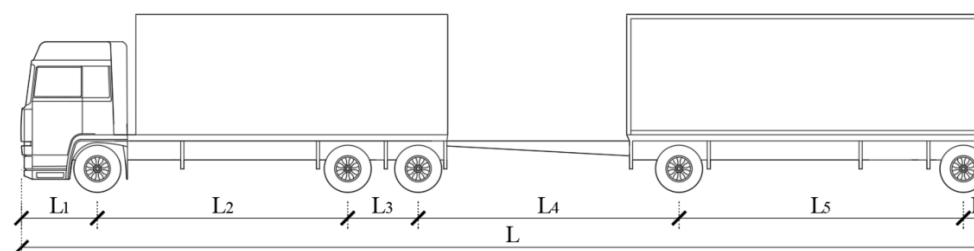
Articulated lorry – ID: AA5II



Trailer truck – ID: AT3



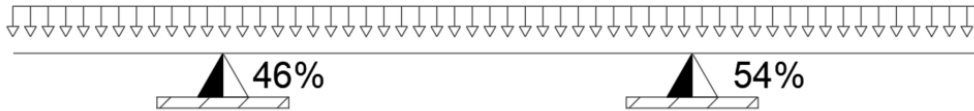
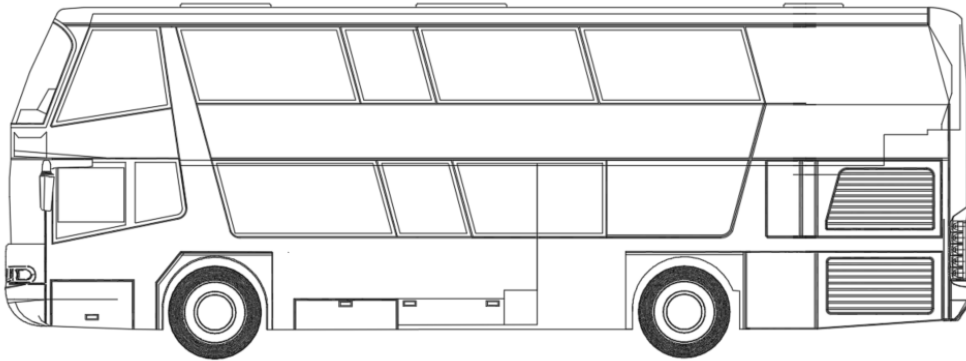
Trailer truck – ID: AT4



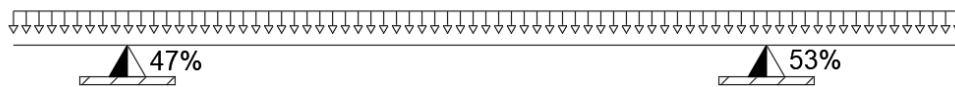
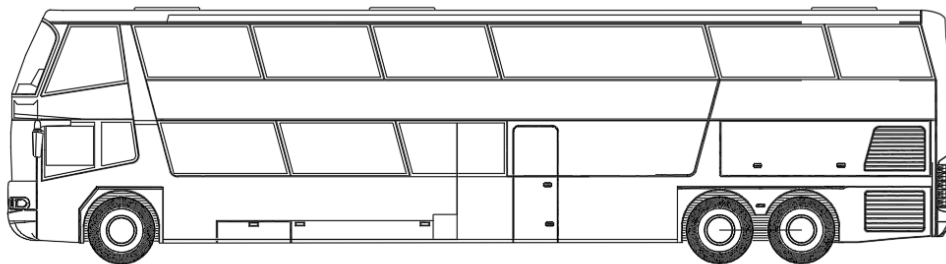
Trailer truck – ID: AT5

Annex B

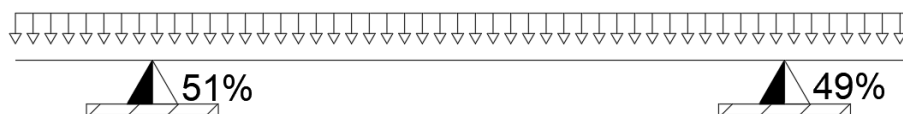
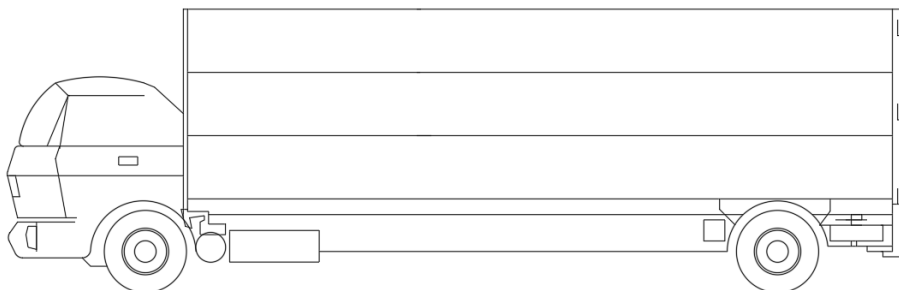
In this section, the geometries of the vehicles considered in the micro-traffic simulation are reported.



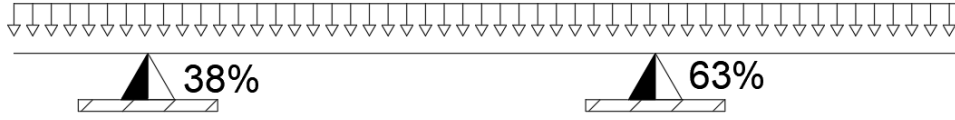
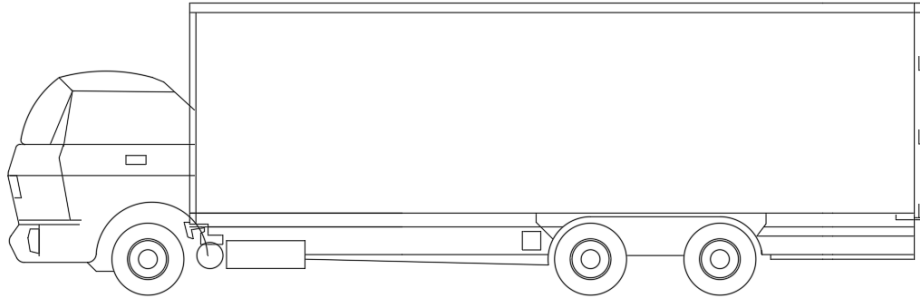
Bus – ID: B2



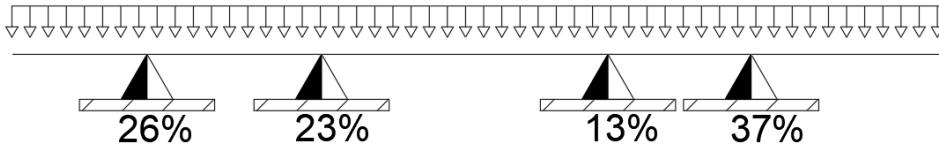
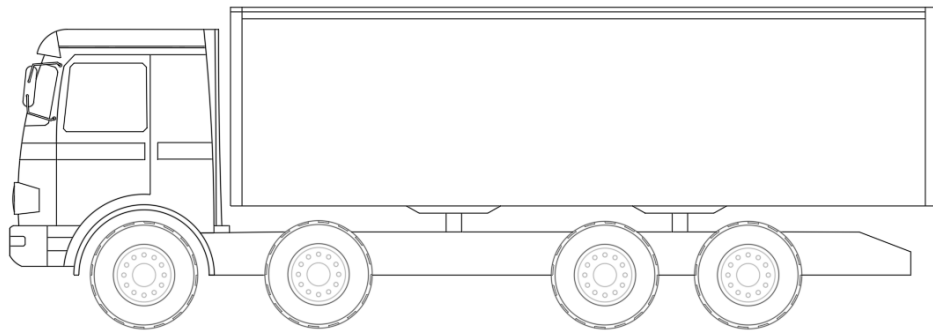
Bus – ID: B3



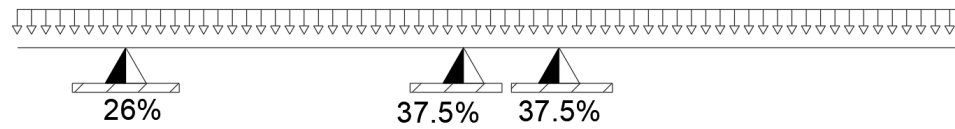
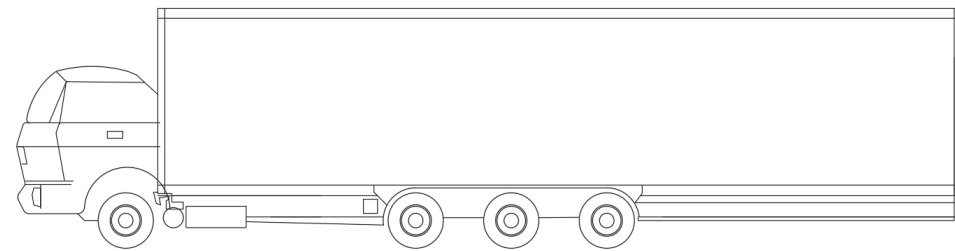
Truck – ID: A2



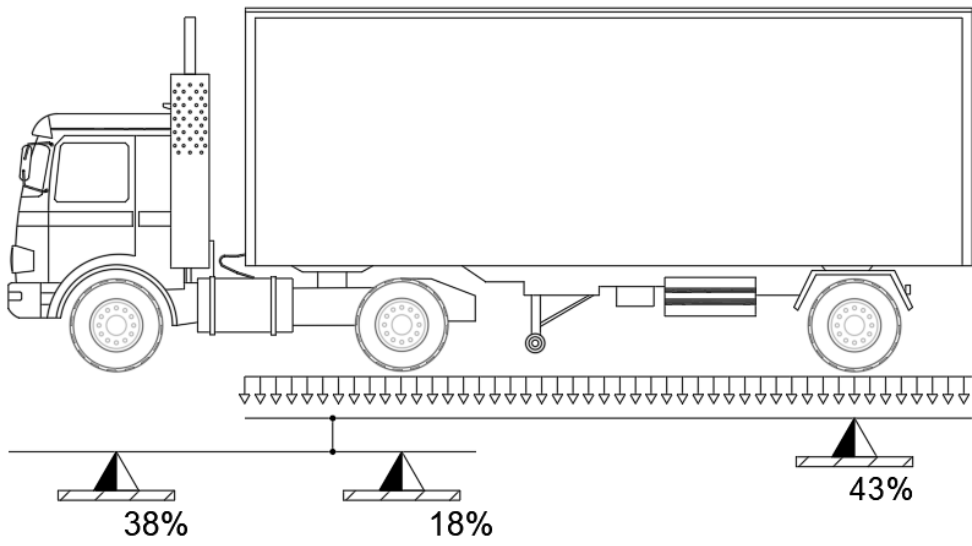
Truck – ID: A3



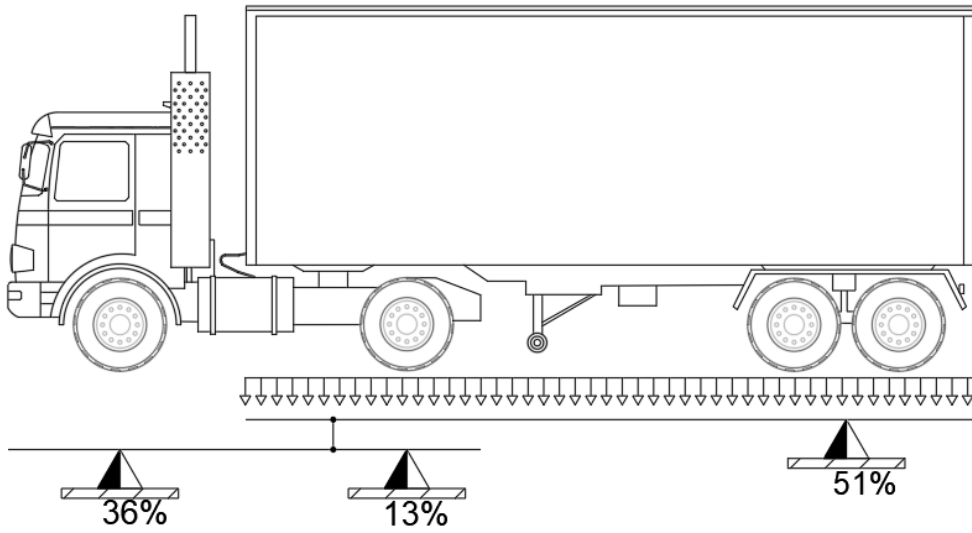
Truck – ID: A4I



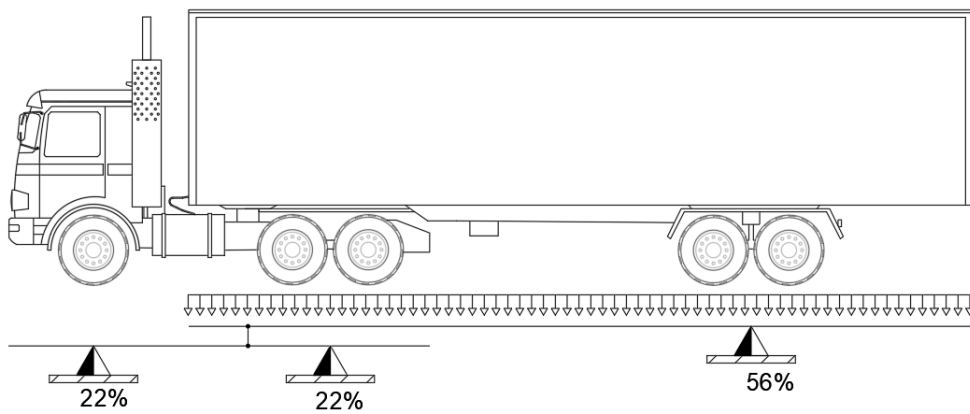
Truck – ID: A4II



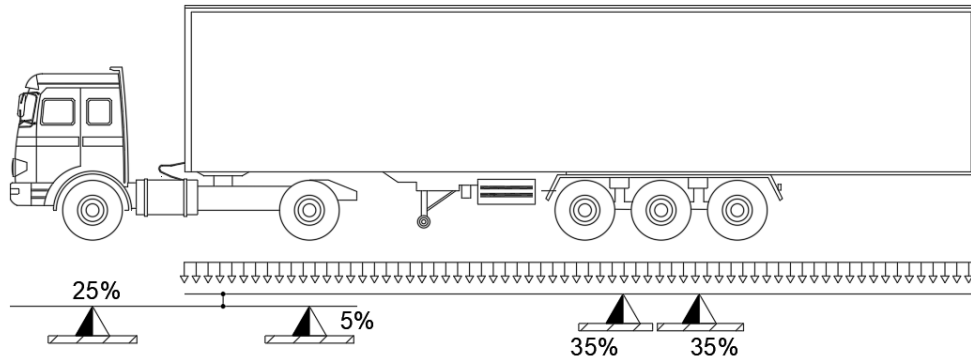
Articulated lorry – ID: AA3



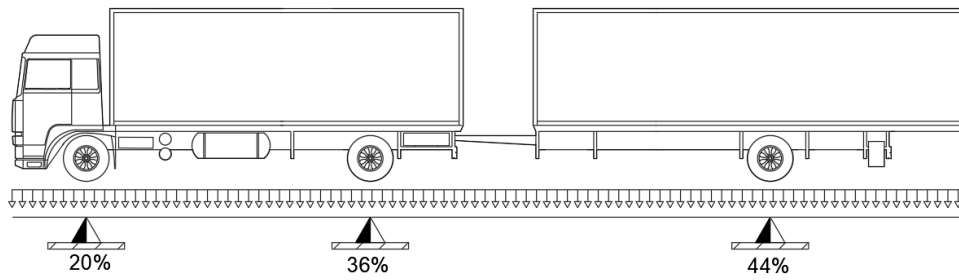
Articulated lorry – ID: AA4I



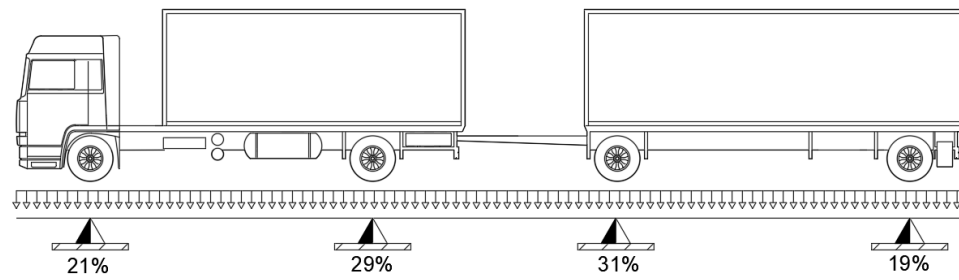
Articulated lorry – ID: AA5I



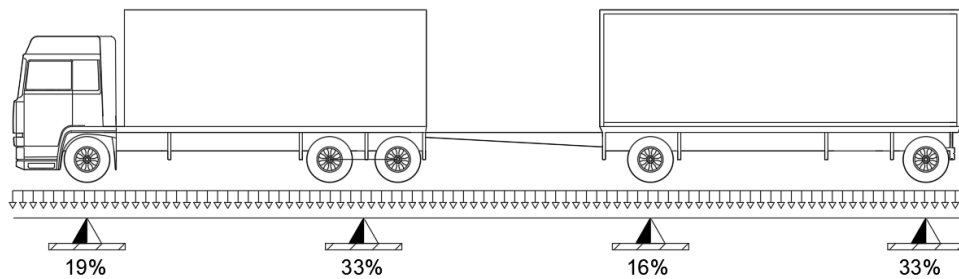
Articulated lorry – ID: AA5II



Trailer truck – ID: AT3



Trailer truck – ID: AT4



Trailer truck – ID: AT5

References

- AASHTO, (2020): AASHTO LRFD Bridge Design Specifications. *American Association of State Highway and Transportation Officials, Washington, D.C.*
- Abdeljaber, O.; Avci, O.; Kiranyaz, S.; Gabbouj, M.; Inman, D. J., (2017): Real-time vibration-based structural damage detection using one-dimensional convolutional neural networks. *Journal of Sound and Vibration.*, **388**, 154–170.
- Adeli, H.; Ghosh-Dastidar, S., (2004): Mesoscopic-wavelet freeway work zone flow and congestion feature extraction model. *Journal of Transportation Engineering.*, **130**, 94–103.
- Akintunde, E.; Eftekhar Azam, S.; Rageh, A.; Linzell, D. G., (2021): Unsupervised Machine Learning for Robust Bridge Damage Detection: Full-Scale Experimental Validation. *Engineering Structures.*, **249**, 113250.
- Alvandi, A.; Cremona, C., (2006): Assessment of vibration-based damage identification techniques. *Journal of Sound and Vibration.*, **292**, 179–202.
- An, J., & Cho, S., (2015): Variational autoencoder based anomaly detection using reconstruction probability. *Special Lecture on IE*.
- Anders Rytter, (1993): Vibrational Based Inspection of Civil Engineering Structures, **44**, 193.
- Arora, P.; Deepali; Varshney, S., (2016): Analysis of K-Means and K-Medoids Algorithm For Big Data. *Procedia Computer Science.*, **78**, 507–512.
- ASCE/SEI 7 -22, (2022): Minimum Design Loads and Associated Criteria for Buildings and Other Structures.
- Au, S. K., (2011): Assembling mode shapes by least squares. *Mechanical Systems and Signal Processing.*, **25**, 163–179.
- Au, S. K., (2017): *Operational Modal Analysis*. Springer Singapore, Singapore.
- Bao, Y.; Tang, Z.; Li, H.; Zhang, Y., (2019): Computer vision and deep learning-based data anomaly detection method for structural health monitoring. *Structural Health Monitoring.*, **18**, 401–421.
- Behmanesh, I.; Moaveni, B.; Lombaert, G.; Papadimitriou, C., (2015): Hierarchical Bayesian model updating for structural identification. *Mechanical Systems and Signal Processing.*, **64–65**, 360–376.
- Benjamin, J. R.; Cornell, C. A., (2014): *Probability, statistics, and decision for civil engineers*. (Courier Corporation, Ed.).
- Bilotta, A.; De Angelis, A.; Testa, G.; Starace, L.; Pecce, M. R., (2021): Use of static and dynamic test results for model updating of a steel-concrete composite bridge. *Proc. of the 2nd fib Symposium on Concrete and Concrete Structures Nov 18th-19th, 2021, Sapienza University, Rome, Italy*.
- Bodeux, J. B.; Golinval, J. C., (2001): Application of ARMAV models to the identification and damage detection of mechanical and civil engineering structures. *Smart Materials and Structures.*, **10**, 479–489.
- Brigante, D.; Rainieri, C.; Fabbrocino, G., (2017): The role of the Modal Assurance Criterion in the interpretation and validation of models for seismic analysis of architectural complexes. *Procedia Engineering.*, **199**, 3404–3409.
- Brincker, R., Zhang, L., & Andersen, P., (2000): Modal identification from ambient responses using frequency domain decomposition. *In Proceedings of the 18th international modal analysis conference (IMAC).*, **1**, 625–630.
- Bu, Y.; Zou, S.; Liang, Y.; Veeravalli, V. V., (2018): Estimation of KL Divergence: Optimal Minimax Rate. *IEEE Transactions on Information Theory.*, **64**, 2648–2674.
- Buisson, C.; Daamen, W.; Punzo, V.; Wagner, P.; Montanino, M.; Ciuffo, B., (2014): Calibration and validation principles. *Traffic Simulation and Data*. CRC Press, pp. 105–134.
- Caprani, C. C., (2010): Using Microsimulation to Estimate Highway Bridge Traffic Load. *In Proc. 5th Intl. Conf. on Bridge Maintenance, Safety and Management*.
- Cascetta, E.; Punzo, V.; Montanino, M., (2011): Empirical Analysis of Effects of

Automated Section Speed Enforcement System on Traffic Flow at Freeway Bottlenecks. *Transportation Research Record: Journal of the Transportation Research Board.*, **2260**, 83–93.

Cha, Y. J.; Choi, W.; Büyüköztürk, O., (2017): Deep Learning-Based Crack Damage Detection Using Convolutional Neural Networks. *Computer-Aided Civil and Infrastructure Engineering.*, **32**, 361–378.

Cha, Y. J.; Wang, Z., (2018): Automated damage-sensitive feature extraction using unsupervised convolutional neural networks. In: Sohn, H. (ed.), *Sensors and Smart Structures Technologies for Civil, Mechanical, and Aerospace Systems 2018*. SPIE, p. 54.

Chang, C. M.; Lin, T. K.; Chang, C. W., (2018): Applications of neural network models for structural health monitoring based on derived modal properties. *Measurement: Journal of the International Measurement Confederation.*, **129**, 457–470.

Chang, M.; Pakzad, S. N., (2014): Optimal Sensor Placement for Modal Identification of Bridge Systems Considering Number of Sensing Nodes. *Journal of Bridge Engineering.*, **19**.

Chen, L.; Chen, W.; Wang, L.; Zhai, C.; Hu, X.; Sun, L.; Tian, Y.; Huang, X.; Jiang, L., (2023): Convolutional neural networks (CNNs)-based multi-category damage detection and recognition of high-speed rail (HSR) reinforced concrete (RC) bridges using test images. *Engineering Structures.*, **276**, 115306.

Chen, S. Z.; Feng, D. C.; Sun, Z., (2021): Reliability-based vehicle weight limit determination for urban bridge network subjected to stochastic traffic flow considering vehicle-bridge coupling. *Engineering Structures.*, **247**, 113166.

Chisari, C.; Macorini, L.; Amadio, C.; Izzuddin, B. A., (2017): Optimal sensor placement for structural parameter identification. *Structural and Multidisciplinary Optimization.*, **55**, 647–662.

Choe, D. E.; Kim, H. C.; Kim, M. H., (2021): Sequence-based modeling of deep learning with LSTM and GRU networks for structural damage detection of floating offshore wind turbine blades. *Renewable Energy.*, **174**, 218–235.

Ciuffo, B.; Punzo, V.; Torrieri, V., (2008): Comparison of Simulation-Based and Model-Based Calibrations of Traffic-Flow Microsimulation Models. *Transportation Research Record: Journal of the Transportation Research Board.*, **2088**, 36–44.

Ciuffo, B.; Punzo, V.; Montanino, M., (2012): Thirty Years of Gipps' Car-Following Model. *Transportation Research Record: Journal of the Transportation Research Board.*, **2315**, 89–99.

Cosenza E., Manfredi G., P. M., (2016): Strutture in cemento armato. Basi della progettazione, **2**.

Courbon, J., (1971): TORSION OF CONTINUOUS GIRDERS WITH A THIN OPEN CROSS SECTION.

CS.LL.PP., (2020): Linee Guida per la classificazione e gestione del rischio, la valutazione della sicurezza e il monitoraggio dei ponti esistenti. *Gazzetta Ufficiale della Repubblica Italiana*.

Cuong-Le, T.; Nghia-Nguyen, T.; Khatir, S.; Trong-Nguyen, P.; Mirjalili, S.; Nguyen, K. D., (2022): An efficient approach for damage identification based on improved machine learning using PSO-SVM. *Engineering with Computers.*, **38**, 3069–3084.

Curadelli, R. O.; Riera, J. D.; Ambrosini, D.; Amani, M. G., (2008): Damage detection by means of structural damping identification. *Engineering Structures.*, **30**, 3497–3504.

D. Bernal, S. J. Dyke, H.F. Lam, J. L. B., (2002): PHASE II OF THE ASCE BENCHMARK STUDY ON SHM. *15th ASCE Engineering Mechanics Conference*.

D.Lgs n.285/1992, (1992): Nuovo Codice della Strada. *Gazzetta Ufficiale della Repubblica Italiana*.

Dai, B.; Wu, D.; Li, Q., (2022): Investigation of multiple-presence factor for traffic loads on road-rail bridges based on a novel extreme value analysis approach. *Structural*

Safety., **96**.

- De Angelis, A.; Esposito, G.; Maddaloni, G.; Cosenza, E.; Pecce, M. R., (2021): AMBIENT VIBRATION TEST ON AN EXISTING PRESTRESSED CONCRETE BRIDGE, pp. 3720–3730.
- Dung, C. V.; Anh, L. D., (2019): Autonomous concrete crack detection using deep fully convolutional neural network. *Automation in Construction.*, **99**, 52–58.
- EN 1991 - 2, (2003): Traffic loads on bridge. *The European Union Per Regulation 305/2011, Directive 98/34/EC, Directive 2004/18/EC*.
- Enright, B.; Carey, C.; Caprani, C. C., (2013): Microsimulation Evaluation of Eurocode Load Model for American Long-Span Bridges. *Journal of Bridge Engineering.*, **18**, 1252–1260.
- Ewins, D. J., (2000): Modal Testing: Theory and Practice. *Research Studies Press Ltd., Baldock, 2nd edition*.
- Fan W, Q. P., (2011): Vibration-based Damage Identification Methods: A Review and Comparative Study. *Structural Health Monitoring.*, **10**, 83–111.
- Fassois, S. D.; Sakellariou, J. S., (2007): Time-series methods for fault detection and identification in vibrating structures. *Philosophical Transactions of the Royal Society A: Mathematical, Physical and Engineering Sciences.*, **365**, 411–448.
- Ferson, S.; Oberkampf, W. L.; Ginzburg, L., (2008): Model validation and predictive capability for the thermal challenge problem. *Computer Methods in Applied Mechanics and Engineering.*, **197**, 2408–2430.
- fib Bulletin No. 80, (2016): Partial factor methods for existing concrete structures, 129.
- Gao, Y.; Mosalam, K. M., (2018): Deep Transfer Learning for Image-Based Structural Damage Recognition. *Computer-Aided Civil and Infrastructure Engineering.*, **33**, 748–768.
- Gentile, C.; Guidobaldi, M.; Saisi, A., (2016): One-year dynamic monitoring of a historic tower: damage detection under changing environment. *Meccanica.*, **51**, 2873–2889.
- Ghannadi, P.; Kourehli, S. S., (2019): Structural damage detection based on MAC flexibility and frequency using moth-flame algorithm. *Structural Engineering and Mechanics.*, **70**, 649–659.
- Ghosh-dastidar, S.; Adeli, H., (2006): for Delay and Queue Length Estimation. *Journal of Transportation Engineering.*, 331–341.
- Giordano, E.; Mendes, N.; Masciotta, M. G.; Clementi, F.; Sadeghi, N. H.; Silva, R. A.; Oliveira, D. V., (2020): Expedient damage index for arched structures based on dynamic identification testing. *Construction and Building Materials.*, **265**, 120236.
- Gomes, G. F.; Mendéz, Y. A. D.; da Silva Lopes Alexandrino, P.; da Cunha, S. S.; Ancelotti, A. C., (2018): The use of intelligent computational tools for damage detection and identification with an emphasis on composites – A review. *Composite Structures.*, **196**, 44–54.
- Grakovski, A.; Yunusov, S.; Medvedev, A., (2020): Static Approach for Solving the Problem of Cargo Weight Distribution on Vehicle's Axles, pp. 151–161.
- Guo, D.; Caprani, C. C., (2019): Traffic load patterning on long span bridges: A rational approach. *Structural Safety.*, **77**, 18–29.
- Heylen, P. W.; Lammens, S.; Sas, (1998): Modal analysis theory and testing. *Katholieke Universiteit Leuven, Faculty of Engineering, Department of Mechanical Engineering, Division of 460 Production Engineering. Machine Design and Automation*.
- Hou, N.; Sun, L.; Chen, L., (2021): Modeling vehicle load for a long-span bridge based on weigh in motion data. *Measurement: Journal of the International Measurement Confederation.*, **183**, 109727.
- Huseynov, F.; Kim, C.; O'Brien, E. J.; Brownjohn, J. M. W.; Hester, D.; Chang, K. C., (2020): Bridge damage detection using rotation measurements – Experimental validation. *Mechanical Systems and Signal Processing.*, **135**, 106380.
- Huth, O.; Feltrin, G.; Maeck, J.; Kilic, N.; Motavalli, M., (2005): Damage

Identification Using Modal Data: Experiences on a Prestressed Concrete Bridge. *Journal of Structural Engineering.*, **131**, 1898–1910.

Iervolino Iuno, (2021): DINAMICA DELLE STRUTTURE E INGEGNERIA SISMICA, **1**.

Jaishi, B.; Ren, W. X., (2005): Structural Finite Element Model Updating Using Ambient Vibration Test Results. *Journal of Structural Engineering.*, **131**, 617–628.

Jiang, X.; Adeli, H., (2004): Wavelet packet-autocorrelation function method for traffic flow pattern analysis. *Computer-Aided Civil and Infrastructure Engineering.*, **19**, 324–337.

Jin, C.; Jang, S.; Sun, X., (2017): An integrated real-time structural damage detection method based on extended Kalman filter and dynamic statistical process control. *Advances in Structural Engineering.*, **20**, 549–563.

Kammer, D. C., (1991): Sensor placement for on-orbit modal identification and correlation of large space structures. *Journal of Guidance, Control, and Dynamics.*, **14**, 251–2019.

Kang, J. S.; Park, S. K.; Shin, S.; Lee, H. S., (2005): Structural system identification in time domain using measured acceleration. *Journal of Sound and Vibration.*, **288**, 215–234.

Karim, A.; Adeli, H., (2002): Incident detection algorithm using wavelet energy representation of traffic patterns. *Journal of Transportation Engineering.*, **128**, 232–242.

Kim, J.; Song, J., (2022): A Design Live Load Model for Long-Span Bridges Based on Traffic Data and Simulations. *ASCE-ASME Journal of Risk and Uncertainty in Engineering Systems, Part A: Civil Engineering.*, **8**.

Kollbrunner and Basler, (1969): Torsion in Structures. *The Aeronautical Journal.*, **Edited in**, 280.

Koteš, P.; Vičan, J., (2013): Recommended reliability levels for the evaluation of existing bridges according to eurocodes. *Structural Engineering International: Journal of the International Association for Bridge and Structural Engineering (IABSE).*, **23**, 411–417.

Li, H.; Ou, J.; Zhao, X.; Zhou, W.; Li, H.; Zhou, Z.; Yang, Y., (2006): Structural Health Monitoring System for the Shandong Binzhou Yellow River Highway Bridge. *Computer-Aided Civil and Infrastructure Engineering.*, **21**, 306–317.

Lin, Y. Z.; Nie, Z. H.; Ma, H. W., (2017): Structural Damage Detection with Automatic Feature-Extraction through Deep Learning. *Computer-Aided Civil and Infrastructure Engineering.*, **32**, 1025–1046.

Liu, K.; Yan, R. J.; Guedes Soares, C., (2018): Optimal sensor placement and assessment for modal identification. *Ocean Engineering.*, **165**, 209–220.

Liu, T.; Zhang, Q.; Zordan, T.; Briseghella, B., (2016): Finite Element Model Updating of Canonica Bridge Using Experimental Modal Data and Genetic Algorithm. *Structural Engineering International.*, **26**, 27–36.

Lu, Q.; Harvey, J.; Lea, T.; Quinley, R.; Redo, D.; Avis, J., (2002): Truck traffic analysis using Weigh-In-Motion (WIM) data in California. *University of California, Berkeley, Institute of Transportation Studies Pavement Research Center.*

Luleci, F.; Catbas, F. N.; Avci, O., (2022): Generative Adversarial Networks for Data Generation in Structural Health Monitoring. *Frontiers in Built Environment.*, **8**, 1–17.

Luo, J.; Huang, M.; Lei, Y., (2022): Temperature Effect on Vibration Properties and Vibration-Based Damage Identification of Bridge Structures: A Literature Review. *Vibrational Based Inspection of Civil Engineering Structure, Ph.D. Dissertation, Department of Building Technology and Structural Engineering, Aalborg University, Denmark.*, **12**, 1209.

Luo, Y.; Guo, X.; Wang, L. K.; Zheng, J. L.; Liu, J. L.; Liao, F. Y., (2023): Unsupervised structural damage detection based on an improved generative adversarial network and cloud model. *Journal of Low Frequency Noise Vibration and Active Control.*, **0**, 1–18.

- Lydon, M.; Taylor, S. E.; Robinson, D.; Mufti, A.; Brien, E. J. O., (2016): Recent developments in bridge weigh in motion (B-WIM). *Journal of Civil Structural Health Monitoring.*, **6**, 69–81.
- Ma, X.; Lin, Y.; Nie, Z.; Ma, H., (2020): Structural damage identification based on unsupervised feature-extraction via Variational Auto-encoder. *Measurement.*, **160**, 107811.
- Mannor, S.; Jin, X.; Han, J.; Jin, X.; Han, J.; Jin, X.; Han, J.; Zhang, X., (2011): K-Medoids Clustering. *Encyclopedia of Machine Learning*. Springer US, Boston, MA, pp. 564–565.
- Mao, J.; Wang, H.; Spencer, B. F., (2021): Toward data anomaly detection for automated structural health monitoring: Exploiting generative adversarial nets and autoencoders. *Structural Health Monitoring.*, **20**, 1609–1626.
- Meixedo, A.; Santos, J.; Ribeiro, D.; Calçada, R.; Todd, M., (2021): Damage detection in railway bridges using traffic-induced dynamic responses. *Engineering Structures.*, **238**.
- Meli, E.; Pugi, L., (2013): Preliminary development, simulation and validation of a weigh in motion system for railway vehicles. *Meccanica.*, **48**, 2541–2565.
- Menn, C., (1990): *Prestressed concrete bridges*. (Springer Science & Business Media, Ed.).
- Mevel L.; M., B.; Benveniste A. A.; Goursat M., (2019): Merging sensor data from multiple measurement set-ups for non-stationary subspace-based modal analysis. *Journal of Sound and Vibration*.
- Michele Meo, G. Z., (2004): Optimal sensor placement on a large-scale civil structure. *NDE for Health Monitoring and Diagnostics.*, **5394**.
- Micu, E. A.; Malekjafarian, A.; OBrien, E. J.; Quilligan, M.; McKinstry, R.; Angus, E.; Lydon, M.; Catbas, F. N., (2019): Evaluation of the extreme traffic load effects on the Forth Road Bridge using image analysis of traffic data. *Advances in Engineering Software.*, **137**, 102711.
- Mirsolav, P.; Michal, B.; Tomas, H., (2012): Modal assurance criterion, *Procedia engineering*.
- Moussas, V. C., & Pnevmatikos, N., (2019): SENSOR PLACEMENT SELECTION FOR SHM OF BUILDINGS. *7-th ECCOMAS Thematic Conference on Computational Methods in Structural Dynamics and Earthquake Engineering*.
- Nguyen, D. H.; Abdel Wahab, M., (2023): Damage detection in slab structures based on two-dimensional curvature mode shape method and Faster R-CNN. *Advances in Engineering Software.*, **176**, 103371.
- Nieminen, V.; Sapanen, J., (2023): Optimal sensor placement of triaxial accelerometers for modal expansion. *Mechanical Systems and Signal Processing.*, **184**, 109581.
- O' Brien, E. J.; Schmidt, F.; Hajjalizadeh, D.; Zhou, X. Y.; Enright, B.; Caprani, C. C.; Wilson, S.; Sheils, E., (2015): A review of probabilistic methods of assessment of load effects in bridges. *Structural Safety.*, **53**, 44–56.
- O'Connor, A.; O'Brien, E. J., (2005): Traffic load modelling and factors influencing the accuracy of predicted extremes. *Canadian Journal of Civil Engineering.*, **32**, 270–278.
- O' Brien, E. J.; Bordallo-Ruiz, A.; Enright, B., (2014): Lifetime maximum load effects on short-span bridges subject to growing traffic volumes. *Structural Safety.*, **50**, 113–122.
- Olstam, J.; Tapani, A., (2011): A Review of Guidelines for Applying Traffic Simulation to Level-of-service Analysis. *Procedia - Social and Behavioral Sciences.*, **16**, 771–780.
- Pachón, P.; Infantes, M.; Cámara, M.; Compán, V.; García-Macías, E.; Friswell, M. I.; Castro-Triguero, R., (2020): Evaluation of optimal sensor placement algorithms for the Structural Health Monitoring of architectural heritage. Application to the Monastery of San Jerónimo de Buenavista (Seville, Spain). *Engineering Structures.*, **202**, 109843.

Pandey, A. K.; Biswas, M., (1994): Damage Detection in Structures Using Changes in Flexibility. *Journal of Sound and Vibration.*, **169**, 3–17.

Papadimitriou, C., (2004): Optimal sensor placement methodology for parametric identification of structural systems. *Journal of Sound and Vibration.*, **278**, 923–947.

Papadopoulos, M.; Garcia, E., (1998): Sensor Placement Methodologies for Dynamic Testing. *AIAA Journal.*, **36**, 256–263.

Pathirage, C. . S. N.; Li, J.; Li, L.; Hao, H.; Wang., L.; Wang, R.; P. Ni, (2018): Structural damage identification based on autoencoder neural networks and deep learning. *Engineering Structures.*

Pathirage, C. . S. N.; Li, J.; Li, L.; Hao, H.; Wang., L.; R. Wang, (2019): Development and application of a deep learning–based sparse autoencoder framework for structural damage identification. *Structural Health Monitoring.*

Pereira, S.; Reynders, E.; Magalhães, F.; Cunha, Á.; Gomes, J. P., (2020): The role of modal parameters uncertainty estimation in automated modal identification, modal tracking and data normalization. *Engineering Structures.*, **224**, 111208.

Pollastro, A.; Testa, G.; Bilotta, A.; Prevete, R., (2023): Semi-supervised detection of structural damage using Variational Autoencoder and a One-Class Support Vector Machine. *IEEE Access.*, **11**, 67098–67112.

Pooya, S. M. H.; Massumi, A., (2021): A novel and efficient method for damage detection in beam-like structures solely based on damaged structure data and using mode shape curvature estimation. *Applied Mathematical Modelling.*, **91**, 670–694.

Pozzi, M., (2022): Decision-making in SHM systems for asset management. *Sensor Technologies for Civil Infrastructures.*, 609–641.

Prendergast, L. J.; Limongelli, M. P.; Ademovic, N.; Anžlin, A.; Gavin, K.; Zanini, M., (2018): Structural Health Monitoring for Performance Assessment of Bridges under Flooding and Seismic Actions. *Structural Engineering International.*, **28**, 296–307.

Proverbio, M.; Vernay, D. G.; Smith, I. F. C., (2018): Population-based structural identification for reserve-capacity assessment of existing bridges. *Journal of Civil Structural Health Monitoring.*, **8**, 363–382.

Punzo, V.; Ciuffo, B.; Montanino, M., (2012): Can results of car-following model calibration based on trajectory data be trusted? *Transportation Research Record.*, 11–24.

Punzo, V.; Ciuffo, B.; Montanino, M.; Daamen, W.; Buisson, C.; Hoogendoorn, S. P., (2014): Sensitivity analysis. In: CRC Press (ed.), *Traffic Simulation and Data: Validation Methods and Applications.*, p. 119.

Rafati Fard, M.; Shariat Mohaymany, A., (2019): A copula-based estimation of distribution algorithm for calibration of microscopic traffic models. *Transportation Research Part C: Emerging Technologies.*, **98**, 449–470.

Rainieri, C., Fabbrocino, G., & Cosenza, E., (2007): Automated Operational Modal Analysis as structural health monitoring tool: theoretical and applicative aspects. *In Key Engineering Materials.*, **347**, 479–484.

Rainieri, C.; Fabbrocino, G., (2014): Operational Modal Analysis of Civil Engineering Structures. *Springer.*, **New York.**

Rao, A. R. M.; Lakshmi, K.; Krishnakumar, S., (2014): A Generalized Optimal Sensor Placement Technique for Structural Health Monitoring and System Identification. *Procedia Engineering.*, **86**, 529–538.

Rastin, Z.; Ghodrati Amiri, G.; Darvishan, E., (2021): Unsupervised Structural Damage Detection Technique Based on a Deep Convolutional Autoencoder. (Caddemi, S., Ed.) *Shock and Vibration.*, **2021**, 1–11.

Rossigali, C. E.; Pfeil, M. S.; Sagrilo, L. V. S.; de Oliveira, H. M., (2023): Load Models Representative of Brazilian Actual Traffic in Girder-Type Short-Span Highway Bridges. *Applied Sciences.*, **13**, 1032.

Rousseeuw, P. J.; Driessen, K. Van, (1999): A Fast Algorithm for the Minimum Covariance Determinant Estimator. *Technometrics.*, **41**, 212–223.

Ruan, X.; Zhou, J.; Shi, X.; Caprani, C. C., (2017): A site-specific traffic load model

for long-span multi-pylon cable-stayed bridges. *Structure and Infrastructure Engineering.*, **13**, 494–504.

Sanayei, M.; Khaloo, A.; Gul, M.; Necati Catbas, F., (2015): Automated finite element model updating of a scale bridge model using measured static and modal test data. *Engineering Structures.*, **102**, 66–79.

Schlune, H.; Plos, M.; Gylltoft, K., (2009): Improved bridge evaluation through finite element model updating using static and dynamic measurements. *Engineering Structures.*, **31**, 1477–1485.

Schommer, S.; Nguyen, V. H.; Maas, S.; Zürbes, A., (2017): Model updating for structural health monitoring using static and dynamic measurements. *Procedia Engineering.*, **199**, 2146–2153.

Sirca, G. F.; Adeli, H., (2005): Case-Based Reasoning for Converting Working Stress Design-Based Bridge Ratings to Load Factor Design-Based Ratings. *Journal of Bridge Engineering.*, **10**, 450–459.

Skokandić, D.; Mandić Ivanković, A., (2022): Value of additional traffic data in the context of bridge service-life management. *Structure and Infrastructure Engineering.*, **18**, 456–475.

Standoli, G.; Giordano, E.; Milani, G.; Clementi, F., (2021): Model Updating of Historical Belfries Based on OMA Identification Techniques. *International Journal of Architectural Heritage.*, **15**, 132–156.

Stephan, C., (2012): Sensor placement for modal identification. *Mechanical Systems and Signal Processing.*, **27**, 461–470.

Sujith, A. V. L. N.; Sajja, G. S.; Mahalakshmi, V.; Nuhmani, S.; Prasanalakshmi, B., (2022): Systematic review of smart health monitoring using deep learning and Artificial intelligence. *Neuroscience Informatics.*, **2**, 100028.

Sun, B.; Xu, Y. L.; Wang, F. Y.; Li, Z.; Zhu, Q., (2019): Multi-scale fatigue damage prognosis for long-span steel bridges under vehicle loading. *Structure and Infrastructure Engineering.*, **15**, 524–538.

Sýkora, M.; Holický, M.; Marková, J., (2013): Verification of existing reinforced concrete bridges using the semi-probabilistic approach. *Engineering Structures.*, **56**, 1419–1426.

Testa, G.; Bilotta, A.; Chioccarelli, E., (2021): Optimal sensor placement for dynamic identification of a reinforced concrete bridge. *fib Symposium 2021, Lisbon*.

Testa, G.; Zaccaria, G.; Montanino, M.; Baltzopoulos, G.; Bilotta, A.; Iervolino, I.; Punzo, V., (2022)a: Infrastructure-level traffic micro-simulation for probabilistic analysis of bridge loads. *Computer-Aided Civil and Infrastructure Engineering*.

Testa, G.; Angelis, A. De; Bilotta, A.; Chioccarelli, E., (2022)b: Dynamic identification, model updating and optimal sensor placement for a prestressed concrete bridge. *Italian Concrete Conference - Napoli*.

Testa, G.; De Angelis, A.; Bilotta, A.; Chioccarelli, E., (2022)c: Dynamic identification, model updating and optimal sensor placement for a prestressed concrete bridge. *Italian Concrete Conference - Napoli*.

Testa, G.; Zaccaria, G.; Montanino, M.; Baltzopoulos, G.; Bilotta, A.; Iervolino, I.; Punzo, V., (2023): Infrastructure-level traffic micro-simulation for probabilistic analysis of bridge loads. *Computer-Aided Civil and Infrastructure Engineering.*, **38**, 1217–1235.

Treiber, M.; Kesting, A.; Wilson, R. E., (2011): Reconstructing the Traffic State by Fusion of Heterogeneous Data. *Computer-Aided Civil and Infrastructure Engineering.*, **26**, 408–419.

Ugray, Z.; Lasdon, L.; Plummer, J. C.; Glover, F.; Kelly, J.; Martí, R., (2005): A Multistart Scatter Search Heuristic for Smooth NLP and MINLP Problems. *Metaheuristic Optimization via Memory and Evolution*. Kluwer Academic Publishers, Boston, pp. 25–57.

Van der Auweraer H.; Leurs W.; Mas P.; Hermans L., (2000): Modal parameter estimation from inconsistent data sets. *In Proceedings of the 18th International Modal*

Analysis Conference., 763–771.

Vincenzi, L.; Simonini, L., (2017): Influence of model errors in optimal sensor placement. *Journal of Sound and Vibration.*, **389**, 119–133.

Waheed, A.; Adeli, H., (2000): A Knowledge-based system for evaluation of superload permit applications. *Expert Systems with Applications.*, **18**, 51–58.

Wall, M. E.; Rechtsteiner, A.; Rocha, L. M., (n.d.) Singular Value Decomposition and Principal Component Analysis. *A Practical Approach to Microarray Data Analysis*. Kluwer Academic Publishers, Boston, pp. 91–109.

Wang, H.; Li, A. Q.; Li, J., (2010): Progressive finite element model calibration of a long-span suspension bridge based on ambient vibration and static measurements. *Engineering Structures.*, **32**, 2546–2556.

Wang, Z.; Cha, Y. J., (2021): Unsupervised deep learning approach using a deep auto-encoder with a one-class support vector machine to detect damage. *Structural Health Monitoring.*, **20**, 406–425.

Wiśniewski, D. F.; Casas, J. R.; Ghosn, M., (2012): Codes for Safety Assessment of Existing Bridges—Current State and Further Development. *Structural Engineering International.*, **22**, 552–561.

Xiao, F.; Hulsey, J. L.; Chen, G. S., (2015): Multi-Direction Bridge Model Updating Using Static and Dynamic Measurement. *Applied Physics Research.*, **7**.

Xiong, Y.; Chen, W.; Tsui, K. L.; Apley, D. W., (2009): A better understanding of model updating strategies in validating engineering models. *Computer Methods in Applied Mechanics and Engineering.*, **198**, 1327–1337.

Yegnanarayana, B., (2009): Artificial neural networks. *PHI Learning Pvt.*

Yi, T. H.; Li, H. N.; Gu, M., (2011): Optimal Sensor Placement for Health Monitoring of High-Rise Structure Based on Genetic Algorithm. *Mathematical Problems in Engineering.*, **2011**, 1–12.

Yin, X.; Huang, Z.; Liu, Y., (2023): Framework of vehicle-bridge coupled analysis for suspension bridges under refined vehicle modeling considering realistic traffic behavior. *Structures.*, **47**, 1991–2005.

Yu, Y.; Wang, C.; Gu, X.; Li, J., (2019): A novel deep learning-based method for damage identification of smart building structures. *Structural Health Monitoring.*, **18**, 143–163.

Yuan, Z.; Zhu, S.; Chang, C.; Yuan, X.; Zhang, Q.; Zhai, W., (2021): An unsupervised method based on convolutional variational auto-encoder and anomaly detection algorithms for light rail squat localization. *Construction and Building Materials.*, **313**, 125563.

Zembaty, Z.; Kowalski, M.; Pospisil, S., (2006): Dynamic identification of a reinforced concrete frame in progressive states of damage. *Engineering Structures.*, **28**, 668–681.

Zhang, B.; Zhou, L.; Zhang, J., (2019): A methodology for obtaining spatiotemporal information of the vehicles on bridges based on computer vision. *Computer-Aided Civil and Infrastructure Engineering.*, **34**, 471–487.

Zhang, Y.; Zhu, J., (2021): Damage identification for bridge structures based on correlation of the bridge dynamic responses under vehicle load. *Structures.*, **33**, 68–76.

Zhao, J.; Zhang, L., (2012): Structural Damage Identification Based on the Modal Data Change. *International Journal of Engineering and Manufacturing.*, **2**, 59–66.

Zhou, J.; Li, T.; Ye, X.; Shi, X., (2020): Safety Assessment of Widened Bridges Considering Uneven Multilane Traffic-Load Modeling: Case Study in China. *Journal of Bridge Engineering.*, **25**.

Zhou, J.; Lu, Z.; Zhou, Z., (2022): Structural Safety Assessment and Traffic Control Strategies of Widened Highway Bridges under Maintenance Works Requiring Partial Lane Closure. *KSCE Journal of Civil Engineering.*, **26**, 1846–1857.

List of Figures

Figure 1 – Flow chart.....	5
Figure 2 – Flowchart about FDD technique.....	27
Figure 3 – Elastic spring - carriage system	28
Figure 4 – Flowchart Model Updating.....	33
Figure 5 – Flowchart of the methodology.....	38
Figure 6 – Case study.....	39
Figure 7 – Masses distribution	39
Figure 8 – Sensors’ position and orientation	40
Figure 9 – Damaged cases	41
Figure 10 – Comparison between output of VAE and target, healthy case	42
Figure 11 – Comparison between output of VAE and target, damaged case	42
Figure 12 – OC – SVM domain, healthy case	42
Figure 13 – OC – SVM domain, damaged case.....	42
Figure 14 – Influence of noise when it is present during the training stage.....	46
Figure 15 – Influence of noise when it emerges after the training stage.....	46
Figure 16 – Influence of noise on the representation of the first singular value of decomposed PSD for healthy case.....	46
Figure 17 – Influence of noise on the representation of the first singular value of decomposed PSD for case 4 (damaged)	47
Figure 18 – Influence of noise on the representation of the first singular value of decomposed PSD for case 9 (damaged)	47
Figure 19 – Geometric properties	48
Figure 20 – Static schemes	48
Figure 21 – Paired configuration	49
Figure 22 – Longitudinal configuration	50
Figure 23 – Static test	51
Figure 24 – Damaged cases: (a) L4.2, (b) L4.3 e (c) L4.4	51
Figure 25 – Sensors’ location	52
Figure 26 – Force displacement curves.....	53
Figure 27 – Comparison between experimental curve (red or blue) and numerical one (black)	54
Figure 28 – Comparison between output of VAE and target, healthy case	55
Figure 29 – Comparison between output of VAE and target, damaged case	55
Figure 30 – OC – SVM results	56
Figure 31 – Initial sensor configuration.....	63
Figure 32 – Efficiency ranking, X direction	64
Figure 33 – Efficiency ranking, Y direction	65
Figure 34 – Efficiency ranking, Z direction.....	65
Figure 35 – Efficiency curve with frequency error, X direction	66
Figure 36 – Efficiency curve with frequency error, Y direction	67
Figure 37 – Efficiency curve with frequency error, Z direction	67
Figure 38 – MAC with all the sensors on the left and the optimal configuration on the right ...	68
Figure 39 – The case study	69
Figure 40 – FE Model.....	70
Figure 41 – Sensors’ placement.....	71
Figure 42 – Experimental results: modal shapes.....	72
Figure 43 – MAC.....	73
Figure 44 – Efficiency curve.....	74
Figure 45 – Optimal sensor configuration	74
Figure 46 – MAC comparison	75
Figure 47 – Initial sensors configuration, regular mesh.....	75
Figure 48 – Efficiency curve.....	76
Figure 49 – Optimal solution	76
Figure 50 – MAC.....	77
Figure 51 – Tammarecchia bridge	78

Figure 52 –FE Model	79
Figure 53 – External constraint	79
Figure 54 – Tests setup and load schemes.....	80
Figure 55 – Sensitivity analysis: concrete elastic modulus	81
Figure 56 – Sensitivity analysis: flexural rotational stiffness.....	82
Figure 57 – MAC with Model 1	82
Figure 58 – Transversal deformation – Model 1	83
Figure 59 – Static comparison, Model 2	84
Figure 60 – Static comparison, Model 3	85
Figure 61 – Comparison of updated models.....	87
Figure 62 – Location of case studies on the A56 – Tangenziale di Napoli	90
Figure 63 – Cases study: (a) Miano Agnano, (b) Arena Sant’Antonio, (c) Calata San Domenico viaducts	91
Figure 64 – Miano Agnano: (a) middle section of beam, (b) beam’s section at the support, (c) top view of pulvinus - dimensions in cm.....	93
Figure 65 – Arena S. Antonio: (a) middle section of beam, (b) beam’s section at the support - dimensions in cm.....	94
Figure 66 – Cross section: (a) Miano Agnano, (b) Arena Sant’Antonio, (c) Calata San Domenico viaducts.....	95
Figure 67 – FEM Model: (a) Miano Agnano, (b) Arena Sant’Antonio, (c) Calata San Domenico viaducts	95
Figure 68 – Schema di carico 1 previsto dalle NTC2018 in riferimento alla prima corsia convenzionale di carico.....	97
Figure 69 – Load scheme with 440 kN, DM2020	98
Figure 70 – Load scheme with 260 kN, DM2020	98
Figure 71 – Cluster analysis	101
Figure 72 - Total flows for "weekdays with school" from 6 to 10 a.m.	103
Figure 73 - PCC matrix of total flows for 24 hours, weekday period with school 2018	104
Figure 74 – Example of vehicle geometry.....	105
Figure 75 – Percentage of each vehicle class within the toll class	106
Figure 76 - Simulated trajectories: (a) congested condition and (b) free flow condition	108
Figure 77 - Frequency distributions of marginal load by year	109
Figure 78 – Static schemes	111
Figure 79 – Spatial distribution of axis	112
Figure 80 – Spatial distribution of forces	113
Figure 81 – Distribution of Maximum Daily Bending Moment at the middle section.....	114
Figure 82 – Distribution of Maximum Daily Shear at the support.....	115
Figure 83 – Distribution of Maximum Annual Bending Moment: (1) Miano Agnano, (2) Arena Sant’Antonio, (3) Calata San Domenico	117
Figure 84 - Distribution of Maximum Annual Shear: (1) Miano Agnano, (2) Arena Sant’Antonio, (3) Calata San Domenico	117

List of Tables

Table 1 – Damaged cases.....	40
Table 2 - Results	43
Table 3 - Results	43
Table 4 - Results	44
Table 5 – FDD results.....	45
Table 6 - Mechanical properties	48
Table 7 - Moment and shear limit values.....	48
Table 8 - Frequency	49
Table 9 – Experimental frequency – unloaded joist.....	50
Table 10 - Experimental frequency – loaded joist.	51
Table 11 – Operational sensors.....	55
Table 12 - PoD _{avg} for all cases	56
Table 13– Analytical modal analysis	63
Table 14 - Results	67
Table 15 – Analytical modal analysis	70
Table 16 – Experimental results: frequency	71
Table 17 – Comparison between real behavior and numerical ones	72
Table 18 – Frequency comparison	73
Table 19 - Frequency comparison.....	75
Table 20 – Static comparison.....	81
Table 21 - Dynamic comparison.....	81
Table 22 – Comparison between Model 0 and Model 1 about the modal frequency.....	82
Table 23 – Static comparison – Model 1	83
Table 24 – Dynamic comparison, Model 2.....	84
Table 25 – Vertical displacement	86
Table 26 - Frequency	86
Table 27 – Conventional lanes according to NTC2018	97
Table 28 – Partial safety factors provided by DM2020 and NTC2018.....	99
Table 29 – Vehicle classification.....	104
Table 30 – Behavioral parameters of vehicles	107
Table 31 – Percentages of total weight distribution for each axis.....	111
Table 32 - Parameters of the distributions for moment (M) and Shear (V) for each typical day	114
Table 33 - Ratios of percentiles of simulations and codes - traffic load only	118
Table 34 - Percentile ratios of simulations and codes - in combination.....	119